

KINEMATICS OF NONLINEARLY INTERACTING MHD INSTABILITIES IN
A PLASMA

by

Alexander K. Hansen

A dissertation submitted in partial fulfillment of the
requirements for the degree of

Doctor of Philosophy

(Physics)

at the

University of Wisconsin—Madison

2000

KINEMATICS OF NONLINEARLY INTERACTING MHD INSTABILITIES IN A PLASMA

Alexander K. Hansen

Under the supervision of Professor Stewart C. Prager and Dr. Daniel Den Hartog

At the University of Wisconsin—Madison

ABSTRACT

Plasmas play host to a wide variety of instabilities. For example, tearing instabilities use finite plasma resistivity to exploit the free energy provided by plasma currents parallel to the magnetic field to alter the magnetic topology of the plasma through a process known as reconnection. These instabilities frequently make themselves known in magnetic confinement experiments such as tokamaks and reversed-field pinches (RFPs). In RFP plasmas, in fact, several tearing instabilities (modes) are simultaneously active, and are of large amplitude. Theory predicts that in addition to interacting linearly with magnetic perturbations from outside the plasma, such as field errors or a resistive wall, the modes in the RFP can interact nonlinearly with each other through a three-wave interaction.

In the current work investigations of both the linear (external) and nonlinear contributions to the kinematics of the tearing modes in the Madison Symmetric Torus (MST) RFP are reported. Theory predicts that tearing modes will respond only to magnetic perturbations that are spatially resonant with them, and was supported by experimental work done on tokamak devices. The results in this work verified that the theory is still applicable to the RFP, in spite of its more complicated magnetic mode structure, involving perturbations of a single poloidal mode number,

i.e. that affect multiple modes simultaneously. However, for perturbations of a single toroidal mode number, i.e. resonant with only one mode, it was found that multiple modes were simultaneously affected, and that the required torque was larger than that needed for those of a single poloidal mode number, presumably due to viscous drag between modes.

Three pieces of evidence were found that indicated experimentally the existence of nonlinear torques in MST. The core-resonant tearing modes in MST undergo episodic negative accelerations (slowing down) in ordinary discharges during sawtooth events. It was found that when the rotation profile was shifted by an applied electric field such that these modes rotated in the opposite direction to normal, the episodic accelerations were in the same direction as in standard discharges—the modes now accelerated, which is contrary to what an external torque from a stationary field error would do. In addition, when one of the modes that is required for the three-wave nonlinear interaction was removed from the plasma, the large changes in the mode velocity disappeared. Finally, the correlated triple products characteristic of the nonlinear torque were measured, and they were found only to be in the right phase to produce a torque during the sawtooth events.

Finally, to combine these efforts, sawtooth events in which the core-resonant modes locked (became stationary in the lab frame) were compared with those where the modes continued to rotate. The result was that neither the external nor the internal torques were substantially different between the two cases, so the cause of the locking remains unknown.

Acknowledgements

First and foremost, I would like to thank my advisor, Stewart Prager. In addition to providing the money, he has given me much good advice on my research, and on going beyond grad school. Even though his schedule has been packed with meetings, he makes the effort to be available to his students.

Thanks to my defense committee for being available for this, my second scheduled defense. They are Professor Paul Terry and Assistant Professor Cary Forest as readers, and Professor Clint Sprott and Associate Professor David Anderson as nonreaders.

Daniel Den Hartog has provided me with valuable feedback on my ideas, asking good questions so that I understand all of the ramifications better. Thanks also for the IDS. If I've got any questions about spectroscopy for my next position (a strong possibility), he will definitely be one of the first people I get a hold of.

The scientific staff have been invaluable in my professional education. John Sarff helped with one of the measurements in this work by holding a probe inside MST, and has offered many good ideas. Thanks to Abdulagder Almagri for your extensive knowledge of the poloidal gap and its coils, as well as your molybdenum probes to spin the plasma. Gennady Fiksel has made suggestions that I have later had to understand the ramifications of. Thanks to Chris Hegna for theoretical support and discussion, so that I can understand(?) what I'm talking about, and for the class notes from his reconnection class.

Thanks to all of the grad students and postdocs, past and present, who've been there to provide a stimulating (sometimes overly so) intellectual environment. Special thanks to Jim Chapman, who put up with living with me for two years, and provided the analysis code I've

built my career on; Kevin Mirus, who took me in when I was just learning about field errors and locking; Jay Anderson, who provided me with mornings of beer and brats, and Darren Craig for the stimulating discussions, and for being a sounding board for the ideas that I thought were too crazy to take to Dan. Thanks also for the improved mode analysis code.

Other people who I'd like to mention include Ted Biewer, Brett Chapman, Nick Lanier, Paul Fontana, Neal Crocker, Ching-Shih Chiang, Derek Baver, Cavendish McKay, Don Holly, John Wright, Eduardo Fernandez, Carl Sovinec, Matt Stoneking, Hantao Ji, Miodrag Cekic, Diane Demers, Uday Shah, Jianxin Lei, Susanna Castillo, Philip Andrew, Yohan Tabora, Jim Reardon, Steve Terry, Renato Gatto, and Stefan Gerhardt, even though he went to HSX.

Thanks to all of the grad students, postdocs, and engineers who have operated MST so that I could get all of this data. I took a lot of weekends, and I especially appreciate those poor souls who got dragged in then.

Thanks to Larry Smith and Paul Wilhite, who keep the computers running so I can look at my data, and for continually upgrading my hardware—Mac Plus, anyone?

Thanks to the engineering staff, especially Mark Thomas and Steve Oliva, for your work on building the RMP system. The system did what it could, against overwhelming adverse physics. Thanks also to John Lauffenberg, who put up with all of the temporary changes that evolved into permanent ones.

To Brian Schwartz, nuclear physicist and my roommate for three years, thanks for the remark that I was “almost a theorist”. When I was here at work struggling to assemble an amplifier, I remembered those words, and went right back to work.

Thanks to my parents, Karl and Sharon, for your support and understanding, even though my chances of going back home for work are pretty slim. Thanks also to my brothers and my whole extended family, who have put up with my attempts to explain plasma physics and what my dissertation research is about.

Thanks to the USDOE, supported by the American taxpayers, for providing the grant under which this work was performed.

Last, but not least, I would like to thank my fiancée, Becky Freiburger (soon to be Hansen), for putting up with the late nights, fighting with the computer, and general stress. I also want to thank you for keeping me motivated to get done and move on to bigger and better things.

Table of Contents

Abstract	i
Acknowledgements	iii
Table of Contents.....	vi
List of Figures	x
List of Tables.....	xiii
1. Introduction and Synopsis.....	1
1.1. Definitions	2
1.2. Motivation.	3
1.3. Prior Work.....	5
1.4. Overview of results.....	5
1.4.1.External electromagnetic torque.....	5
1.4.2.Internal electromagnetic torque.....	6
1.5. Layout of this dissertation.	7
2. Background.....	8
2.1. The RFP concept.....	8
2.2. Tearing modes.	9
2.2.1. Tearing mode rotation.....	10
2.2.1.1.External electromagnetic torques.	11
2.2.1.2.Internal electromagnetic torques.....	12
2.2.1.2.1. Toroidal coupling.....	13

2.2.1.2.2. Nonlinear torques.....	14
2.2.2. Mode locking.....	15
2.3. RFP mode structure.....	16
2.3.1. $m = 1$ modes.....	17
2.3.2. $m = 0$ modes.....	17
2.3.3. $m \geq 2$ fluctuations.....	18
2.3.4. High- n fluctuations.....	20
2.4. The RFP sawtooth cycle.....	20
2.5. Summary	22
3. Experimental Considerations.....	24
3.1. Tools for Active Experiments.....	24
3.1.1. Shell gaps and coils at gaps.....	24
3.1.1.1. Poloidal gap.....	24
3.1.1.2. Toroidal gap	25
3.1.2. Power supplies.....	26
3.1.2.1. Static perturbation.....	26
3.1.2.2. Rotating magnetic perturbation (RMP).....	26
3.2. Diagnostics	28
3.2.1. Magnetic arrays	28
3.2.1.1. Toroidal array coil calibration.....	30
3.2.1.2. Determination of mode helicity.....	31

3.2.2. Calibration of perturbation amplitude at toroidal gap.	33
3.2.2.1. Measurements	33
3.2.2.1.1. Measurement of magnetic field within the toroidal flange.....	33
3.2.2.1.2. Measurement of the magnetic field within the VCV	37
3.2.2.2. Finding the $m = 1$ spectral component.....	40
3.2.3. Further Diagnostics.....	41
3.3. Ensemble Averaging	42
Appendix to Chapter 3	43
4. Experiments Involving External Torques	50
4.1. Static Perturbation Experiments.	51
4.1.1. Poloidal gap.....	51
4.1.1.1. Background field errors and mode rotation.....	51
4.1.1.2. Effect of $m = 1$ perturbation on $m = 1$ modes (resonant).....	53
4.1.1.3. Effect of $m = 0$ perturbation on $m = 1$ modes (nonresonant).....	54
4.1.1.4. Effects of $m = 0$ perturbation on $m = 0$ modes (resonant)	55
4.1.1.5. Effects of $m = 1$ perturbation on $m = 0$ modes (nonresonant).	56
4.1.1.6. Effects of applying an $m = 2$ perturbation (nonresonant).	57
4.1.2. Toroidal gap	59
4.1.3. Quantitative comparison of EM torques	62
4.1.4. Estimating the viscous torque	65
4.2. Rotating Magnetic Perturbation.....	69

4.3. External Torques During Sawtooth Activity	71
4.4. Summary	73
5. Experiments involving nonlinear electromagnetic torques.....	75
5.1. Nonlinear Torques in Active Experiments.....	76
5.2. Nonlinear Torques in Sawtooth Activity	76
5.2.1. Modes and flow	76
5.2.2. Mode dynamics in the MST sawtooth cycle.....	78
5.2.2.1. Standard case	78
5.2.2.2. Applied radial electric field.....	79
5.2.2.3. Non-reversed discharge.....	83
5.2.3. Triple product measurement	84
5.3. Permanent Locking vs. Reacceleration During Sawtooth Events.	86
5.4. Summary	92
6. Summary and Future Work	94
6.1. Summary of Physics Results	94
6.2. Future Work.....	95

List of Figures

1.1. Directions in toroidal geometry.....	4
2.1. Calculated q profile with resonant surface locations.....	9
2.2. Cartoon of formation of magnetic islands by a tearing mode.....	10
2.3. Calculated q profile showing estimated $m = 1$ island widths.....	17
2.4. $m = 1$ and $m = 2$ rotation frequencies.....	19
2.5. $m = 1$ and $m = 2$ power spectra.....	20
2.6. Sawtooth cycle behavior of several signals.....	21
3.1. Poloidal flange, showing the locations of the correction coils.....	25
3.2. Cartoon of external $m = 0$ coils.....	26
3.3. $n = 6$ coil schematic.....	27
3.4. Current from static perturbation power supply.....	27
3.5. Circuit diagram for rotating magnetic perturbation amplifier.....	28
3.6. Cartoon of entire RMP system.....	28
3.7. Toroidal array coil form.....	29
3.8. Layout for coil forms used at the poloidal gap.....	30
3.9. Sketch of 1/4" hole probe.....	34
3.10. Sketch of toroidal flange layout, showing $n = 6$ coils and probe.....	34
3.11. Sketch of toroidal flange layout, showing $n = 6$ coils and flux loop.....	35

3.12. Data for magnetic fields in the toroidal flange.	36
3.13. Probe used for internal magnetic measurements.	38
3.14. Data from internal probe measurements, largest signal for all components.	39
3.15. Radial magnetic field profiles inside the vacuum vessel.	39
3.16. The Ion Dynamics Spectrometer.	41
3.A.1. Profile of the radial magnetic field from perturbation at the toroidal gap.....	45
4.1. Discharge with no pulsed magnetic perturbation, correction coils disengaged.	52
4.2. Discharge with no pulsed magnetic perturbation, correction coils engaged.	52
4.3. Discharge with pulsed $m = 1$ magnetic perturbation at the poloidal gap.	53
4.4. Discharge with pulsed $m = 1$ magnetic perturbation at the poloidal gap.	54
4.5. Discharge with pulsed $m = 0$ magnetic perturbation at the poloidal gap.	55
4.6. Ensembles of discharges with applied electric field and $m = 0$ perturbation.	56
4.7. Ensembles of discharges with applied electric field and $m = 1$ perturbation.	57
4.8. Discharge with pulsed $m = 2$ magnetic perturbation at the poloidal gap.	58
4.9. Ensembles with applied electric field and $m = 2$ perturbation.	59
4.10. Discharge with applied $n = 6$ perturbation, exhibiting prompt locking.	60
4.11. Discharge with applied $n = 6$ perturbation, exhibiting locking and unlocking.	61
4.12. Ensemble of discharges with applied RMP.....	70
4.13. Ensemble averaged quantities for external torque on (1,6) mode.	71
4.14. Ensemble averaged quantities for external torque on (0,1) mode.	72

5.1. Ensemble of velocities and accelerations of (1,6) mode (solid) and C^{4+} ions.	77
5.2. Mode amplitudes ensemble averaged over ~ 700 sawtooth events.	78
5.3. Velocity and acceleration of $m = 1$ modes, ensemble averaged.	79
5.4. (1,6) and (0,1) mode toroidal phase velocities, ensemble averaged.	80
5.5. C^{4+} and C^{2+} toroidal flow velocity for a discharge with applied electric field.....	81
5.6. (1,6) mode phase velocity and C^{4+} flow for a discharge with applied electric field. .	81
5.7. (0,1) and (1,6) modes with applied radial electric field, ensemble averaged.	82
5.8. (0,1) and (1,6) modes with radial electric field, sawtooth ensemble averaged.	83
5.9. Non-reversed discharge.....	84
5.10. Relevant quantities for nonlinear torque, ensemble averaged over ~ 700 sawteeth. .	86
5.11. Typical discharge where locking occurs.	87
5.12. Ensemble averaged kinematic quantities for sawteeth with and without locking. ...	87
5.13. External torque products in ensembles of sawtooth crashes.	88
5.14. Relevant quantities for nonlinear torque in ensemble over locking sawteeth.	89
5.15. Comparing NL quantities in ensembles over sawteeth with and without locking...	90
5.16. C^{4+} ion velocity and acceleration, (1,6) mode velocity and acceleration.	91
5.17. Velocity of (1,6) mode, C^{4+} ion toroidal velocity, and C^{2+} ion toroidal velocity.....	92

List of Tables

Table 3.1. Calibration data for RMP toroidal flange field measurements.....	37
Table 3.2. Summary of results from interior measurement of RMP magnetic fields.....	40

1 Introduction and Synopsis

Plasmas frequently have instabilities within them, both in nature and in experimental devices. Some of these instabilities, such as tearing modes (§ 1.1), also have a wavelike character to them, and can therefore propagate. The experimental work performed for this dissertation consisted of investigating the kinematic response of tearing modes in the Madison Symmetric Torus (MST) Reversed Field Pinch (RFP)¹ to external and internal electromagnetic torques.

External torques are produced by magnetic fields whose source lies outside the plasma. It was found experimentally in this work, as well as previously (see § 1.3), that a *spatial resonance* condition between the perturbation and the tearing mode had to be satisfied for a torque to be exerted, in agreement with theory.^{2,3} The condition was that the mode and the perturbing agent both must have their wavevector component parallel to the magnetic field vanish somewhere within the plasma, i.e. $\mathbf{k} \cdot \mathbf{B} = 0$, with the same \mathbf{k} for both the mode and the perturbing agent. A new feature in the current work is that a difference was found between the effects of applied perturbations that are resonant with single modes and those that are resonant with multiple modes.

Internal torques are produced within the plasma by interactions between three tearing modes. These require $\mathbf{k} \cdot \mathbf{B} = 0$, where \mathbf{k} is the wavevector of one of these modes, just as for the external torque. These torques can be due to geometric (toroidal) effects, where the perturbing agent is the part of another mode with the same \mathbf{k} , or from nonlinear three-wave mode coupling, which requires $\mathbf{k} = \mathbf{k}' + \mathbf{k}''$, where \mathbf{k}' and \mathbf{k}'' are the wavevectors of the two other tearing modes. Experimentally, it was found that the products of mode amplitudes that characterize the nonlinear torques become large on a sawtooth crash (see § 1.1), where the nonlinear drive is expected

to be large. The relative phase between the modes also becomes such that a torque is generated only near the crash. When one of the modes is removed from the plasma, the kinematics of the other modes exhibit the absence of an internal torque. Finally, when an external perturbation is applied that is resonant with only one of the modes in a triplet, other modes can respond to it as well—this is consistent with the nonlinear torque, but not the torque from toroidicity. Because of tight coupling between the mode rotation and the flow (to be shown later) it will be argued that a result of the action of the internal torque is radial transport of toroidal momentum, i.e. changes in its radial profile. Thus, in addition to being important for nonlinear coupling of the modes, this interaction provides a mechanism for transport other than electrostatic or magnetic fluctuations (Rechester-Rosenbluth).

1.1 Definitions

Certain terms will be used throughout this work. The most fundamental of them will be defined here, and more detail will be provided in Chapter 2:

Reversed-field pinch refers to a particular magnetic field configuration used to confine a plasma.

Axisymmetry means that the toroidal direction is regarded as a direction of symmetry.

Tearing modes are instabilities in the plasma. Their free energy source is current in the plasma, they require resistivity, and they form around locations in the plasma where the magnetic field satisfies certain conditions. Their name comes from the fact that they change the magnetic topology of the plasma.

Field errors or *error fields* are irregularities in the magnetic field. Ideally, in MST or similar magnetic confinement devices the magnetic field is supposed to be two-dimensional, having only

components in the toroidal (long way around the torus) and poloidal (short way around) directions (Fig. 1.1). However, for real devices there are deviations from the perfect structure.

Magnetic perturbations are deliberate changes made to the magnetic field structure, in order to distort its two-dimensional nature. In practice magnetic perturbations and field errors are identical, but the distinction will be made to distinguish between intentionally applied changes and extant defects in the magnetic structure.

Viscous torque is created by differential rotation in a medium that has finite dissipation.

Sawteeth in MST are phenomena that involve rapid ($\sim 100 \mu\text{s}$) changes in most of the equilibrium parameters. In addition, they are characterized by dramatically enhanced fluctuation levels.

Locking of a tearing mode means that it becomes stationary in the laboratory frame. In MST, the rotating tearing modes sometimes lock following a sawtooth crash, but frequently do not.

1.2 Motivation

The basic issues discussed earlier can now be made more concrete by using the definitions in §1.1. The essential goal of this work was to understand how tearing modes in the plasma

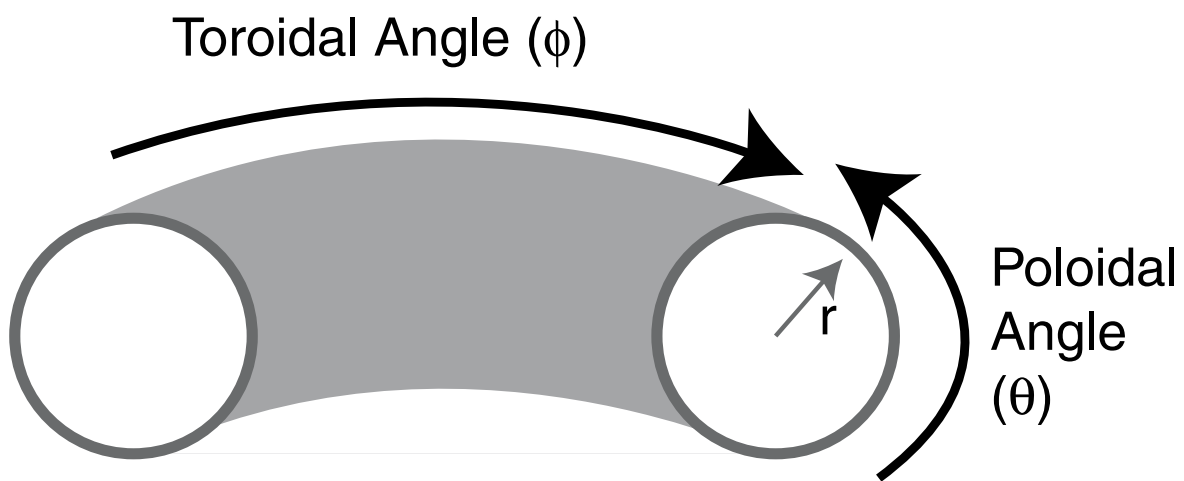


Figure 1.1. Directions in toroidal geometry

produce and respond to external and internal electromagnetic torques (as per the definition in §1.1). Regardless of the mechanism, for a torque to be exerted a resonance condition between the mode and the perturbing agent(s) must be satisfied. The perturbing agents may be external to the plasma, e.g. error fields, or deliberately applied magnetic perturbations from external coils; or internal to it, e.g. interactions between tearing modes.

A principal motivation for the work undertaken has been to understand the kinematics of rotating tearing modes in a situation where there is strong nonlinear coupling between the modes. These modes decelerate at sawtooth events, and either reaccelerate or remain motionless in the lab frame afterward. Because the deceleration is very fast ($\sim 100 \mu\text{s}$), an electromagnetic torque of some variety is a reasonable explanation for the phenomenon. The rapid change in the mode rotation/flow represents transport of momentum that is much faster than the classical collisional timescale.

A secondary motivation was to understand how multiple overlapping islands and the consequent magnetic stochasticity affect the phenomenon of mode locking. The results can be compared with those from tokamak experiments. The two magnetic configurations are similar in their axisymmetry and the presence of currents in the plasma that can drive tearing modes. However, tokamak plasmas with tearing mode activity typically have only one or two magnetic islands present, whereas RFPs have multiple islands, which overlap and lead to large-scale stochasticity, as well as more pronounced nonlinear effects. Thus, a tokamak provides a similar system with simpler properties with which the results here can be compared.

The final motivation was to attempt to develop some quantitative understanding concerning the response of the modes to applied magnetic perturbations, e.g. perturbation ampli-

tudes required to lock a mode. Schemes to control the modes via applied perturbations, which are currently being pursued on MST, require such knowledge so that they may be designed to have a reasonable chance of effectiveness.

1.3 Prior Work

Experiments involving locking and rotation control through resonant magnetic perturbations have been performed on several tokamak devices; among them are: D-IIID,⁴ and COM-PASS-C.⁵ It was found that stationary magnetic perturbations affected modes with which they were resonant, including stabilization of the mode for appropriate phasing between the mode and perturbation. Experiments performed on the HBT-EP tokamak used rotating resonant magnetic perturbations to control the rotation of and stabilize a tearing mode.⁶

Prior measurements have been made on MST concerning mode locking and the role of field errors.⁷ The results include measurement of coupling between the modes. In addition, experiments have been performed on the RFX reversed-field pinch that involved rotating a mode through application of a resonant magnetic perturbation.⁸ In these experiments it was found that in addition to rotating the targeted mode, modes of different helicities were made to rotate in such a way as to satisfy a three-wave nonlinear coupling condition.

1.4 Overview of results

The results will be broken down in terms of the relevant physics, which is external vs. internal torques. The real experiments involve both torques, of course, but one or the other in will be emphasized in the discussion.

1.4.1 External electromagnetic torque

To understand the external electromagnetic torque, experiments were performed in which magnetic perturbations that were static in space but impulsive in time were applied. These per-

turbations either met a spatial resonance condition within the plasma, or did not. Theory predicts that an effect is seen only if the resonance condition is satisfied. If the resonance condition was not met, no effect on the kinematics of the tearing modes was seen, while if the resonance condition was met the modes were able to respond to it, resulting in locking. A further experiment along these lines was attempted in which a rotating magnetic perturbation was applied; this had no effect due to insufficient power.

1.4.2 Internal electromagnetic torques

The internal torque exhibited itself in the static perturbation experiments. It was found that certain magnetic perturbation configurations, in addition to affecting the mode that was resonant with the perturbation, interacted with other modes as well. This only holds for the non-linear interaction, not the geometric one

In addition, an experiment was performed in which the plasma equilibrium was altered to remove the resonance for one class of the tearing modes involved in the internal torque. It was found that the kinematics of the other modes were changed.

Finally, the internal torque makes itself known in passive experiments. It was found that a correlated triple product which is representative of this type of torque becomes large at sawtooth events, as expected from theoretical considerations. Moreover, the relative phase between the modes comes into alignment to produce such a torque only near the sawtooth crash, and its timescale is consistent with the observed mode deceleration time. Finally, results will be presented concerning the bifurcation between sawtooth events where the modes stop rotating and where they reaccelerate (cf. §1.1).

1.5 Layout of this dissertation.

The remainder of this work will be laid out as follows. Chapter 2 will focus on the theoretical background necessary to understand the experimental results. Chapter 3 will cover the diagnostics used, as well as the relevant analysis techniques. Chapter 4 is the first results chapter, in which experiments focused on external electromagnetic torques will be discussed. Chapter 5, the second results chapter, will deal with the experiments that relate to internal electromagnetic torques. Finally, Chapter 6 will include a summary of the results, and a discussion of possible future directions of research.

¹ R. N. Dexter, D. W. Kerst, T. W. Lovell, S. C. Prager, and J. C. Sprott, *Fusion Technol.* **19**, 131 (1991).

² R. Fitzpatrick, T. C. Hender, *Phys. Fluids B* **3**, 644 (1991).

³ R. Fitzpatrick, *Nucl. Fusion* **33**, 1049 (1993).

⁴ J.T. Scoville, R.J. LaHaye, A.G. Kellman, T.H. Osborne, R.D. Stambaugh, E.J. Strait, and T.S. Taylor, *Nucl. Fusion* **31**, 875 (1991).

⁵ T.C. Hender, R. Fitzpatrick, A.W. Morris, P.G. Carolan, R.D. Durst, T. Edlington, J. Ferreira, S.J. Fielding, P.S. Haynes, J. Hugill, I. J. Jenkins, R.J. LaHaye, B.J. Parham, D.C. Robinson, T.N. Todd, M. Valovi_, and G. Vayakis, *Nucl. Fusion* **32**, 2091 (1992).

⁶ G.A Navratil, C. Cates, M.E. Mael, D. Maurer, D. Nadle, E. Taylor, Q. Xiao, W.A. Reass, G.A Wurden, *Phys. Plasmas* **5**, 1855 (1998).

⁷ A.F. Almagri, S. Assadi, S.C. Prager, J.S. Sarff, D.W Kerst, *Phys. Fluids B* **4**, 4080 (1992).

⁸ R. Bartiromo, T. Bolzonella, A. Buffa, G. Chitarin, S. Martini, A. Masiello, S. Ortolani, R. Piovan, P. Sonato, and G. Zollino, *Phys. Rev. Lett.* **83** 1779 (1999).

2 Background

In order to understand fully the experimental results, some background is necessary. A brief overview of the reversed-field pinch (RFP) will first be provided. Then a brief overview of tearing modes and their kinematics will be given. Next the discussion is specialized to the RFP mode configuration, and the chapter ends with a discussion of the RFP sawtooth cycle.

2.1 The RFP concept

The RFP is an axisymmetric, toroidal magnetized plasma configuration with an equilibrium magnetic field that has toroidal and poloidal components, which are of comparable magnitude. The configuration gets its name from the fact that the toroidal field reverses sign near the plasma edge. In an idealized situation of perfect axisymmetry and no fluctuations, the magnetic fields form closed, nested “flux surfaces”. For a review of the RFP, see Refs. 1-4.

The equilibrium fields in axisymmetric magnetized plasma configurations are typically described in terms of the parameter q , known as the “safety factor” for historical reasons. This quantity is defined as the ratio of toroidal transits to poloidal transits of a magnetic field line. In arbitrary axisymmetric geometry, it is defined as follows:

$$q \equiv \frac{1}{2\pi} \int_0^{2\pi} \left(\frac{d\phi}{d\theta} \right) d\theta, \quad (2.1)$$

where ϕ is the toroidal angle, θ is the poloidal angle, and the integral and derivative are done following a magnetic field line. In a cylindrical approximation, $q = q(r) = rB_\phi/RB_\theta$, where r is the radius of interest, R is the major radius of the (toroidal) device, B_ϕ is the toroidal component of the magnetic field, and B_θ is the poloidal component. A distinguishing feature of the RFP besides the reversal of B_ϕ is that $q < 1$ everywhere in the plasma.

The surfaces where $q = m/n$ for integer m and n , i.e. a rational number, are of special importance, because at such places $\mathbf{k} \cdot \mathbf{B} = 0$, where \mathbf{k} is the wavenumber of a perturbation. This situation permits the formation of instabilities such as tearing modes (§ 2.2). Although there are an infinite number of these rational surfaces, in practice, those that are of lowest order are the most unstable. An example of a computed q profile for MST-like parameters from a cylindrical model is shown in Fig. 2.1, along with the radial locations of important rational number values. Note the location where $q = 0$, the so-called “reversal surface” or “reversal radius”. In addition to the toroidal field changing direction at this location, multiple modes of different helicity can be simultaneously unstable here.

2.2 Tearing modes

In an ideal magnetohydrodynamic (MHD) description of the plasma, the magnetic field “lines” move with the plasma flow. This is known as the “frozen flux theorem”. Non-ideal effects, such as finite resistivity, allow the magnetic field to slip through the plasma. The breaking

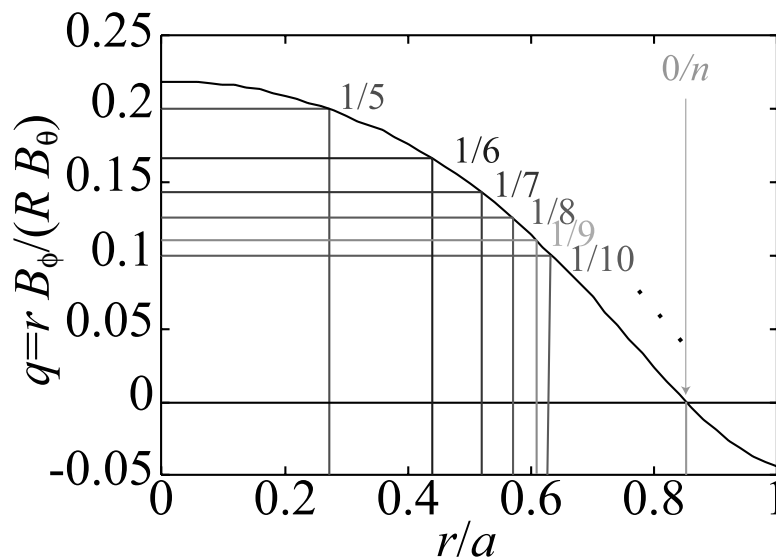


Figure 2.1. Calculated q profile for MST-like parameters, showing locations of selected rational surfaces.

of the frozen flux condition taps free energy to form instabilities such as tearing modes. These modes are driven by currents parallel to the equilibrium magnetic field, and can change the magnetic topology through a process known as reconnection. The reconnection process forms periodic structures within the plasma known as magnetic islands. A cartoon of this process is shown in Fig. 2.2.

The fluctuations in MST have been measured to have tearing/resistive kink character.⁵ The following discussion is applicable regardless of the exact nature of the mode, so “tearing mode” will be used as shorthand.

2.2.1 Tearing mode rotation

Plasmas frequently exhibit rotation (flow). The magnetic islands formed by tearing modes tend to rotate as well. In an MHD description of the plasma, the kinematics of the rotation of a tearing mode are governed by the balance between the inertia and the electromagnetic and viscous torques acting upon it.^{6,7} Without getting into the gory details of the theory, the equa-

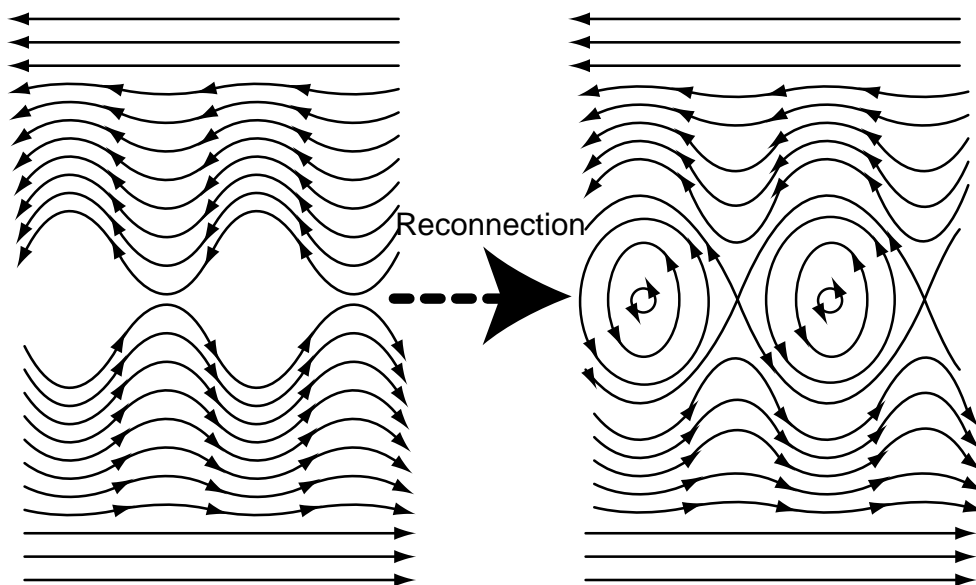


Figure 2.2. Cartoon of formation of magnetic islands by a tearing mode.

tion describing the island rotation can be expressed as:

$$I \frac{d\Omega}{dt} = T_{em} + T_{vis}, \quad (2.2)$$

where I is the moment of inertia, Ω is the angular velocity of the mode, T_{em} is the electromagnetic torque, and T_{vis} is the viscous torque.

The viscous torque comes from differential rotation, which can be that between the island and the surrounding plasma or between the island and other islands. This torque is proportional to the difference between the mode's rotation and its "natural" frequency, which is determined by the plasma flow at the mode's rational surface. This dissertation will not focus on this torque, but rather on the electromagnetic contribution. The viscous torque has the form

$$T_{vis} = \int d^3x \rho v_{\perp} R \frac{\partial(\Delta\Omega)}{\partial r}, \quad (2.3)$$

where ρ is the mass density, v_{\perp} is the perpendicular viscosity, and $\Delta\Omega$ is the deviation of the mode rotation from its "natural" value.

The electromagnetic torque is due to $\mathbf{J} \times \mathbf{B}$ forces arising from the mode's magnetic perturbation and an eddy current that is produced on the mode's resonant surface by some perturbing agent. If the current perturbation is produced by an agent outside the plasma, then the torque is an *external* torque, and through it angular momentum can be lost. If the current perturbation is produced by other modes, then the torque is an *internal* torque, which conserves angular momentum, i.e. $\int d^3x T_{em}^{NL} = 0$.

2.2.1.1 External electromagnetic torques

External torques on a mode come from field errors or deliberately applied magnetic perturbations that are resonant with the mode. Also, they can be due to induced eddy currents from

the mode in a resistive wall; these currents are out of phase with their source. These torques have the form:

$$T_{em}^{ext} = \int d^3x \left[\mathbf{R} \times (\mathbf{j}_k^{pert} \times \mathbf{b}_{-k}^{mode} + \mathbf{j}_k^{mode} \times \mathbf{b}_{-k}^{pert}) \right] = \int d^3x \left[\mathbf{R} \times (j_k^{pert} b_{-k}^{mode} + j_k^{mode} b_{-k}^{pert}) \right] \sin \delta, \quad (2.4)$$

where T_{em}^{ext} is the external electromagnetic torque, \mathbf{k} is the wavevector denoting the resonant surface, \mathbf{j}_k^{pert} is the current density perturbation induced on the resonant surface, \mathbf{b}_k^{mode} is the mode's magnetic field perturbation, \mathbf{j}_k^{mode} is the mode's current density perturbation, \mathbf{b}_k^{pert} is the induced magnetic field perturbation, and δ is the spatial phase between the mode and the applied perturbation. An important feature of the theory is that δ is nonzero only where resistivity becomes important, because only in these regions is the eddy current produced by the perturbation not in phase with magnetic field, which should also be true for internal torques (§ 2.2.1.2), for the various rational surfaces involved. It turns out that the current density and magnetic field in the resistive layer are related such that both terms in eq. 2.3 have the same form, differing by a constant, i.e. $\mathbf{j} \sim i\mathbf{k} \times \mathbf{B}/\mu_0$. Note also that the external torque is linear in the mode amplitude. Since MST has a thick (~ 5 cm) aluminum wall, torques due to the resistive wall are not expected to be very important.

2.2.1.2 Internal electromagnetic torques

Internal torques come from interactions between modes in the plasma. These can be produced by geometric coupling of modes in a toroidal system, or by nonlinear interactions between modes in arbitrary geometry. Torques produced by either mechanism produce similar effects on the plasma. For any internal torque, the mode that is being acted upon will also produce an equal and opposite torque on other modes (Newton's third law). Therefore, internal torques can only redistribute angular momentum, not remove it from the plasma.

2.2.1.2.1 Toroidal coupling.^{8,9}

In periodic cylindrical geometry, a mode can be fully separated in its coordinate dependences:

$$\Psi_{mn}(r, \theta, \phi) = \psi_{mn}(r) e^{i(m\theta - n\phi)}, \quad (2.5)$$

where Ψ is the mode's wavefunction, ψ is its radial eigenfunction, m is the azimuthal (poloidal-like) mode number, θ is the azimuthal angle, n is the axial (toroidal-like) mode number, and ϕ is the toroidal angle; in a cylinder $\phi = z/R$, where z is the axial distance, and $2\pi R$ is the periodicity length.

On the other hand, in a toroidal system, θ ceases to be an ignorable coordinate and only the ϕ -dependence can be separated out:

$$\Psi_n(r, \theta, \phi) = e^{-in\phi} \sum_m \psi_{mn}(r) e^{im\theta}, \quad (2.6)$$

for all resonant m , i.e. the wavefunctions depend on multiple resonant surfaces. There are still as many linearly independent eigenfunctions as there are resonant surfaces, but they are coupled. For example, in MST there are $m = 0$ and $m = 1$ (only) resonances for values of n between 5 and 10, e.g. 6. In the absence of toroidal coupling, the (0,6) and (1,6) modes are independent, so their eigenfunctions in the regions surrounding the respective resistive layers, where ideal MHD remains valid, can be expressed by the matrix equation

$$\begin{pmatrix} L_{0,6} & 0 \\ 0 & L_{1,6} \end{pmatrix} \begin{pmatrix} \psi_{0,6} \\ \psi_{1,6} \end{pmatrix} = 0, \quad (2.7)$$

where $\psi_{m,n}$ is the eigenmode for the $q = m/n$ resonance, and $L_{m,n}$ is an operator; it is singular where $q = m/n$. Note that there are no off-diagonal elements, because the modes are uncoupled. On the other hand, when toroidal effects become important, the matrix equation becomes

$$\begin{pmatrix} L_{0,6} & L_{0,6}^{1,6} \\ L_{1,6}^{0,6} & L_{1,6} \end{pmatrix} \begin{pmatrix} \psi_{0,6} \\ \psi_{1,6} \end{pmatrix} = 0, \quad (2.8)$$

where $L_{m,n}^{m',n'}$ is the geometric coupling operator between the $q = m/n$ cylindrical solution and the $q = m'/n'$ cylindrical solution. $L_{m,n}^{m',n'} \sim \varepsilon$, the inverse aspect ratio, or alternatively $\varepsilon\beta_p$. Note that eq. 2.7 is still diagonalizable, and will produce two eigenfunctions that each depend on the $q = 0$ and $q = 1/6$ resonances. Because they are determined by the same resonances, these two eigenmodes can produce torques on each other.

The torque on one mode in this case has the form

$$T_{em}^{TC} \sim R j_{\mathbf{k}}^{\mathbf{k}'} b_{-\mathbf{k}} \sin(\delta_{\mathbf{k}} - \delta_{\mathbf{k}'}), \quad (2.9)$$

where T_{em}^{TC} is the electromagnetic torque generated through toroidal coupling, $j_{\mathbf{k}}^{\mathbf{k}'}$ is the current induced on rational surface of the mode \mathbf{k} by the mode \mathbf{k}' , and $\delta_{\mathbf{k}}$ ($\delta_{\mathbf{k}'}$) is the phase of the \mathbf{k} (\mathbf{k}') mode.

2.2.1.2.2 Nonlinear torques.

Nonlinear contributions to the electromagnetic torque are due to interactions between the mode and the resonant current perturbation produced by pairs of other modes satisfying a wavevector sum rule.^{10,11} The nonlinear torque has the form:

$$T_{em}^{NL} \sim |\mathbf{R} \times \mathbf{j}_{\mathbf{k}}^{NL} \times \mathbf{b}_{\mathbf{k}}|, \quad (2.10)$$

where T_{em}^{NL} is the nonlinear electromagnetic torque, \mathbf{k} is the wavevector of the mode in question, $b_{\mathbf{k}}$ is the mode amplitude, and $j_{\mathbf{k}}^{NL}$ is the nonlinearly produced current density perturbation at the mode's rational surface. Eqns. (2.10) and (2.4) or (2.9) have the same form, but in (2.10) the current density is produced nonlinearly by other modes. The current density has the form:

$$j_{\mathbf{k}}^{NL} \approx \sum_{\mathbf{k}'} C_{\mathbf{k}', \mathbf{k}-\mathbf{k}'} b_{\mathbf{k}'} b_{\mathbf{k}-\mathbf{k}'} e^{i(\delta_{\mathbf{k}'} - \delta_{\mathbf{k}-\mathbf{k}'})}, \quad (2.11)$$

where $C_{\mathbf{k}',\mathbf{k}-\mathbf{k}'}$ are nonlinear coupling coefficients and $(\delta_{\mathbf{k}'}-\delta_{\mathbf{k}-\mathbf{k}'})$ is the phase difference between the modes with wavevectors \mathbf{k}' and $\mathbf{k}-\mathbf{k}'$. Therefore, the nonlinear torque has the form:

$$T_{em}^{NL} \sim R \sum_{\mathbf{k}'} C_{\mathbf{k};\mathbf{k}-\mathbf{k}'} b_{-\mathbf{k}} b_{\mathbf{k}} b_{\mathbf{k}-\mathbf{k}'}, \sin(\delta_{\mathbf{k}'} - \delta_{\mathbf{k}} + \delta_{\mathbf{k}-\mathbf{k}'}) . \quad (2.12)$$

For diagnostic reasons to be discussed in Chapter 3, it is difficult on MST to measure the phase differences and even some of the mode amplitudes for the toroidal coupling torque. Therefore, when the term ‘‘internal torques’’ is used, the nonlinear torque will be the mechanism that is emphasized.

2.2.2 Mode locking.

The term ‘‘locking’’ in this context means that a mode’s angular velocity is made to match that of some other entity through an electromagnetic torque, whether external or internal. It has been studied in many devices, examples of which can be found in Refs. 7 and-17. Typically, ‘‘locking’’ is used to describe the situation in which the mode comes to rest with respect to the device wall. However, the same mechanism underlies the flattening of the momentum profile produced by internal torques, or a mode being driven by an external rotating magnetic perturbation.^{18,19}

For detailed theoretical work behind mode locking, see Refs. 6 and 7. Rather than delving into the theory, an experimentalist’s view of the subject will be presented. The rotation of a mode can be expressed in the form

$$\frac{d^2\zeta}{dt^2} + \nu \left(\frac{d\zeta}{dt} - \omega_0 \right) + \kappa \sin\zeta = 0, \quad (2.13)$$

where ζ is the phase of the mode, ω_0 is the ‘‘natural’’ rotation rate, ν measures the viscous dissipation, and κ is a measure of the electromagnetic force. This equation is similar in form to that of a damped pendulum, so it is natural to make the analogy. A pendulum, in the absence of dissipation, can either exhibit rotation through a full 2π of angle, where gravity exerts an

sipation, can either exhibit rotation through a full 2π of angle, where gravity exerts an oscillatory torque depending on whether the pendulum is rising or falling, or oscillate in a restricted angular space. There is a critical point at which the pendulum makes the transition from rotation to oscillation.

Fundamentally, then, mode locking occurs because, in the presence of dissipation, for high enough mode or perturbation amplitude, i.e. electromagnetic torque (κ in eqn. 2.13), there is a bifurcation in the angular velocity, which can occur because $\kappa = \kappa(d\zeta/dt)$ for the mode, rather than being a constant as for the pendulum. The mode spontaneously makes a transition from rotating near its “natural” rate to very slow rotation with respect to the perturbing entity, at which point dissipative effects can come into play and remove the residual relative angular velocity. There is a hysteresis effect, as well, wherein the mode/perturbation amplitude must be reduced below the locking threshold for unlocking to occur.

2.3 RFP mode structure

Since the RFP has $|q| < 1$ everywhere, i.e. $m < n$ for resonant modes, there are essentially four classes of possible internally resonant modes to discuss. The standard cylindrical formalism will be adopted, except for one case to be noted later. The $m = 1$, low- n modes dominate the dynamics of the core of the plasma. The $m = 0$ modes govern the edge. These two types of modes are global in character, so they affect large portions of the plasma. Modes with $m > 1$ exist, but are primarily generated by toroidicity. There are also $m = 1$, high- n modes near the reversal surface that are small-wavelength, local fluctuations.

2.3.1 $m = 1$ modes

Modes which have poloidal mode number $m = 1$ are resonant inside the $q = 0$ surface. Of these modes, which are linearly unstable, the dominant ones are those with toroidal mode num-

ber $n \approx 2R/a$, with R and a being the major and minor radii, respectively. For MST, with $R = 1.5$ m and $a \approx 0.5$ m, the $m = 1$, $n = 5-9$ modes are dominant, with the largest being the (1,6) mode. These modes are typically phase-locked to each other¹⁵ and their islands overlap, as can be seen in Fig. 2.3. Because of the large scale of the overlap, the magnetic field is essentially stochastic throughout much of the plasma. There are modes with larger values of n that are resonant near the reversal surface, but they are of much smaller amplitude than the dominant ones.

2.3.2 $m = 0$ modes

The second class of global modes has $m = 0$, and $n = 1-4$ (or higher). These are resonant where the toroidal field reverses ($q = 0$) (cf. Fig. 2.3). The drive for these modes is not yet determined; they may be nonlinearly driven, or linearly unstable. Of these, by far the largest is the $n = 1$ mode. It has been observed that the $m = 0$ modes are normally locked or slowly rotating in MST plasmas. The presence of internally resonant $m = 0$ modes in the RFP means that the nonlinear electromagnetic torque will include terms involving adjacent (in n) $m = 1$ modes and

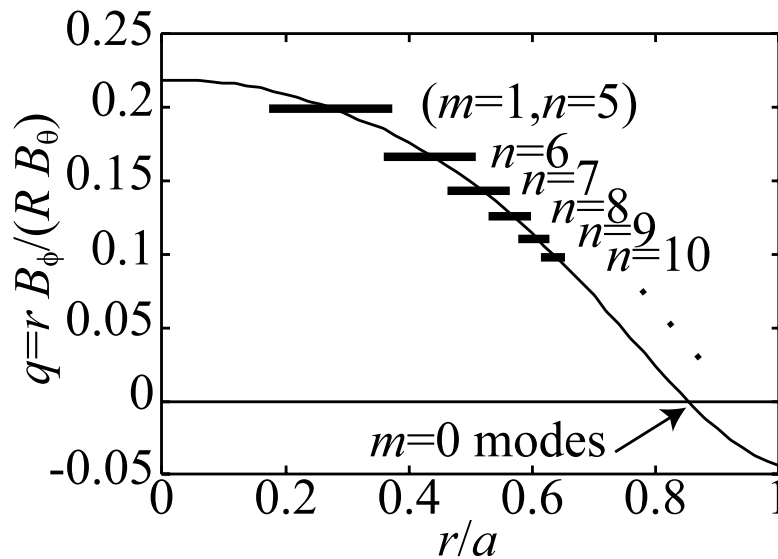


Figure 2.3. Calculated q profile for MST-like parameters, showing estimated $m=1$ island widths.

the ($m = 0, n = 1$) mode.

The presence of an $m = 0$ resonance allows for large nonlinear torques in the RFP. This is because the $(1, n)$ mode can couple with the $(1, n')$ mode through the $(0, \Delta n = n - n')$ mode, which is resonant for all Δn , and large in amplitude for small Δn (e.g. 1).

2.3.3 $m \geq 2$ fluctuations.

There is also the possibility for internally resonant modes with $m \geq 2$, and large values of n . Although $m = 2$ fluctuations have previously been reported for MST,⁵ more recent measurements indicate that independent fluctuations with $m \geq 2$ are small; the $m = 2$ spectrum is mainly generated from the $m=1$ modes from toroidicity. These results are similar to what was previously reported for the HBTX-1A RFP²⁰. A brief digression here is in order.

Using a poloidal array of magnetic pickup coils (to be discussed in Chapter 3), the frequencies of the $m = 1$ and $m = 2$ fluctuations (averaged over all n) were measured. If such fluctuations were generated through nonlinear coupling between two $m = 1$ modes, then their frequency would be approximately double that of the $m = 1$ modes, i.e.

$$b_{m=2}^{NL} \sim e^{i(\theta - n_1 \phi - \omega_{n_1} t)} e^{i(\theta - n_2 \phi - \omega_{n_2} t)} \sim e^{i[2\theta - (n_1 + n_2)\phi - (\omega_{n_1} + \omega_{n_2})t]}, \quad (2.10)$$

where $\omega_{n_1} \approx \omega_{n_2} \Rightarrow \omega_{n_1} + \omega_{n_2} = 2\omega_{n_1}$ or $2\omega_{n_2}$. However, what is actually seen (Fig. 2.4) is that the $m = 1$ and $m = 2$ rotation track each other closely.

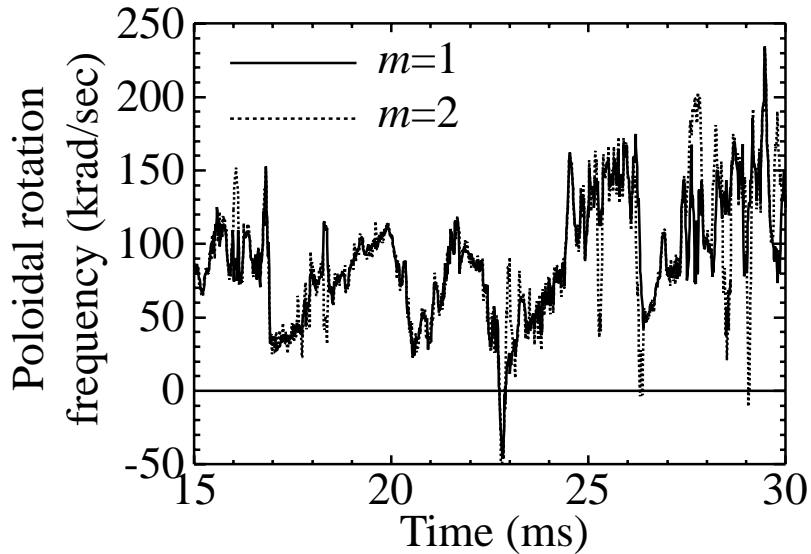


Figure 2.4. $m = 1$ and $m = 2$ rotation frequencies. They are essentially identical.

To understand whether the effect could be due simply to calibration errors in the coils, it was necessary to measure the power spectra of the $m = 1$ and $m = 2$ fluctuations over an ensemble of events, using a technique to be described in Chapter 3. The results are plotted in Fig. 2.5. The observed $m = 2$ power is too large to be due to coil calibration errors, which should give about 1% in the power spectrum for a 10% uncertainty in area. Therefore, what is seen is really $m = 2$ fluctuation.

Clearly, between 5 and 25 kHz, the $m = 2$ spectrum appears to be a scaled down version of the $m=1$ spectrum. This appears to be a toroidal effect:

$$b_{m=2}^{TC} \sim \cos \theta e^{i(\theta - n\phi - \omega t)} \sim e^{i[2\theta - n\phi - \omega t]}, \quad (2.11)$$

i.e. the frequency of the $m = 2$ mode is the same as that of the generating $m=1$ mode. There is a feature in the $m = 2$ spectrum between 25-40 kHz that could well be independent nonlinearly driven fluctuations. However, the power here is two orders of magnitude below the peak in the $m = 1$, and more than an order below the peak in the $m = 2$.

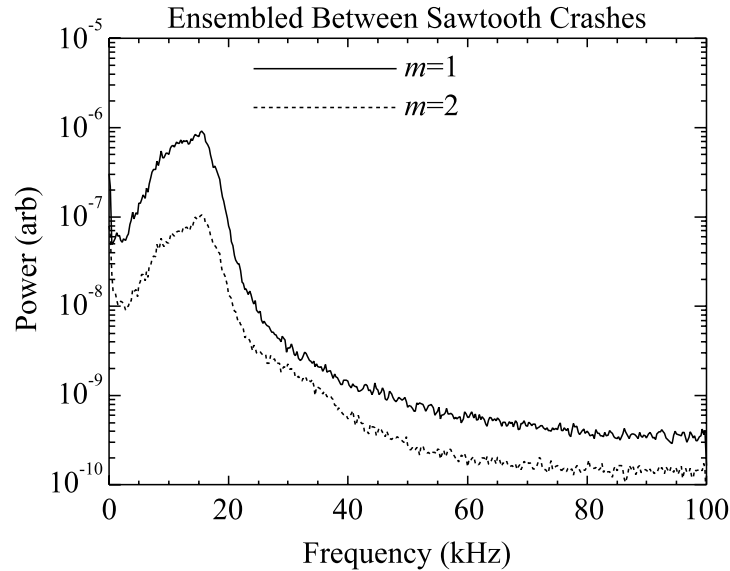


Figure 2.5. $m = 1$ and $m = 2$ power spectra. Between 5 and 25 kHz, the $m = 2$ spectrum is a scaled down version of the $m = 1$.

The conclusion is that fluctuations with $m \geq 2$ do exist but primarily arise from the $m = 1$ modes through toroidicity rather than nonlinear coupling. The effects of nonlinear coupling through the $m = 2$ channel will be ignored in further discussions.

2.3.4 High- n fluctuations

There are resonances that lie near the $q = 0$ radius. The modes at these surfaces have large values of n , implying small wavelength. These are not, therefore, global modes, and play no significant role in the electromagnetic torque, so they will not be discussed further.

2.4 The RFP sawtooth cycle²¹

Most quantities in MST plasmas exhibit dramatic changes during the so-called sawtooth cycle. The kinematics of the modes are no exception, and this will be the major focus of Chapter 5. The sawtooth cycle in MST is characterized by rapid flux generation through a dynamo process,^{22,23,24,25} followed by a quiescent period that culminates in another flux generation event, repeated for much of the discharge. A sample discharge is shown in Fig. 2.6. Figures 2.6(a) and 2.6(b) show the toroidal flux generation, with slow time behavior in the average toroidal field,

and fast behavior in the toroidal field at the wall. The rapid flux generation phases will hereafter be referred to as sawtooth “events” or “crashes”.

From the point of view of this dissertation, the most important features of the sawtooth cycle are a rapid increase in the amplitudes of the tearing modes and deceleration and acceleration of the $m = 1$ modes. In Fig. 2.6(c) is plotted the toroidal phase velocity of the ($m = 1, n = 6$) mode. The other $m = 1$ modes have similar behavior. There is a rapid ($\sim 100 \mu\text{s}$) deceleration at the sawtooth crash, which typically ends with the mode rotating very slowly or not at all. This has been described as a temporary mode locking phenomenon.²⁶ The crash phase is followed in many cases by a slower (few ms) reacceleration phase. However, the slow reacceleration does not always occur—sometimes the modes do, in fact, lock permanently to the wall.

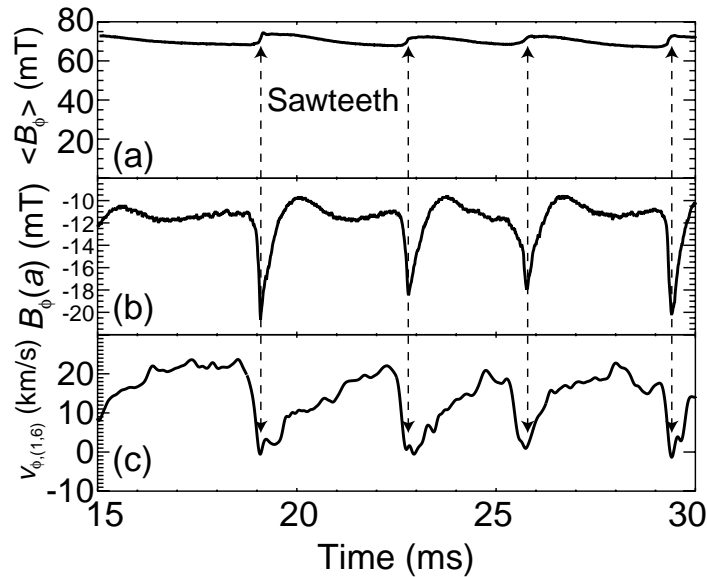


Figure 2.6. Sawtooth cycle behavior of (a) the volume-averaged toroidal field, (b) the toroidal field at the wall, and (c) the toroidal phase velocity of the (1,6) mode.

2.5 Summary

Plasma resistivity allows for instabilities such as tearing modes to appear that can alter the magnetic topology through reconnection. Electromagnetic forces, or torques in circular geometry, can be exerted on these modes by other perturbations, whether they are external sources or other modes, if the perturbations are out of phase with the mode. The phenomenon of mode locking is due to these forces/torques.

The RFP magnetic configuration provides a unique laboratory setting to study the kinematics of tearing modes. There are several modes active in typical RFP plasma. In addition, the mode numbers of the largest modes $[(0,1), (1,6), (1,7)]$ are such that nonlinear three-wave interactions can become quite important. These modes become very large during sawtooth crashes, so nonlinear effects are expected to be quite important.

References:

- ¹ S. Ortolani and D. D. Schnack, *Magnetohydrodynamics of Plasma Relaxation*, World Scientific Publishing Co., Singapore, (1993).
- ² H. A. B. Bodin, A. A. Newton, Nucl. Fusion **20**, 1255 (1980).
- ³ H. A. B. Bodin, Nucl. Fusion **30**, 1717 (1990).
- ⁴ S. Ortolani, Plasma Phys. Controlled Fusion **31**, 1665 (1989).
- ⁵ S. Assadi, S. C. Prager, and K. L. Sidikman, Phys. Rev. Lett. **69**, 281 (1992).
- ⁶ R. Fitzpatrick, T. C. Hender, Phys. Fluids B **3**, 644 (1991).
- ⁷ R. Fitzpatrick, Nucl. Fusion **33**, 1049 (1993).
- ⁸ J. W. Connor, R. J. Hastie, and J. B. Taylor, Phys. Fluids B **3**, 1532 (1991).
- ⁹ R. Fitzpatrick, R. J. Hastie, T. J. Martin, and C. M. Roach, Nucl. Fusion **33**, 1533 (1993).
- ¹⁰ C. C. Hegna, Phys. Plasmas **3**, 4646 (1996).
- ¹¹ R. Fitzpatrick, Phys. Plasmas **6**, 1168 (1999).
- ¹² J. T. Scoville, R. J. La Haye, A. G. Kellman, T. H. Osborne, R. D. Stambaugh, E. J. Strait, and T. S. Taylor, Nucl. Fusion **31**, 875 (1991).
- ¹³ M. Talvard, R. E. Bell, S. Bernabei, S. Kaye, M. Okabayashi, S. Sesnic, and S. von Goelert, Plasma Phys. Con-

trolled Fusion **38**, 705, (1996).

¹⁴ A. F. Almagri, S. Assadi, S. C. Prager, J. S. Sarff, and D. W. Kerst, Phys. Fluids B **4**, 4080 (1992).

¹⁵ Y. Yagi, H. Sakakita, T. Shimada, K. Hayase, Y. Hirano, I. Hirota, S. Kiyama, H. Koguchi, Y. Maejima, T. Osakabe, Y. Sato, S. Sekine, and K. Sugisaki, Plasma Phys. Controlled Fusion **41**, 255, (1999).

¹⁶ S. Mazur, Phys. Plasmas **1**, 3356, (1994).

¹⁷ A.K Hansen, A.F. Almagri, D. J. Den Hartog, S.C. Prager, and J. S. Sarff, Phys. Plasmas **5**, 2942 (1998).

¹⁸ G.A Navratil, C. Cates, M.E. Mauel, D. Maurer, D. Nadle, E. Taylor, Q. Xiao, W.A. Reass, G.A Wurden, Phys. Plasmas **5**, 1855 (1998).

¹⁹ R. Bartiromo, T. Bolzonella, A. Buffa, G. Chitarin, S. Martini, A. Masiello, S. Ortolani, R. Piovan, P. Sonato, and G. Zollino, Phys. Rev. Lett. **83** 1779 (1999).

²⁰ I. H. Hutchinson, M. Malacarne, P. Noonan, and D. Brotherton-Radcliffe, Nucl. Fusion **24**, 598 (1984).

²¹ S. C. Prager, A. F. Almagri, S. Assadi, J. A. Beckstead, R. N. Dexter, D. J. Den-Hartog, G. Chartas, S. A. Hokin, T. W Lovell, T. D. Rempel, J. S. Sarff, W. Shen, C. W. Spragins, and J. C. Sprott, Phys. Fluids B **2**, 1367 (1990).

²² H Ji, S. C. Prager, A. F. Almagri, J. S. Sarff, Y. Yagi, Y. Hirano, K. Hattori, and H. Toyama, Phys. Plasmas **3**, 1935 (1996).

²³ J. T. Chapman, Ph. D. thesis, University of Wisconsin—Madison (1998).

²⁴ D. J. Den Hartog, J. T. Chapman, D. Craig, G. Fiksel, P. W. Fontana, S. C. Prager, and J. S. Sarff, Phys. Plasmas **6**, 1813 (1999).

²⁵ P. W. Fontana, Ph. D. thesis, University of Wisconsin—Madison (1999).

²⁶ D. J. Den Hartog, A. F. Almagri, J. T. Chapman, H. Ji, S. C. Prager, and J. S. Sarff, Phys. Plasmas **2**, 2281 (1995).

3 Experimental Considerations.

The discussion will now turn to the hardware that was used. First will be the equipment needed to apply magnetic perturbations to the plasma, including the coils and the power supplies. Next is a discussion of the magnetic pickup coils that are used to measure the amplitudes of the modes. For the experiments that involved perturbations at the toroidal gap, calibrating the applied field at the edge of the plasma to the measured currents in the coils was necessary. The final section is a discussion of special analysis techniques that were used.

3.1 Tools for Active Experiments

3.1.1 Shell gaps and coils at gaps

Because MST has a 5 cm thick aluminum shell, external magnetic perturbations with timescales in the millisecond range must be applied at either the poloidal gap or the toroidal gap in the shell.

3.1.1.1 Poloidal gap

The purpose of the poloidal gap is to allow the toroidal plasma current to be driven. Because there are substantial field errors at this gap, there are various sets of coils that pass through a flange at this gap to reduce various components of the field error. These coils typically consist of a twisted pair of transmission lines, forward and return wires that pass through the holes in the poloidal flange, and a connecting piece that lies on the flange between the holes. Only the magnetic field that enters or leaves the gap is important because of the long skin time of the shell. Figure 3.1 shows the location where some of these coils pass through the poloidal flange.

It was chosen to co-opt the “correction coils” (Fig. 3.1) for most of the static perturbation experiments because they are close to the plasma, and can be configured to output a variety of

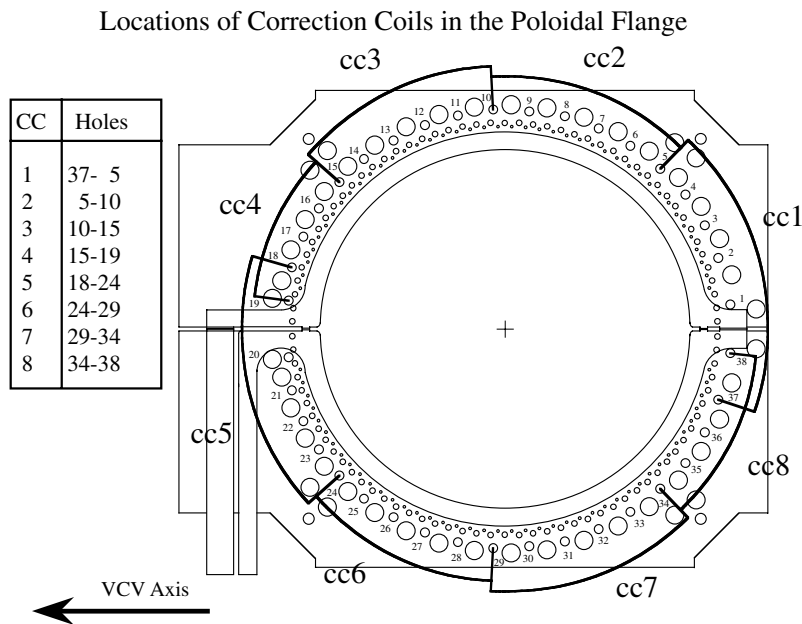


Figure 3.1. Poloidal flange, showing the locations of the correction coils.

harmonics ($m = 0, 1, 2,$ and 4). Another experiment used an extra set of $m = 0$ coils that are wound outside of the poloidal flange (Fig. 3.2).

3.1.1.2 Toroidal gap

The toroidal gap exists to allow the current that produces the toroidal field to flow in the shell. To apply perturbations at the toroidal gap it was decided to put wires through the 1/4" holes that pierce the toroidal flange and gap. Because the ~ 1 cm wide gap is narrow with respect to the major circumferences of MST, ~ 10 m, the poloidal spectrum is broad. See Ref. 1 for an analytic cylindrical calculation of the spectrum. Only the $m = 0$ and $m = 1$ harmonics are resonant; the rest of the power in the perturbation does not go into producing electromagnetic torque. Figure 3.3 shows a schematic of the $n = 6$ coils. The two coils are 90° spatially out of phase with one another, so they can produce a rotating $n = 6$ perturbation. The coils are wound such that the other toroidal harmonics that are produced should be primarily integer multiples of 6—no significant $n = 5, 7,$ or 8 .

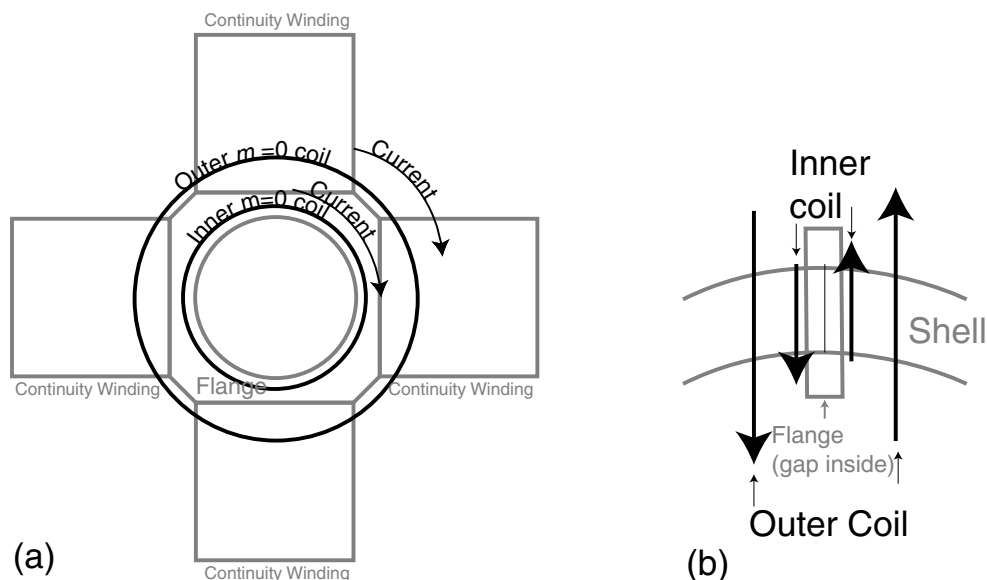


Figure 3.2. Cartoon of external $m = 0$ coils (a) side view, showing directions of currents (b) top view, many intervening parts removed for clarity, showing directions of currents.

3.1.2 Power supplies

3.1.2.1 Static perturbation

One set of experiments that were performed utilized magnetic perturbations that were static in space but impulsive in time. The power supply used for the static perturbation experiments uses a discharging capacitor bank. Currents up to about 9 kA can be generated with 800 V on the capacitors, so the peak power is 7.2 MW. The output pulse that is generated is about 5 ms FWHM. A current trace from this supply is shown in Fig. 3.4.

3.1.2.2 Rotating magnetic perturbation (RMP)

Another set of experiments involved applying a rotating perturbation to the $n = 6$ coils. The signal source is a two-output function generator with variable relative phase between the outputs. In this manner the coils can be tuned into phase quadrature simply by adjusting the phase at the signal generator rather than adjusting resonant circuit elements (i.e. inductance and capacitance) attached to the coils. The function generator outputs pass through a first stage of

amplification, which for each channel is a commercial power amplifier. These are in turn connected to a “drift-pump” amplifier, which functions as a Class C audio frequency amplifier.

A matching network is attached to each coil to match its impedance to that of the power supply so that it may be driven with the maximum possible current. Because the load (matching network and coils) is reactive in nature, the system is tuned to be operable at a single frequency.

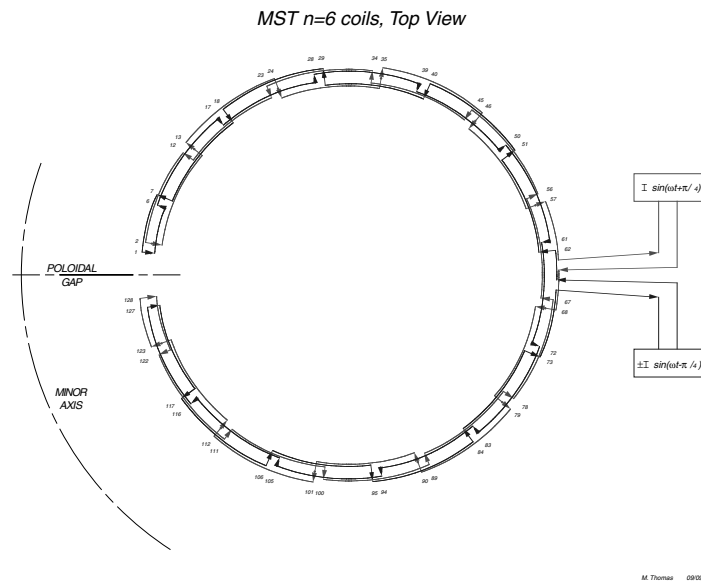


Figure 3.3. $n = 6$ coil schematic.

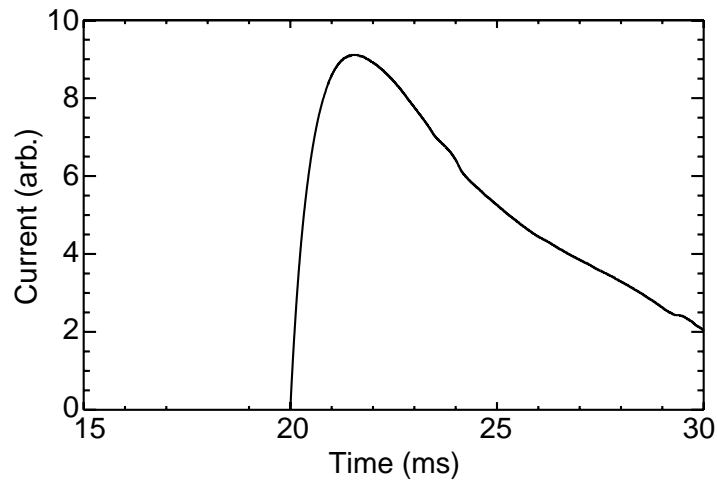


Figure 3.4. Current from static perturbation power supply.

The frequency that was used was 10.08 kHz, which is within the range of typical (1,6) mode rotation frequencies seen on MST. Figure 3.5 shows a circuit diagram for one amplifier and coil, and Figure 3.6 is a cartoon of the whole system, showing the matching networks.

3.2 Diagnostics

3.2.1 Magnetic arrays

MST has several arrays of sets of internal magnetic coils to measure magnetic fluctuations. These coils are attached to the inside of the wall. The outputs of these coils are typically

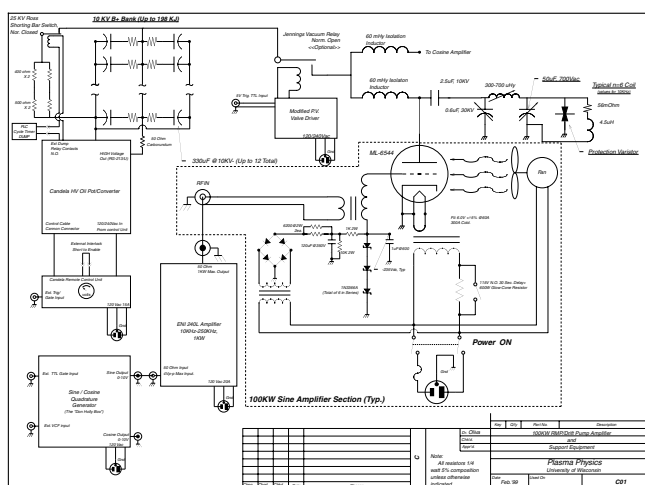


Figure 3.5. Circuit diagram for rotating magnetic perturbation amplifier.

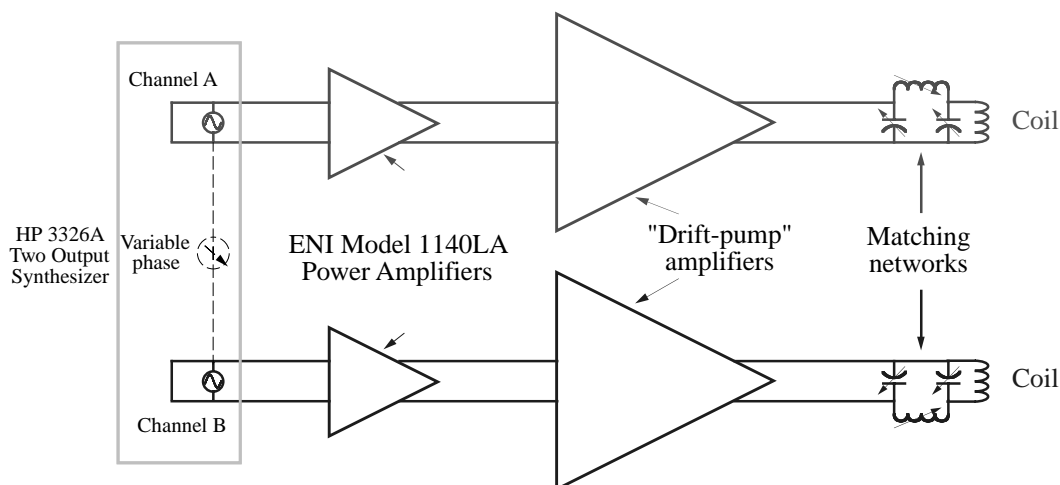


Figure 3.6. Cartoon of entire RMP system.

analog integrated so that the magnetic field rather than its time derivative is measured. Some use tri-axial coil forms, which have radial, poloidal and toroidal coils.² There are two poloidal arrays of equally spaced coil forms at 155° and 180° toroidal, having 8 and 16 forms respectively. The 180° poloidal array was used for the measurement of the $m = 2$ frequency in § 2.3.3.

In addition, there is a toroidal array of 64 equally spaced forms. This is the primary diagnostic tool used for the work in this dissertation. For this work 32 toroidal and 32 poloidal coils of the toroidal array were used. The toroidal mode spectra are extracted from the raw data through a discrete Fourier transform. Figure 3.7(a)³ shows an illustration of the location of one of the coils in this array in a poloidal plane, and an expanded view is shown in Fig 3.7(b).

In addition to the arrays of tri-axial coils, there is an array of 32 bi-axial forms at the poloidal gap, having radial and poloidal pickup coils.⁴ These coils straddle the poloidal gap (see Fig. 3.8). For the work in this dissertation, 8 or 16 of the radial coils (depending on the general

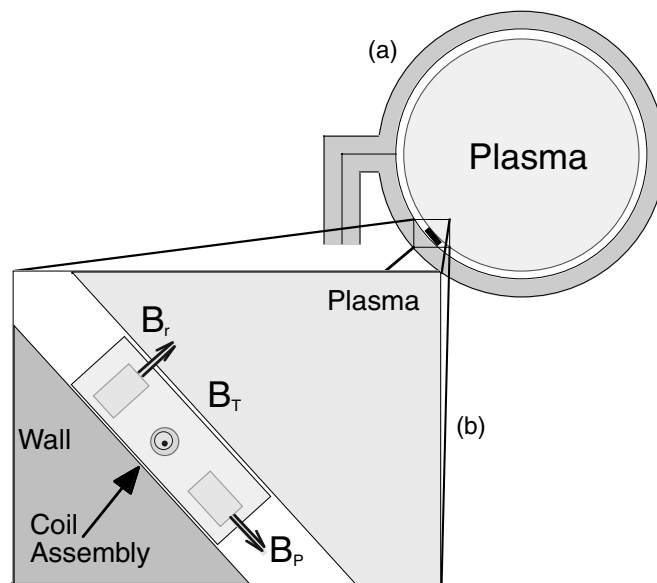


Figure 3.7. (a) Position of toroidal array in vacuum vessel. (b) View of individual coil form.

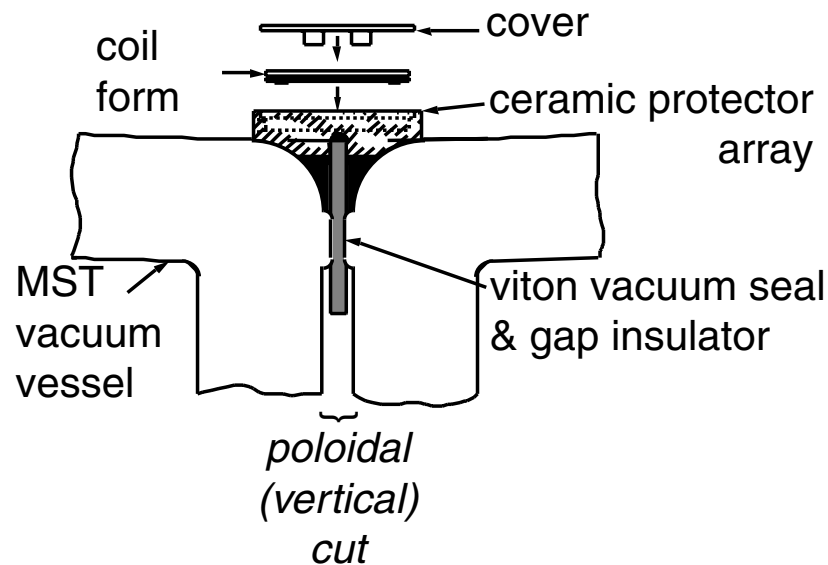


Figure 3.8. Layout for coil forms used at the poloidal gap.

MST run needs) were used. The raw data were Fourier transformed to get poloidal harmonic information.

3.2.1.1 Toroidal array coil calibration

Because of uncertainties in the areas and orientations of the coils in the toroidal array, a shot by shot recalibration method has been used. For the poloidal field coils, the toroidal field pickup is removed by looking at the signals before the discharge when the toroidal field is turned on, but before the plasma current and therefore poloidal field starts. Then the relative areas of the coils are found by removing the stationary component, presumed due to systematic errors in the tabulated coil areas, during a period of the discharge in which rotation of the modes occurs.

To correct the toroidal pickup coils, the averaged field from the poloidal field coils is subtracted off, using a normalization derived from discharges where the average toroidal field at the wall was zero, as measured from the current in the shell, so that any signal in the edge toroidal pickup coils is due to poloidal field pickup. The relative areas are found by renormalizing to a separate measurement of the vacuum toroidal field at the wall.

For the poloidal gap radial field pickup coils, no such recalibration is performed. There is not a significant vacuum toroidal or poloidal field pickup in these coils, and their areas are better known, so these signals are just used directly.

3.2.1.2 Determination of mode helicity

Based on knowledge of the mode spectrum and equilibrium in MST, it is possible to figure out the helicities of the larger modes without a full 2D decomposition—using the toroidal and poloidal coils of the toroidal array is sufficient. It will be shown that the amplitudes of the ($m = 0, n = 1-4$) and ($m = 1, n = 5-9$) modes can be found directly from the coils.

The starting point is to determine which $m = 1$ mode has the smallest resonant n . This can be done through equilibrium modeling to find q on the magnetic axis. For nonpositive values of the toroidal field at the wall $n_{min} \geq 5$ for resonant modes. It may therefore be assumed that any internally resonant mode with $n < 5$ has $m = 0$. In addition, there are no resonant $m > 1$ modes for $n < 10$.

In addition, the poloidal field coils should not pick up $m = 0$ fluctuations. To show this requires the fixed boundary condition that the radial component of the current vanish at the wall, i.e. (in cylindrical geometry):

$$0 = \mu_0 j_r = \hat{\mathbf{e}}_r \cdot \nabla \times \mathbf{b}|_{r=a} = \frac{1}{a} \frac{\partial b_\phi}{\partial \theta} - \frac{1}{R} \frac{\partial b_\theta}{\partial \phi}, \quad (3.1)$$

where \mathbf{b} is the vector magnetic field fluctuation, $\hat{\mathbf{e}}_r$ is the unit vector in the minor radial direction, R is the major radius, and a is the minor radius. For $b_\theta, b_\phi \sim e^{i(m\theta+n\phi)}$, eqn. 3.1 reduces to

$$\frac{m}{a} b_\phi - \frac{n}{R} b_\theta = 0 \Rightarrow \frac{b_\theta}{b_\phi} = \frac{ma}{nR}. \quad (3.2)$$

Clearly, there should be no b_θ for $m = 0$ fluctuations. In toroidal geometry, the situation is more complicated, since m is no longer a good quantum number. To make matters simpler, the cylindrical convention, which is standard for use on MST, will be adopted, and the results from eqn. 3.2 used.

The net result is that the toroidal pickup coils can be used for the $m = 0$, $n = 1-4$ modes, and the poloidal pickup coils for the $m = 1$, $n = 5-9$ modes without picking up modes of different m for the same n . This has been experimentally verified by calculating average m values for different n .⁵ In addition, to get the total fluctuation amplitude at the wall of an $m = 1$ mode, the polarization from (3.2) can be used, and the fact the measured radial field at the wall is essentially zero:

$$|\mathbf{b}| = \sqrt{b_r^2 + b_\theta^2 + b_\phi^2} = b_\theta \sqrt{1 + \left(\frac{na}{mR}\right)^2}, \quad (3.3)$$

where this is done because the b_ϕ measurement also contains information from the $m = 0$ modes, which is difficult to deconvolve. When $m = 1$ mode amplitudes are quoted, eqn. 3.3 will be the method used to determine them. For $m = 0$ modes, the quoted amplitudes will be those evaluated from the toroidal pickup coils.

For n values where the $m = 0$ and $m = 1$ harmonics are both resonant, e.g. $n = 6$, the toroidal pickup coils receive a combination of the $m = 0$ and $m = 1$ harmonics at that n . It is difficult to separate the different poloidal harmonics, so the ($m = 0$, $n \geq 5$) modes are not resolved. For this reason, as well as that the (0,6) mode should be small, when the internal electromagnetic torque on the (1,6) mode (Chapter 5) is discussed, the focus will be on the nonlinear process.

3.2.2 Calibration of perturbation amplitude at toroidal gap

3.2.2.1 Measurements

The major diagnostic difficulty with applying a perturbation at the toroidal gap versus the poloidal gap is that there are no pickup coils available to measure the applied magnetic field. In order to compensate for this limitation, simultaneous measurements were made of the vacuum magnetic field put out by the RMP coils and the currents in each coil, thereby providing the ratio of vacuum magnetic field produced to applied current. The currents were measured with a current transformer around each coil. Measurements were made of the vacuum field inside the vacuum vessel, and that inside the toroidal flange, as well. The two $n=6$ coils were driven in phase quadrature with the AC function generator (cf. § 3.1.2.2), just as was done in the RMP experiments with a plasma present (§ 4.2), in all cases.

3.2.2.1.1 Measurement of magnetic field within the toroidal flange.

The field within the flange was measured by use of a probe that was designed to be inserted into one of the leak-checking holes at the poloidal gap, which are also 1/4" holes.⁶ The probe has two orthogonal coils that were used to measure the radial and toroidal magnetic field components. Figure 3.9 shows a sketch of the probe's layout, showing the electrostatic shielding, insulation, and coil form.

The construction of the $n = 6$ coils entails that there are four unused leak-checking holes between each pair of conductors (cf. Fig. 3.3). When the system is run in perfect quadrature there is an additional symmetry between the magnetic fields put out by each coil, ignoring the phase difference between them. Thus, there are only two possible AC magnetic measurements—the field one hole or two holes away from a wire. Figure 3.10 is a sketch of this, showing the probe inserted in a hole.

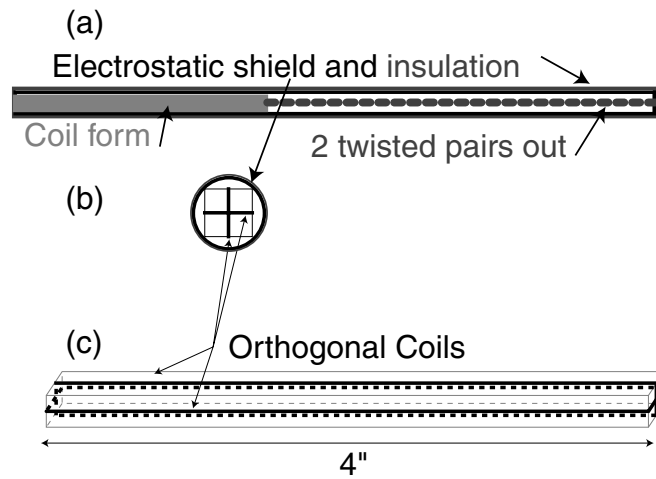


Figure 3.9. Sketch of 1/4" hole probe showing coil form, electrostatic shielding, and insulation (a) side view, (b) end view. (c) Close-up of coil form.

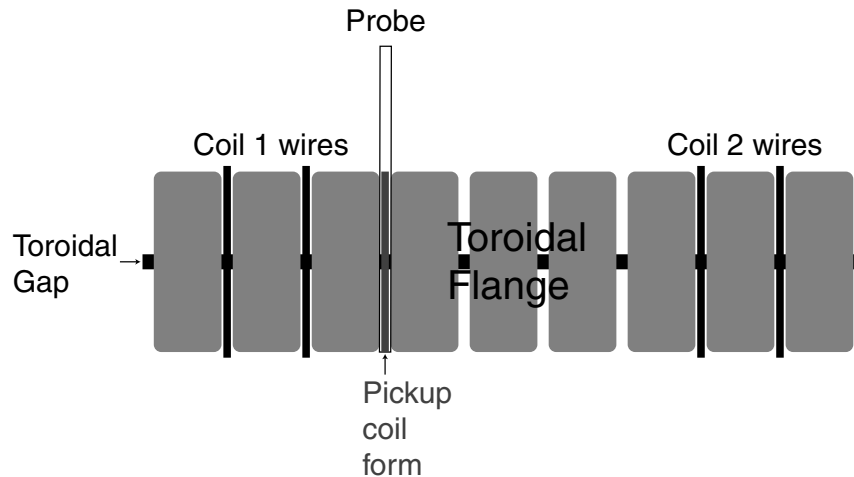


Figure 3.10. Sketch of toroidal flange layout, showing $n = 6$ coils and probe inserted into a hole.

Because not much flux soaks into the flange at the RMP operating frequency, the effective area of the coil is given by $A_{eff} = 2 d w$, where $d = 1.27$ cm is the gap width, $w = 2-2.5$ mm is the width of the coil along its short axis, and the factor of 2 is because there are two turns of wire in the coil. Thus $A_{eff} = 5.08-6.35$ cm².

In addition, a single-turn flux loop was constructed which encompassed half a spatial period of one of the $n = 6$ coils (Fig. 3.11). Because the coil is large, it gives an average measure of

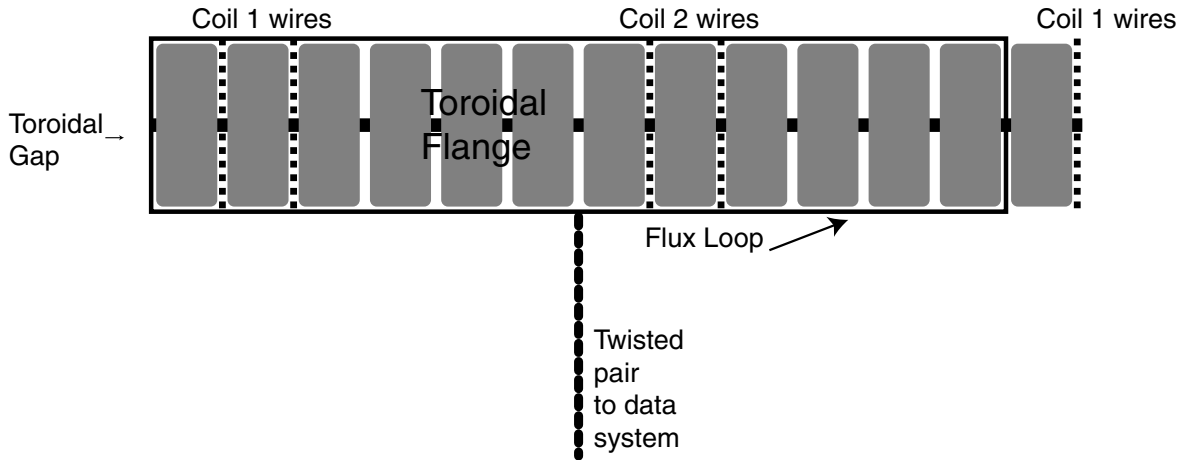


Figure 3.11. Sketch of toroidal flange layout, showing $n = 6$ coils and half-period flux loop.

the radial field from applied magnetic perturbation, smoothing over the locally large fields that exist close to the wires. The portions of the loop that are on top of the flange are pulled out to minimize contamination from flux leaking from the wires on top and on the bottom of the flange.

By similar arguments as were given for the probe measurement, the effective area of the flux loop can be expressed as $A_{eff} = R \phi d$, where $d = 1.27$ cm is the gap width, $R = 91.5$ cm is the major radius of the leak-checking holes, and $\phi = \pi/6$ is the toroidal angle subtended by the loop. Thus $A_{eff} = 60.8$ cm².

As is frequently the case for magnetic measurements on MST, the signals from the probe and flux loop were analog integrated before being digitized. The ~ 10 kHz RMP drive frequency is well within the ~ 250 kHz bandwidth of the integrators. All signals were digitized at 200 kHz. The currents in each coil were measured with current transformers and digitized at the same rate as the magnetic signals.

Figure 3.12(a) shows data from the flux loop and the probe's radial and toroidal coils when the probe was inserted one hole away from one of the $n = 6$ coils. These data are

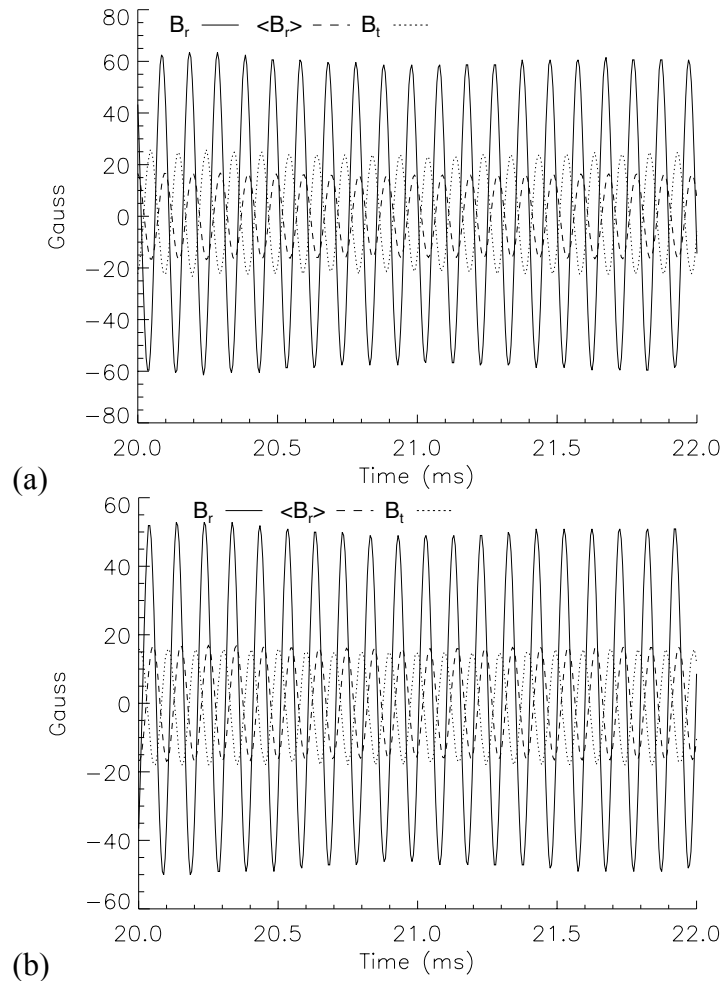


Figure 3.12. Data for magnetic fields in the toroidal flange, for (a) a hole next to an $n = 6$ coil, and (b) for two holes away from a coil.

calculated using the minimum of the range of probe coil areas. The local toroidal field, as measured by the probe, is a factor of ~ 3 smaller than the local radial field, and the average radial field, as measured by the flux loop, is a factor of ~ 4 smaller. The same quantities are shown in Fig. 3.12(b) for the case of the probe inserted two holes away from an $n = 6$ coil. In this case, the local toroidal field is approximately equal in magnitude to the average radial field from the flux loop, and the local radial field has decreased from ~ 60 to ~ 50 Gauss. The calibration results from this measurement are summarized in Table 3.1. The flux loop measurement of 0.0375 G/A will

	One hole away	Two holes away
Peak current—I	400 Amps	400 Amps
Peak local B_r	48-60 Gauss	40-50 Gauss
Peak local B_t	12-15 Gauss	20-25 Gauss
Peak $\langle B_r \rangle$ (from flux loop)	15 Gauss	15 Gauss
B_r/I	0.12-0.15 Gauss/Amp	0.10-0.125 Gauss/A
B_t/I	0.03-0.0375 Gauss/Amp	0.05-0.0625 Gauss/Amp
$\langle B_r \rangle/I$	0.0375 Gauss/Amp	0.0375 Gauss/Amp

Table 3.1. Calibration data for RMP toroidal flange field measurements.

probably provide a more relevant comparison with the internal measurement (§ 3.2.2.1.2) than do the local probe measurements because it averages over the locally large fields.

3.2.2.1.2 Measurement of the magnetic field within the vacuum vessel

To measure the field within the vacuum vessel, a probe was employed that was originally constructed to measure vacuum fields on the Tokapole II experiment.⁷ As can be seen in Fig. 3.13(a), the probe has four radial, poloidal and toroidal coils. It was inserted through a 4-1/2" port and placed within the vacuum vessel such that the axis of the radial pickup coil was centered on the toroidal gap [Fig. 3.13(b)]. All of the radial coils were used, as well as the two outermost toroidal coils. The second poloidal coil was also used. In order to ensure that the coils were centered on the gap, measurements were taken in which the probe was elevated and lowered. No substantial changes in the fields were seen.

In Fig. 3.14 are plotted the time series for the largest available signal of each of the three components of the magnetic field, to show the relative size and phase relations. As expected, the

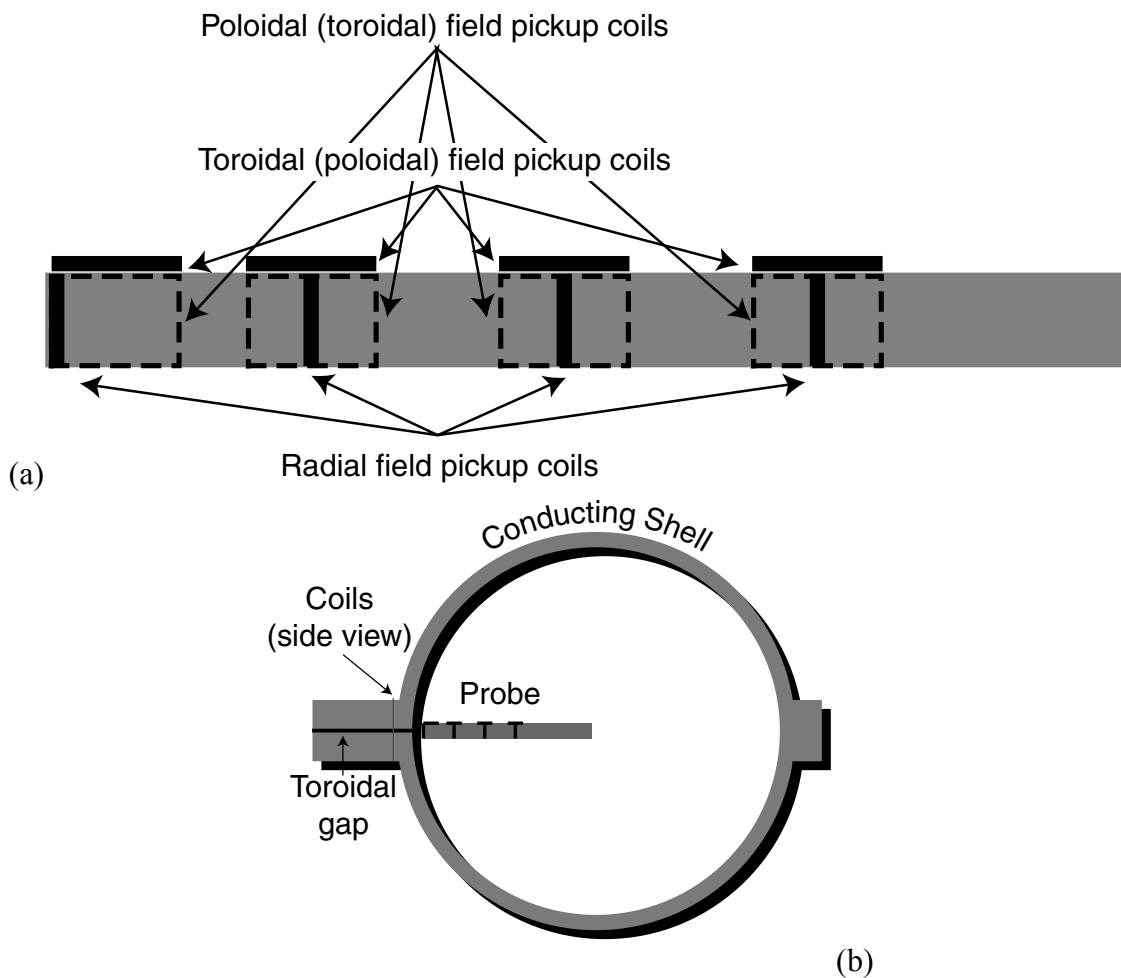


Figure 3.13. (a) Sketch of probe used for internal magnetic measurements. (b) Cartoon of probe setup for measurement.

poloidal field is very small near the midplane. It is not zero, however. The poloidal coil is was not exactly on the midplane, because the toroidal, poloidal and radial coils are not concentric (see Fig. 3.12). B_p and B_r look to be nearly in phase, and B_t is crudely 90° out of phase, which is what one expects to satisfy $\nabla \cdot \mathbf{B} = 0$.

In Fig. 3.15 the peak measured magnetic field amplitudes inside the vacuum vessel are plotted versus radius. The B_r profile shows a large falloff region near the edge, which is what

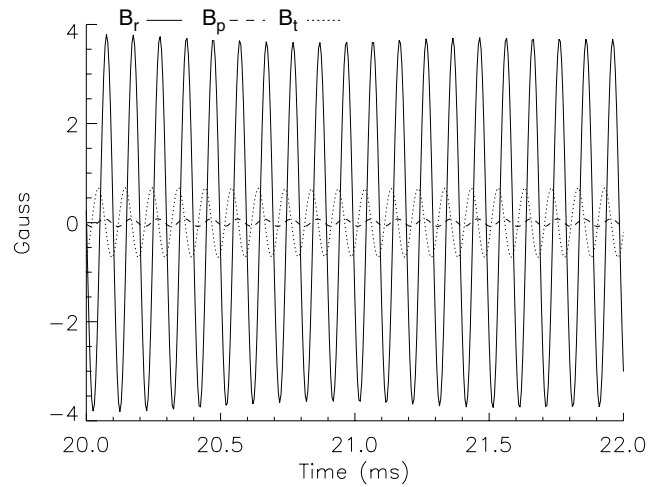


Figure 3.14. Data from internal probe measurements, largest signal for all components.

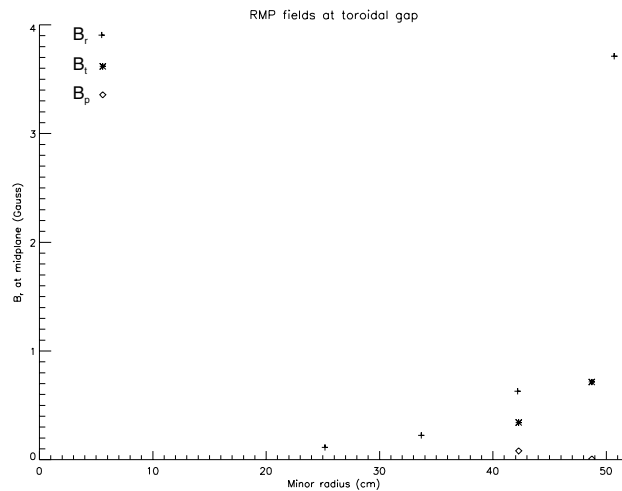


Figure 3.15. Radial profiles of measured magnetic field components amplitudes inside the vacuum vessel.

one would expect by comparing to the analytic calculation from Ref. 1. The B_t profile shows a smaller falloff.

The results of these measurements are summarized in Table 3.2. A radius of 50.07 cm is essentially at the edge of the plasma, assuming a 1 cm limiter, so the radial field at this radius will be used henceforth as the edge radial field. The magnetic field is much smaller than what is

Peak B_r (50.07 cm from axis)	3.5 Gauss
Peak B_r (42.175 cm)	0.6 Gauss
Peak B_r (33.675 cm)	0.22 Gauss
Peak B_r (25.175 cm)	0.1 Gauss
Peak B_t (48.725 cm)	0.7 Gauss
Peak B_t (42.275 cm)	0.35 Gauss
Peak B_p (42.275 cm)	0.07 Gauss
Peak current—I	300 Amps
$B_r(50.07 \text{ cm})/I$	0.0117 Gauss/Amp

Table 3.2. Summary of results from measurement of RMP magnetic fields inside the MST vacuum vessel.

seen in the flange (Table 3.1). In the Appendix to this chapter are calculations that indicate that the measured fields inside the vacuum vessel are reasonable.

3.2.2.2 Finding the $m = 1$ spectral component

By using a solution to Laplace's equation for the vacuum magnetic field (Ref. 1) and choosing only the $m = 1$ Fourier term, it is possible to find the fraction of the input field which will have a (1,6) helicity (ignoring the toroidal spectral impurities). The fraction of power in the applied radial field with $m = 1$ is given by

$$f_{m=1,n=6} = \left| \frac{2}{\pi} \sin\left(\frac{d}{2a}\right) \frac{I_1\left(\frac{6r}{R}\right)}{I_1\left(\frac{6a}{R}\right)} \right|^2, \quad (3.4)$$

where toroidicity has been ignored. For direct comparison with measurements, eq. 3.4 will be evaluated at 50.07 cm, the outermost measurement location within the vacuum vessel. The result

is $f_{m=1,n=6} = 5.53 \times 10^{-5}$. Using the measured value for B_r/I_{applied} at 50.7 cm, 0.0117 G/A, the $m=1$ component of the field of $[(0.0117)^2 \times (5.53 \times 10^{-5})]^{1/2}$ G/A = 8.7×10^{-5} G/A. This number will be used henceforth to estimate the (1,6) radial magnetic field perturbation from the $n = 6$ coils, given the measured applied current.

3.2.3 Further diagnostics

The Ion Dynamics Spectrometer has been used to provide flow data for this work. A cursory description of its operation will be provided, and for detailed descriptions of its operation, see Refs. 5 and 8. Figure 3.17 is a sketch of the configuration that was normally used for this work.

By using two opposing views, there is no need for an absolute calibration of the spectrometer. The spectrometer is tuned using the filter monochromators and diffraction grating to observe a particular emission line from an impurity. Most frequently, this is a C^{4+} 227.09 nm line

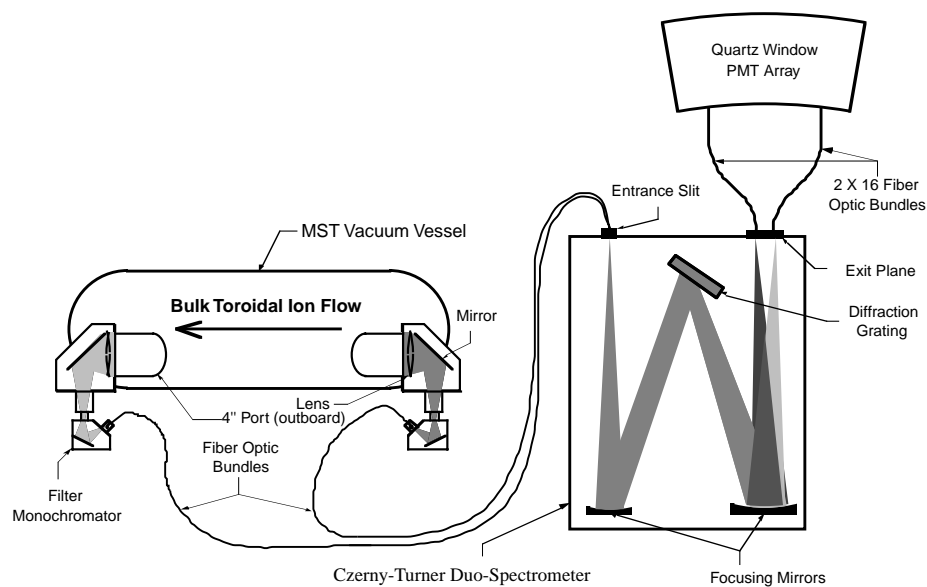


Figure 3.17. The Ion Dynamics Spectrometer, showing collection optics and the spectrometer itself.

for measurements near the core. Whatever the line, the flow velocity is found by finding the Doppler shift of the emission.

There are a couple of caveats with the measurement. The measurement is not local, but is integrated over a long line of sight in the plasma. In addition, the diagnostic samples over a wide minor radial cross-section of the plasma. Furthermore, the measurement is sensitive to the radial profile of the impurity state being examined. Thus, discharge-to-discharge variations in the radial profile of the impurity state of interest, e.g. due to changes in the plasma temperature, can result in different minor radial weightings for the measurement. For the purposes of this dissertation, however, these shortcomings are not crucial.

3.3 Ensemble Averaging

In order to extract useful information from the magnetic fluctuation data, it is frequently useful to do averaging. In addition to the obvious benefit of reducing noise, measurements involving correlations of multiple fluctuating quantities require ensemble averaging in order to approximate a surface average.

Several averaging techniques have been used for this work. In order to show slow trend behavior by averaging out the fast time behavior of sawtooth crashes, the simplest procedure is to average multiple discharges together, which works insofar as sawtooth crashes do not occur at exactly the same time in different discharges.

More often, what is wanted is an ensemble average of multiple realizations with the same plasma parameters in many discharges. In order to ensure that the realizations are taken in plasma conditions that are as identical as possible, it is useful to use sawtooth crashes as the time reference, i.e. to let zero time be given by some characteristic event in a sawtooth crash. A

“standard” package of routines that was developed for this purpose was employed.⁵ It uses the peak in the induced voltage at the toroidal gap during the sawtooth crash as the event that marks zero time.

What was done in running the code was to select sawteeth from discharges manually, in order to remove crashes that were too closely spaced compared with the normal sawtooth period in the discharge, and also to exclude sawteeth where the $m = 1$ modes were permanently locked. Typically, several sawteeth in a discharge were picked out in this way. In addition, for large enough ensembles, (about 100 sawteeth) cuts were made based on equilibrium plasma parameters around the time of the sawtooth crash, such as the electron density, plasma current, field reversal parameter, etc. The average was performed on the post-cut ensemble. As long as the time window being examined did not overlap multiple sawtooth crashes, the result was a reliable ensemble average of the parameters of interest.

In addition, discharges where permanent locking occurred during a sawtooth crash were investigated. The same procedure was performed as detailed previously, but there was only one locking event in a discharge, rather than several. By doing this, it is possible to compare sawteeth at the same plasma parameters with and without permanent locking of the $m = 1$ modes (Chapter 5).

Appendix

The large falloff of the magnetic field between the flange and the gap was surprising, so a couple of sanity checks were performed. These were a comparison to an analytic theory, and a simple calculation of the inductance of the gap.

To compare the attenuation with an analytic calculation, however, requires knowledge of the field right where the gap and vacuum vessel intersect. This will be done in the following section.

Theory and modeling.

Using analytic models with the experimental data as a constraint, the vacuum eigenfunction of the radial field put out by the $n=6$ coils has been constructed. By doing this, it is possible to find the field right at the toroidal gap, and thereby compare with theory the observed falloff from the flange to inside the vacuum vessel.

Fitting the data

The base theory (from Ref. 1) is analytic but is cylindrical. Nevertheless, reasonably good agreement with the experimental data is obtained. The $n = 6$ component of B_r from the toroidal gap on the midplane is given by:

$$B_{r,n=6} = B_{r0} \left[\frac{d}{2\pi a} \frac{I_0' \left(\frac{6r}{R} \right)}{I_0' \left(\frac{6a}{R} \right)} + \frac{2}{\pi} \sum_{m=1}^{\infty} \sin \left(\frac{md}{2a} \right) \frac{I_m' \left(\frac{6r}{R} \right)}{I_m' \left(\frac{6a}{R} \right)} \frac{1}{m} \right], \quad (3.A.1)$$

where B_{r0} is the radial field at the gap midplane, $d = 1.27$ cm is the gap width, $a = 52$ cm is the minor radius of the vessel wall, $R = 150$ cm is the vessel major radius, m refers to poloidal mode number, I_m is the modified Bessel function of order m , and ' refers to derivative with respect to argument.

In Fig. 3.A.1, eqn. 3.A.1 and various modified versions of it are fit to the experimental data. Fig. 3.A.1(b) shows the same fits over the whole minor radius. The fit is performed such that the fit value at the radial location of the second probe coil matches the field measured by that coil. The second coil was chosen rather than the one closest to the wall because the theory

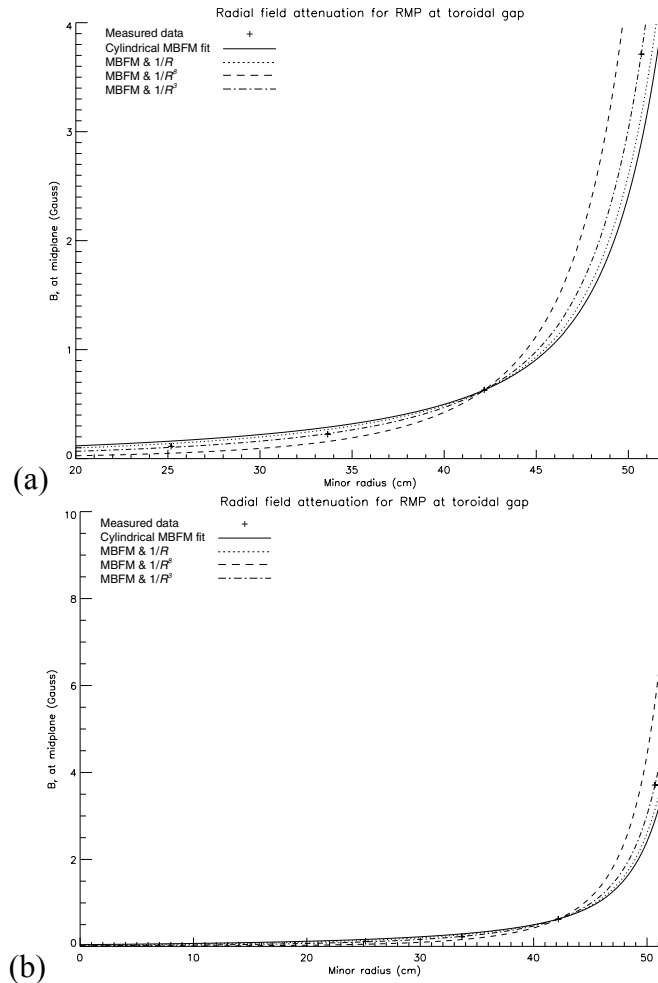


Figure 3.A.1. Profile of the radial magnetic field from perturbation at the toroidal gap with fits to a modified Bessel Function model (MBFM) and further modifications (a) 20 cm from the toroidal axis to the wall (b) over the entire minor radius.

assumes that the gap is straight, rather than flaring out poloidally as does the real gap. The flaring would probably depress the field seen at the first coil more than for coils farther out.

The solid curve in Fig. 3.A.1 is produced by fitting eq. 3.A.1 to the measured data points. The agreement with the data points is better for those inside the normalization point than for the outermost one. The dotted line in Fig. 3.A.1 shows a fit to a modification of eq. 3.A.1, where an

additional $1/R$ falloff has been introduced, as might be expected from toroidicity. The agreement with the data is better than for the purely cylindrical theory.

The dashed line in Fig. 3.A.1 is a fit to a further modification of eq. 3.A.1, in which an additional $1/R^7$ falloff is introduced to emulate continuing effects of the toroidal flange, i.e. a $1/R^{n+1}$ falloff. The agreement with the data is not as good as for the $1/R$ modification.

A further modification was made to eq. 3.A.1, in which the power of R was also varied to find the integer power that gave the best fit to the data. The result was that a $1/R^3$ falloff gave the best agreement with the measurement. The result is shown as the dash-dot curve in Fig. 3.A.1. The effects which account for the agreement may include toroidicity and the actual vs. ideal geometry of the gap.

Using this fit, the field/applied current at the toroidal gap is 0.0186 Gauss/A. Compared with the value at the coil major radius as measured with the flux loop, 0.0375 Gauss/A, the field has fallen by about a factor of 2. The expectation, based on a $1/R^7$ falloff within the flange, is to have a falloff of 1.6, so the fit gives results which are roughly consistent with expectations. By doing a simple two-point logarithmic fit to get a power law, the exponent is about 9.94, which would give a $1/R^{10}$ falloff. However, since there are only two points, no great significance should be attached to such a fit.

One experimental reality, which could account for the large falloff between the measured field in the toroidal flange and the analytic theory, is the fact that the gap has a narrower “neck” to form the vacuum sealing surface. This narrowed region might be expected to admit less flux than the rest of the gap.

Inductance calculation.

In addition, the coils themselves have a finite leakage inductance. An estimate using a back of the envelope calculation will be provided.⁹ The measured terminal inductance of one of the $n=6$ coils is 4.4 μH . This should provide a means to estimate the ratio of the radial field to the applied current at the coil, to be compared with the measurements. The terminal inductance includes a significant contribution of self-inductance or leakage inductance from the finite wire size, so it will be necessary to calculate this first.

The leakage flux per unit length between the wire and the MST shell will first be estimated by using an image current technique and assuming the shell is infinite in extent and perfectly conducting. The effects of image currents where the wire is “stitched” through the toroidal flange will be ignored because there will be little leakage in these portions due to the close fit of the holes.

The leakage flux per length is given by

$$\begin{aligned}
 B(r)_{\text{outside}} &= \frac{\mu_0 I}{2\pi} \left[\frac{r}{a^2} + \frac{1}{2a-r} \right] \\
 \Rightarrow \frac{\Phi}{l} \Big|_{\text{outside}} &= \frac{\mu_0 I}{2\pi} \int_0^a dr \left(\frac{r}{a^2} + \frac{1}{2a-r} \right) = \frac{\mu_0 I}{2\pi} \left(\frac{1}{2} + \ln 2 \right),
 \end{aligned} \tag{3.A.2}$$

on the top or bottom of the tank, and

$$\begin{aligned}
 B(r)_{\text{flange}} &= \frac{\mu_0 I}{2\pi} \left[\frac{r}{a^2} \right] \\
 \Rightarrow \frac{\Phi}{l} \Big|_{\text{flange}} &= \frac{\mu_0 I}{2\pi} \int_0^a dr \frac{r}{a^2} = \frac{\mu_0 I}{4\pi},
 \end{aligned} \tag{3.A.3}$$

in the flange, where a is the radius of the wire, B is the radial magnetic field, and $r \leq a$. Then the leakage inductance per unit length is

$$\frac{L}{l}\bigg|_{outside} = \frac{\Phi}{I}\bigg|_{outside} = \frac{\mu_0}{2\pi} \left(\frac{1}{2} + \ln 2 \right) = 0.24 \mu\text{H/m}, \quad (3.A.4)$$

above and below the flange, from eq. 3.A.2, and

$$\frac{L}{l}\bigg|_{flange} = \frac{\Phi}{I}\bigg|_{flange} = \frac{\mu_0}{4\pi} = 0.10 \mu\text{H/m}, \quad (3.A.5)$$

in the flange, from eq. 3.A.3. The length of one of the $n = 6$ coils is given by the sum of

$$l_{tb} = 2 \times 2 \pi R_{coil}, \quad (3.A.6)$$

which is the amount of wire on top and bottom of flange, including backwinding (the extra factor of 2). $R_{coil} = 0.915$ m, and

$$l_{flange} = 2 \times (2n - 1) \times h, \quad (3.A.7)$$

where $h = 0.15$ m is the thickness of the flange, the factor of 11 is the number of crossings, and the 2 is due to the backwinding. The leakage inductance is then

$$\begin{aligned} L_{leak} &= l_{tb} \times \frac{L}{l}\bigg|_{outside} + l_{flange} \times \frac{L}{l}\bigg|_{inside} \\ &= 2 \times 2 \pi R_{coil} \times 0.24 \mu\text{H/m} + 2 \times (2n - 1) \times h \times 0.10 \mu\text{H/m} \\ &= (2.87 + 0.33) \mu\text{H} = 3.2 \mu\text{H}. \end{aligned} \quad (3.A.8)$$

Therefore, the inductance of the gap itself is

$$L_{gap} = L_{terminal} - L_{leak} = (4.4 - 3.2) \mu\text{H} = 1.2 \mu\text{H}. \quad (3.A.9)$$

To first order, the gap flux is estimated to be $B 2 \pi R_{coil} d$, where $d = 1.27 \times 10^{-2}$ m is the gap width. The radial flux is in and out, but in phase with the coil, obviously. The mutual coupling of each half-wavelength loop to other loops should be small, but does increase the flux per ampere. Then

$$\Phi = B 2 \pi R_{coil} d = L_{gap} I, \quad (3.A.10)$$

where Φ is the flux. Thus from solving (3.14) for the ratio of current to (radial) magnetic field, $B/I = 1.2 \mu\text{H}/(2 \pi R_{coil} d) \approx 0.14 \text{ G/A}$. This is close to the measured value of the normalized radial field near one of the conductors of the coil, 0.12-0.15 G/A (Table 3.1). The conclusion, therefore, is that the estimate agrees with the measurement. Another possible diluting factor is the fact that joint of the vacuum vessel and toroidal flange is curved, rather than straight. This would result in an edge field that is reduced from the theoretical value, but further into the vacuum vessel there would be less difference. In summary, then, the measured ratio of radial field to applied current, although small within the vacuum vessel, is consistent with what should be expected, given the inductances.

References:

- ¹ R.N. Dexter, D.W. Kerst, T.W. Lovell, S.C. Prager, and J.C. Sprott, PLP 965, Plasma Studies, University of Wisconsin (1985).
- ² S. Assadi, Ph. D. Thesis, University of Wisconsin—Madison (1988).
- ³ Figure courtesy of N. Lanier, present address LANL (1999).
- ⁴ A. F. Almagri, Ph. D. Thesis, University of Wisconsin—Madison (1990).
- ⁵ J. T. Chapman, Ph. D. Thesis, University of Wisconsin—Madison (1998).
- ⁶ A. F. Almagri, University of Wisconsin, private communication (1999).
- ⁷ M. R. Stoneking, Lawrence University, private communication (1999).
- ⁸ D. J. Den Hartog and R. J. Fonck, Rev. Sci. Instrum. **65**, 3238 (1994).
- ⁹ J. S. Sarff, University of Wisconsin, private communication (1999).

4 Experiments involving external torques

The experimental results will be divided by the dominant electromagnetic torque physics. This chapter will focus on experimental results involving external torques imposed by applied magnetic perturbations. These experiments will be further divided into experiments involving static magnetic perturbations and attempts to produce an effect on the plasma through a rotating magnetic perturbation. The final section is a brief discussion of the variation of the external torque over a sawtooth cycle, due to the changing $m = 1$ field error and mode amplitudes.

The static perturbation experiments will be discussed in § 4.1. In § 4.1.1 the results of the experiments that were done using applied perturbations at the poloidal gap will be discussed. These perturbations, if resonant, interact with multiple modes. Discussion of the background field errors at the poloidal gap will be presented in § 4.1.1. The results for an $m = 1$ perturbation on the $m = 1$ modes are discussed in § 4.1.1.2. Effects of an $m = 0$ perturbation to the $m = 1$ modes are discussed in § 4.1.1.3. Results of an $m = 0$ perturbation applied to discharges where the $m = 0$ modes are rotated using an applied edge bias are detailed in § 4.1.1.4. The effects of an $m = 1$ perturbation on similar discharges are discussed in § 4.1.1.5. Results for an $m = 2$ perturbation are discussed in § 4.1.1.6.

A complementary experiment was performed in which an $n = 6$ perturbation was applied at the toroidal gap, which should only exert an external torque on the (1,6) mode. In § 4.1.2 results of the experiment will be discussed. In § 4.1.3 there is a quantitative comparison between the poloidal gap experiment and toroidal gap experiment. Finally, parameters relevant for the viscous torque will be estimated in § 4.1.4 using the torque balance at the locking threshold.

The remainder of the chapter will be organized as follows: § 4.2 will be devoted to the results of the rotating magnetic perturbation at the toroidal gap, and § 4.3 will discuss external torques between field errors and the modes during the sawtooth cycle.

4.1 Static perturbation experiments.

4.1.1 Poloidal gap

In these experiments, magnetic perturbations with $m = 0, 1,$ or 2 were applied at the poloidal gap, sometimes using the correction coils (§ 3.1.1.1). Because the gap is narrow compared with the major circumference of MST (1 cm vs. 10 m), the perturbations are broadband in toroidal mode number. The results are consistent with resonant torque theory: the $m = 1$ modes were locked by the resonant ($m = 1$) perturbation, and they were not locked by those which were not resonant with them ($m = 0, 2$). Similarly, the $m = 0$ modes were locked by an $m = 0$ perturbation, but unaffected by other mode numbers. Many of the results of these experiments were previously published in Ref. 1.

4.1.1.1 Background field errors and mode rotation.

There are field errors at the poloidal cut in MST even in the absence of applied perturbations, as can be seen in Figs. 4.1 and 4.2. Figure 4.1 represents the case where the correction coils were disengaged to provide the magnetic perturbations (§§ 4.1.1.2-3, and 4.1.1.6). Figs. 4.1(a)-(c) show the $m = 0, 1,$ and 2 components of the radial field at the poloidal cut. These may be taken to be the background upon which additional magnetic perturbations are added. The monotonic increase which can be seen in the $m = 2$ component of the field error at the poloidal cut [Fig. 4.1(c)] is generated by the magnetic field soaking through the conducting shell around the (square) poloidal field transformer. Figs 4.1(d) and 4.1(e) show the toroidal phase velocity of the (1,6) mode and the amplitude of the poloidal fluctuation at the wall (not the total amplitude),

respectively. The $m=1$ component of the field error is sufficiently small that the $m = 1$ modes are not locked, but are able to rotate freely. The other components of the field error are not resonant with the $m = 1$ modes, so they should not affect the $m = 1$ mode rotation. Figure 4.2 depicts the same quantities for a discharge where the correction coils were employed in their standard fashion. The field errors in this case may be regarded as backgrounds for the experiments in §§

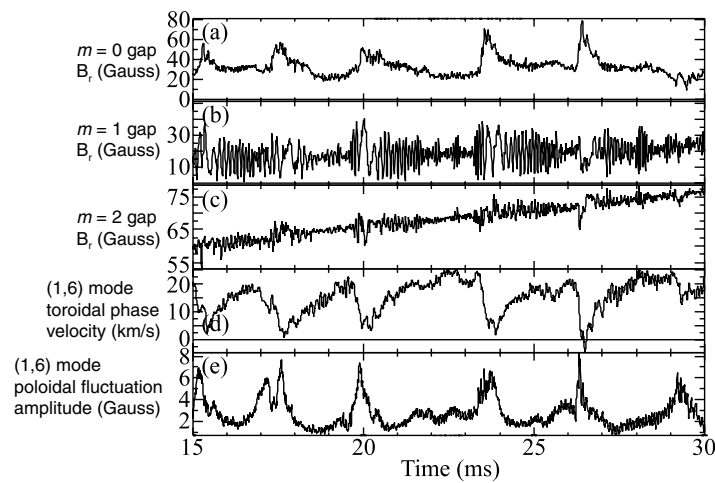


Figure 4.1. (a) $m = 0$, (b) $m = 1$, and (c) $m = 2$ components of the field error at the poloidal gap; (1,6) mode (d) toroidal phase velocity and (e) poloidal field fluctuation, for a discharge with no pulsed magnetic perturbation, with correction coils disengaged.

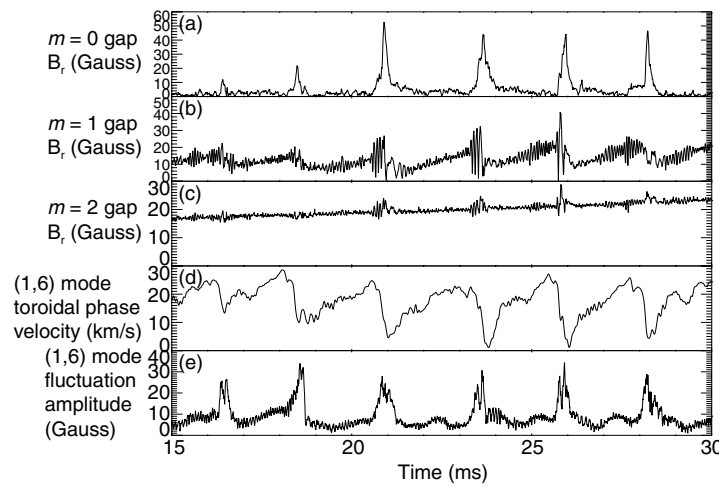


Figure 4.2. (a) $m = 0$, (b) $m = 1$, and (c) $m = 2$ components of the field error at the poloidal gap; (1,6) mode (d) toroidal phase velocity and (e) poloidal field fluctuation, for a discharge with no pulsed magnetic perturbation, with correction coils engaged.

4.1.1.4-5. The rapid changes in the (1,6) mode velocity seen in Figs. 4.1(d) and 4.2(d) are due to sawtooth crashes, which are evidenced as well in the spikes in the mode amplitude [Figs. 4.1(e) and 4.2(e)]

4.1.1.2 Effect of $m = 1$ perturbation on $m = 1$ modes (resonant)

When an $m = 1$ magnetic perturbation of sufficient amplitude is applied, the $m = 1$ modes lock. An example is shown in Fig. 4.3. Figure 4.3(b), the $m=1$ component of the radial magnetic field at the cut, shows the pulsed magnetic perturbation as a large rise from the background level beginning at 20 ms. The spectral purity of the pulse is evidenced by Figs. 4.3(a) and (c), which show that the $m = 0$ and $m = 2$ components of the radial field have no response (cf. Fig. 4.1). Locking occurs at ~ 22 ms into the discharge, as defined by the velocity of the (1,6) mode [Fig. 4.3(d)], which slows to zero and remains stationary thereafter. Locking of the (1,6) mode occurs between sawtooth crashes seen as spikes in the $n = 6$ poloidal field fluctuation at the wall [Fig.

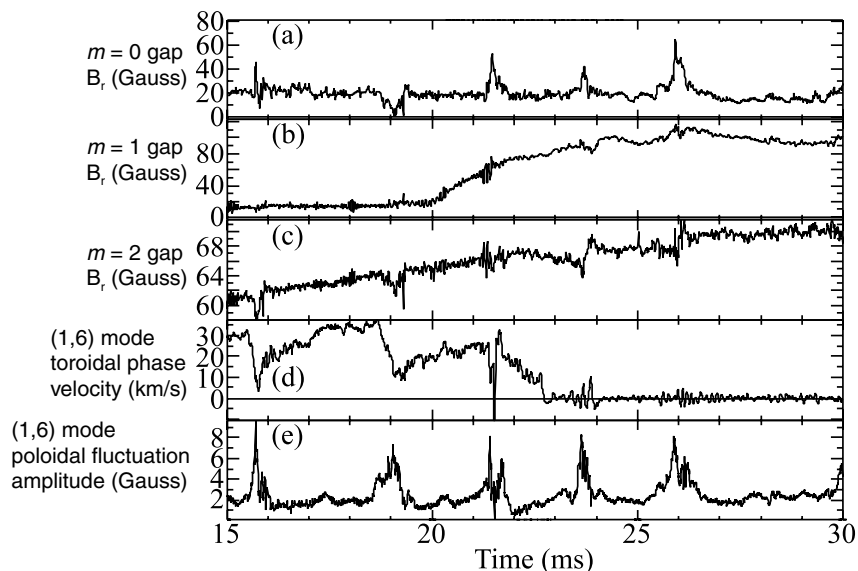


Figure 4.3. (a) $m = 0$, (b) $m = 1$, and (c) $m = 2$ components of the field error at the poloidal gap; (d) (1,6) mode toroidal phase velocity and (e) poloidal field fluctuation, for a discharge with pulsed $m = 1$ magnetic perturbation at the poloidal gap [evident in (b)].

4.3(e)]. Locking occurs when the $m=1$ component of the radial field at the poloidal cut is about 80 Gauss, or $\sim 8\%$ of the average poloidal field at the wall. Figure 4.4 shows that the baseline ($m = 1, n = 6, 7, 8$) mode amplitudes increase after locking [Fig. 4.4(a)-(c), also cf. Fig. 4.3]. In addition, all three modes exhibit similar kinematic responses to the perturbation [Fig. 4.4(d)-(f)].

4.1.1.3 Effect of $m = 0$ perturbation on $m = 1$ modes (nonresonant)

An applied $m = 0$ magnetic perturbation produces no obvious effect on the (1,6) mode, as can be seen in Fig. 4.5. This is as expected for a perturbation which is not resonant with the $m=1$ modes. In this case the amplitude of the $m = 0$ component of the radial magnetic field at the poloidal cut at a sawtooth crash can reach 90 Gauss—comparable to the $m = 1$ error needed to induce locking. The reduction in the $m = 2$ field error amplitude [Fig. 4.5(c)] is due to the fact that this perturbation also had a significant $m = 2$ component.

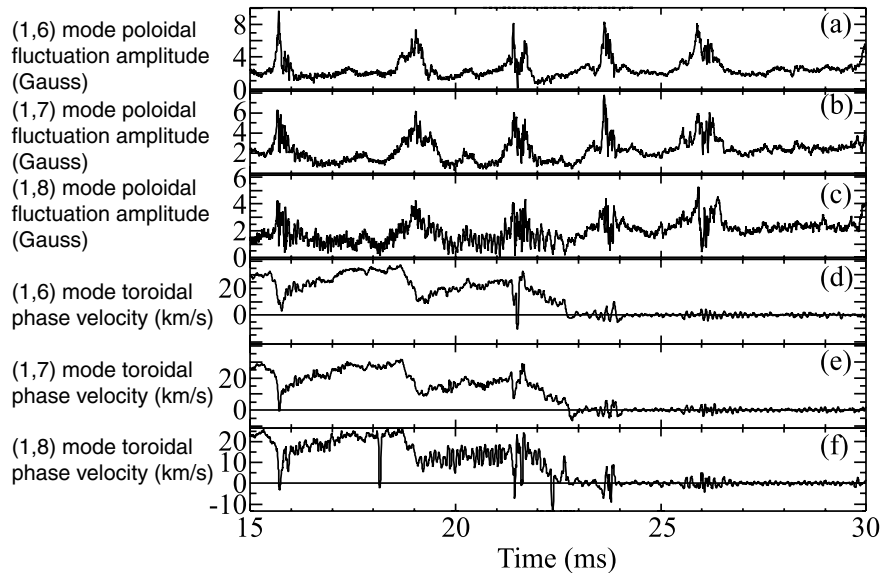


Figure 4.4. (a) $m = 1, n = 6$, (b) $m = 1, n = 7$, and (c) $m = 1, n = 8$ mode amplitude. (d) $m = 1, n = 6$, (e) $m = 1, n = 7$, and (f) $m = 1, n = 8$ mode toroidal phase velocity for a discharge with pulsed $m = 1$ magnetic perturbation at the poloidal gap.

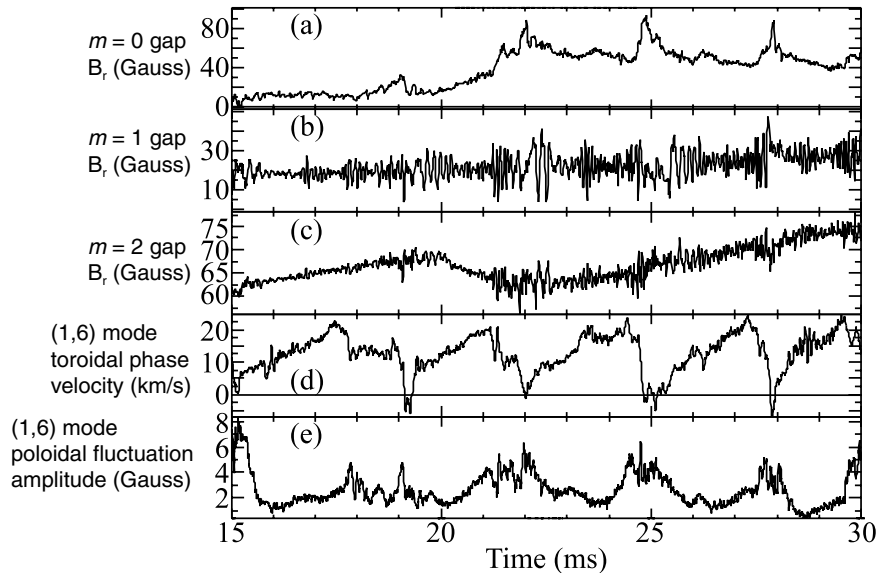


Figure 4.5. (a) $m = 0$, (b) $m = 1$, and (c) $m = 2$ components of the field error at the poloidal gap; (d) (1,6) mode toroidal phase velocity and (e) poloidal field fluctuation, for a discharge with pulsed $m = 0$ magnetic perturbation at the poloidal gap [evident in (a)].

There were no toroidal magnetic field pickup coils of the toroidal array present during this experiment, so the phase velocity of the (0,1) mode couldn't be determined (cf. § 3.2.1.2). The following experiment was performed to rectify this deficiency.

4.1.1.4 Effects of $m = 0$ perturbation on $m = 0$ modes (resonant)

In addition to applying an $m = 0$ perturbation at the poloidal gap, a probe was inserted into the plasma and biased with respect to the shell in order to apply an electric field to the edge and thereby produce rotation of the (0,1) mode (cf. Refs. 2-4). The results of this experiment are summarized in Fig. 4.6. All quantities are averaged over about 10 discharges. The period in which the electric field was applied is marked by the gray rectangle in Fig. 4.6.

In Fig. 4.6(a)-(c), the dashed line represents a signal in discharges where the $m = 0$ perturbation was not pulsed, while the solid line is the signal in discharges with the $m = 0$ perturbation. Figure 4.6(a) is the $m = 0$ field error at the poloidal gap. The pulsed perturbation is about

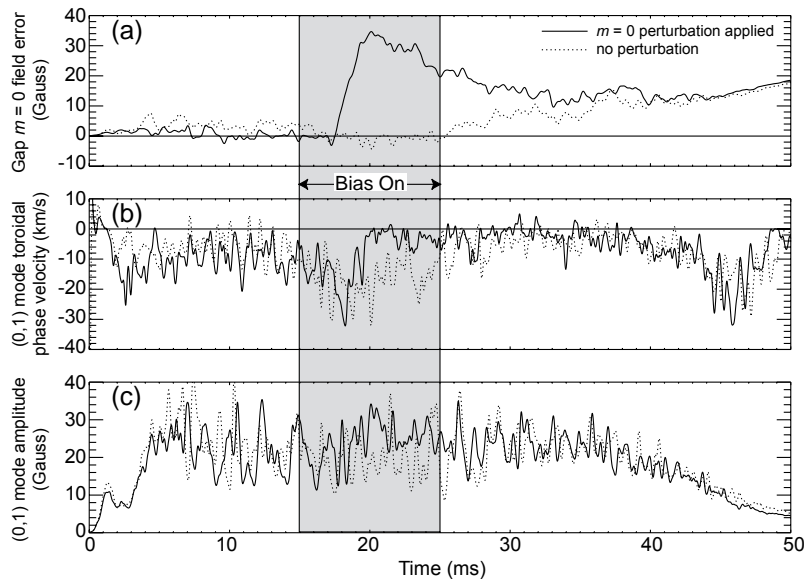


Figure 4.6. (a) $m = 0$ field error/perturbation, (b) $(0,1)$ mode toroidal phase velocity, and (c) $(0,1)$ mode amplitudes, for ensembles of discharges with applied electric field with (solid) and without (dotted) $m = 0$ perturbation. The gray area marks the period of applied edge electric field.

30 Gauss, which is lower than what was applied in § 4.1.1.2, but proved sufficient for results to be seen. The $(0,1)$ mode phase velocity is shown in Fig. 4.6(b). Although the signals are noisy, it should be clear that this mode is rotating at about 10 km/sec on average during the interval in which the bias is applied. At about 20 ms the $(0,1)$ mode velocity goes to zero when the $m = 0$ perturbation is employed, whereas there is continued rotation of the $(0,1)$ mode during the whole period of applied bias. Figure 4.6(c) is the $(0,1)$ mode amplitude. It looks to be somewhat higher when it locks to the applied perturbation than the case with no applied perturbation.

4.1.1.5 Effects of applied $m = 1$ perturbation on $m = 0$ modes (nonresonant).

An experiment with a similar setup to that in the previous section was performed that used an $m = 1$ perturbation. The topic of interest is to look at the effect on the $m = 0$ modes. The results of this experiment are summarized in Fig. 4.7. All quantities are averaged over about 10 discharges. The period in which the electric field was applied is marked by the gray rectangle in

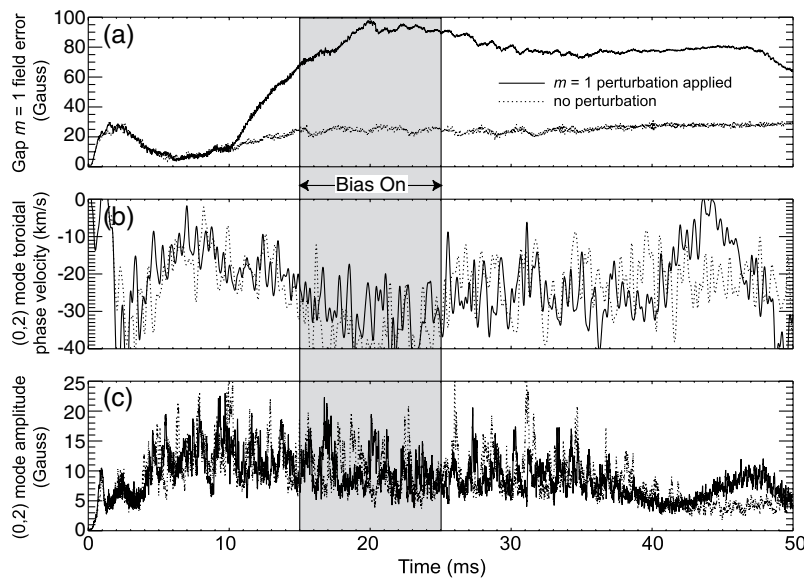
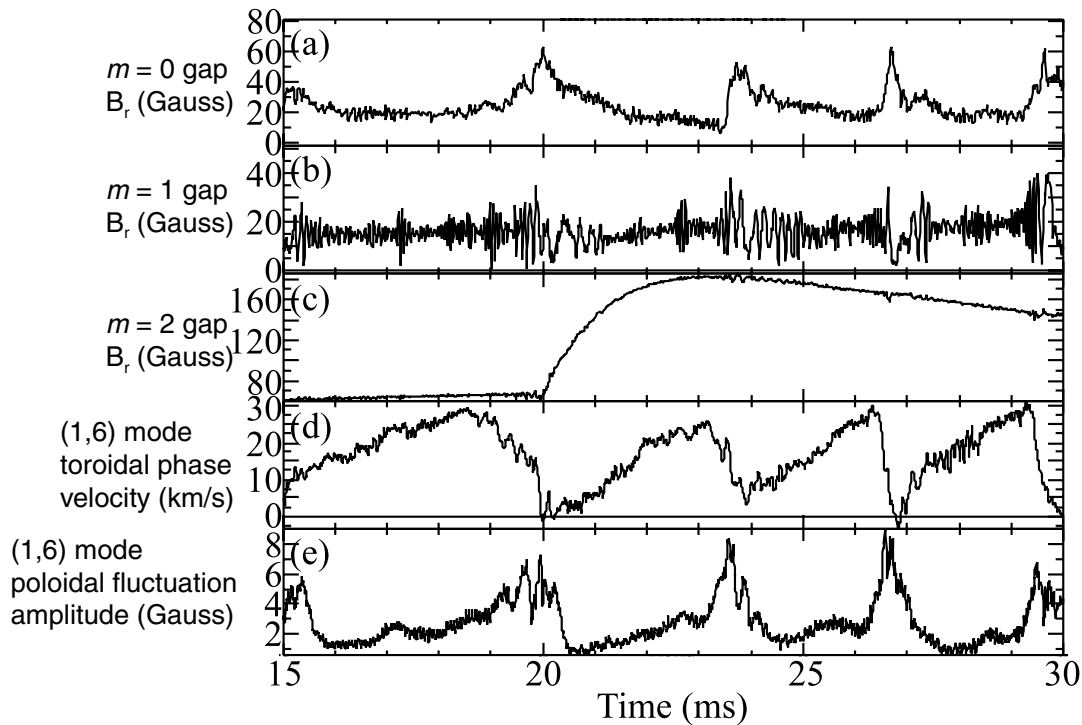


Figure 4.7. (a) $m = 1$ field error/perturbation, (b) (0,2) mode toroidal phase velocity, and (c) (0,2) mode amplitudes, for ensembles of discharges with applied electric field with (solid) and without (dotted) $m = 1$ perturbation. The gray area marks the period of applied edge electric field.

Fig. 4.7. The dotted line denotes discharges with no applied perturbation. Figure 4.7(a) is the $m = 1$ component of the field error at the poloidal gap. For the discharges with applied electric field, the $m = 1$ perturbation was sufficient to lock the $m = 1$ modes. Figures 4.7(b) and (c) are the toroidal phase velocity of the (0,2) mode [better phase resolution than (0,1)] and its amplitude. No significant difference is evident between the two cases, so the obvious conclusion is that there is no direct effect produced on the $m = 0$ modes by the $m = 1$ perturbation.

4.1.1.6 Effects of applying an $m = 2$ perturbation (nonresonant)

As expected, an applied $m = 2$ magnetic perturbation produces no effect on the (1,6) mode rotation, as can be seen in Fig. 4.8. This holds although the $m = 2$ amplitude of the radial magnetic field at the poloidal cut [Fig. 4.8(c)] reaches 190 G (about 20 % of the average poloidal field at the wall), i.e. more than twice the amplitude for which locking occurred with an $m = 1$ perturbation.



In addition, an $m = 2$ perturbation appears not to have an effect on the $(0,1)$ mode rotation, which is once again facilitated by the use of biased probes. Figure 4.9(a) depicts the $m = 2$ component of the field error at the poloidal gap. Figure 4.9(b) depicts the $(0,2)$ mode velocity averaged over the available discharges with bias and applied $m = 2$ perturbation (solid) and a reference set without applied perturbation (dotted). There is no obvious effect on the $(0,1)$ rotation. One caveat is that the perturbation amplitude is smaller in this case than in Fig. 4.8.

An obvious question is whether an $m = 2$ perturbation will lock a preexisting $m = 2$ mode. As argued in § 2.3.3, however, the $m = 2$ fluctuation in MST (averaged over all n) is about an order of magnitude smaller than the $m = 1$. Moreover, the $m = 2$ fluctuation is dominantly generated by toroidicity, so the kinematics that can be observed in the $m = 2$ fluctuations are those of the $m = 1$ modes, even in the presence of the large $m = 2$ perturbation. The $m = 2$ perturbation may therefore be regarded as nonresonant.

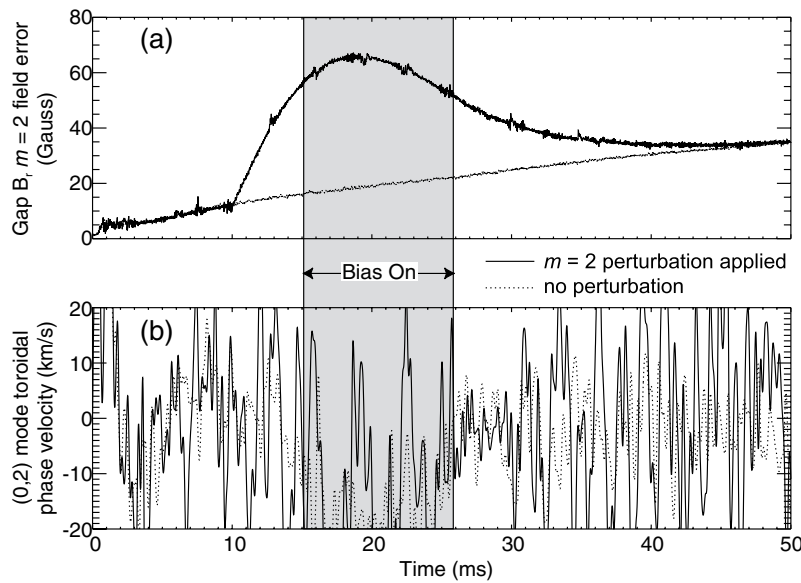


Figure 4.9. (a) $m = 2$ field error at the poloidal gap and (b) toroidal phase velocity of the (0,2) mode for ensembles of discharges with applied electric field (gray) with (solid, 2 discharges) and without (dotted, ~ 10 discharges) applied $m = 2$ perturbation.

4.1.2 Toroidal gap

As a complement to the experiments in § 4.1.1, a pulsed perturbation with $n = 6$ was applied at the toroidal gap using the $n = 6$ coils (§ 3.1.1.2). The gap width is narrow with respect to the minor circumference (1 cm vs. ~ 3 m), so the perturbation is broadband in poloidal mode number. The calibration performed in § 3.2.2 to estimate the perturbation amplitude from the measured current in the coil will be used, but neglecting soak-in effects from the longer timescale of the static perturbation compared to the rotating perturbation (1 ms vs. 100 μ s). The calibration factor is 8.7×10^{-5} Gauss for the (1,6) perturbation per applied Ampere of current in the coil (§ 3.2.2.2). This ignores screening by the plasma.

At the level of perturbation that could be applied, there were two major outcomes. One was that the $m = 1$ modes locked within ~ 2 ms after the perturbation was applied (Fig. 4.10). The other was that the (1,6) mode sometimes exhibits episodic deceleration for several millise-

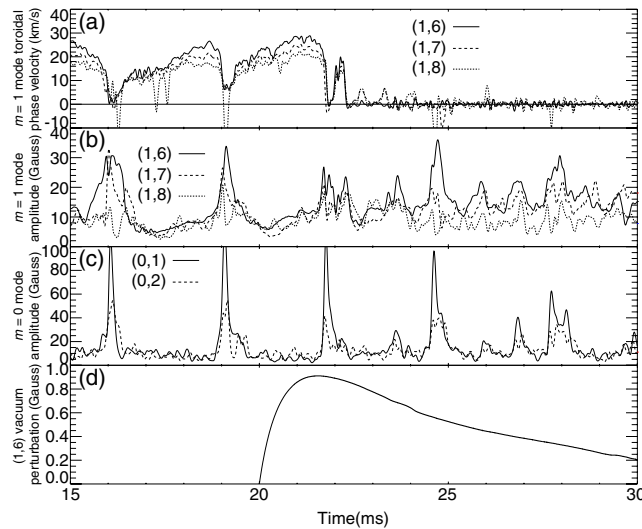


Figure 4.10. Discharge with applied $n = 6$ perturbation. (a) ($m = 1, n = 6, 7, 8$) mode toroidal phase velocities, (b) ($m = 1, n = 6, 7, 8$) mode amplitudes, (c) ($m = 0, n = 1, 2$) mode amplitudes, and (d) (1,6) perturbation vacuum amplitude. This discharge exhibits prompt locking of the $m = 1$ modes.

onds while the other $m = 1$ modes continue rotating (Fig. 4.11), followed eventually by locking of all of the $m = 1$ modes.

In Fig. 4.10(a), the phase velocities of the (1,6), (1,7) and (1,8) modes are plotted. All three modes lock (i.e. achieve zero phase velocity) at the same time in response to the applied perturbation, plotted in Fig. 4.10(d). In Fig. 4.10(b) are plotted the ($m = 1, n = 6, 7, 8$) mode amplitudes. The increase in the baseline value of these amplitudes, which is seen after 23 ms, is a characteristic feature of discharges where the $m = 1$ modes lock [cf. Fig. 4.4(a-c) and Ref. 5], presumably due to the effects of resonant field errors/perturbations. In Fig. 4.10(c), the ($m = 0, n = 1, 2$) mode amplitudes are plotted. These modes do not exhibit any change in baseline amplitude.

The same quantities are plotted in Fig. 4.11 for a discharge where the (1,6) mode experienced sporadic decelerations. Figure 4.11(a) shows the bursts of deceleration between the

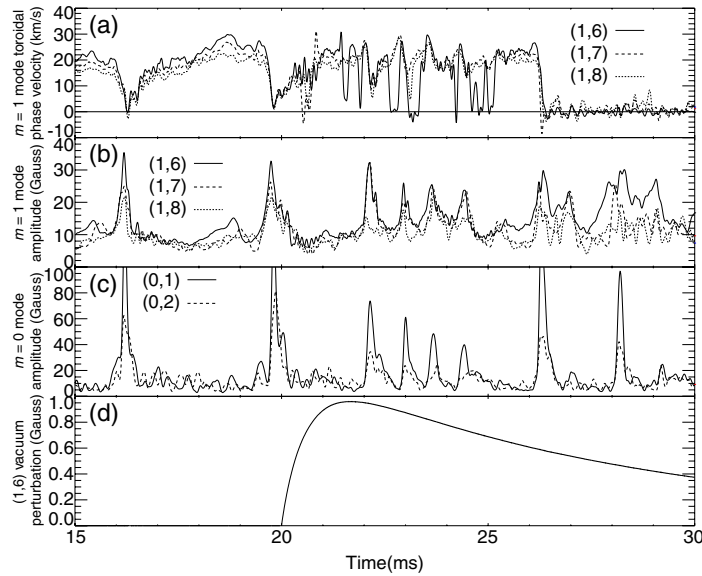


Figure 4.11. Discharge with applied $n = 6$ perturbation. (a) ($m = 1, n = 6, 7, 8$) mode toroidal phase velocities, (b) ($m = 1, n = 6, 7, 8$) mode amplitudes, (c) ($m = 0, n = 1, 2$) mode amplitudes, and (d) (1,6) perturbation vacuum amplitude. This discharge exhibits locking and unlocking of the (1,6) mode.

sawtooth crashes [spikes in Fig. 4.11(b) and (c)] in the (1,6) mode (around 23 and 25 ms). These are clearly absent in the (1,7) and (1,8) modes. Note that the baseline mode amplitudes and the perturbation amplitude are not vastly different between Figs. 4.10(b-d) and 4.11(b-d).

These results can be compared to results for the $m = 1$ perturbation applied at the poloidal gap. From the solution to for the vacuum field at the poloidal gap,⁶

$$f_{(1,6)}|_{pg} = \left(\frac{a}{R_0}\right)^2 f_{(1,6)}|_{tg}, \quad (4.1)$$

where $f_{(1,6)}$ is the (1,6) power fraction of the radial field perturbation, pg refers to the poloidal gap, tg refers to the toroidal gap, $a = 0.52$ m is the minor radius, and $R_0 = 1.5$ m is the major radius. Then the (1,6) component of the $m = 1$ perturbation at the poloidal gap is given by

$$b_{(1,6)}|_{pg} = \sqrt{f_{(1,6)}|_{pg} |b_{m=1}|_{pg}|^2} = \sqrt{\left(\frac{a}{R_0}\right) f_{(1,6)}|_{tg} |b_{m=1}|_{pg}|^2}. \quad (4.2)$$

From § 3.2.2.2, $f_{(1,6)}|_{tg} = 5.53 \times 10^{-5}$. Then

$$b_{(1,6)}|_{pg} = (5.53 \times 10^{-5})(0.52/1.5)(80 \text{ Gauss}) \approx 0.21 \text{ Gauss}. \quad (4.3)$$

Clearly, in Figs. 4.10(d) and 4.11(d), locking requires larger perturbation amplitudes, and for larger mode amplitudes as well (accounting for the conversion factor from poloidal field fluctuation to total fluctuation). This implies a larger torque (see § 4.1.3).

The sporadic decelerations and reaccelerations of the (1,6) mode that occur in Fig. 4.9 can be accounted for straightforwardly. The (1,6) mode is presumably locked by the perturbation, then is spun back up by viscous coupling to the other modes, particularly the (1,7) and (1,5), owing to the differential rotation. Ref. 7 is theoretical work along these lines. Nonlinear effects may also play a role; this possibility will be discussed in the next chapter.

That the $n = 6$ perturbation also affected the (1,7) and (1,8) modes was a surprising result. The coils, as discussed earlier, do not produce any significant $n = 7$ or $n = 8$ magnetic field. Therefore, they must be responding indirectly to the perturbation. As this is an effect beyond the resonant external electromagnetic torque it will be discussed in the next chapter.

4.1.3 Quantitative comparison of EM torques in single- m and single- n perturbations

To compare quantitatively the results of the experiments involving the $m = 1$ perturbation at the poloidal gap (§ 4.1.1.1) and the $n = 6$ perturbation at the toroidal gap (§ 4.1.2), it is necessary to calculate the external torque on the (1,6) mode. Fortunately, a full computation is not necessary to compare the results of the two experiments, because for any resonant external per-

turbation the current density perturbations and magnetic field perturbations are proportional, and the current profiles are most likely not too different (similar plasma parameters). The torque has the form

$$T_{ext} \sim b_{pert} b_{mode} \sin \delta \quad (4.4)$$

(cf. eqn. 2.3), where T_{ext} is the external electromagnetic torque on a mode, b_{pert} is the amplitude of the resonant perturbation at the mode's resonant surface, b_{mode} is the amplitude of the mode at its resonant surface, and δ is the phase between the mode and the perturbation. Thus, assuming $\sin \delta = 1$, i.e. the maximum possible torque, it suffices to compare the products of the amplitudes. Furthermore, by assuming that the amplitudes at the resonant surface are proportional to those at the wall, the comparison can be made using the measured/calculated values at the plasma edge.

For the $m = 1$ perturbation at the poloidal gap (§ 4.1.1.1), this quantity will be evaluated at the locking transition (just before 23 ms in Fig. 4.3). The measured poloidal field fluctuation amplitude of the (1,6) mode [Fig. 4.3(e)] must be multiplied by the conversion factor from equation 3.3 to generate the total amplitude:

$$|b_{(1,6)}^{mode}| = b_{(1,6),\theta}^{mode} \sqrt{1 + \left(\frac{6(.52)}{1.15}\right)^2} \approx 2.31 b_{(1,6),\theta}^{mode} \quad (4.5)$$

In addition, the $m = 1$ perturbation amplitude should be multiplied by the $n = 6$ fraction:

$$b_{(1,6)}^{pert} = \sqrt{f_{(1,6)}} |b_{m=1}^{pert}|^2 = \sqrt{6.64 \times 10^{-6}} b_{m=1}^{pert} = 2.58 \times 10^{-3} b_{m=1}^{pert} \quad (4.6)$$

Just before the occurrence of locking, $b_{pert,m=1} = 80$ Gauss, and $b_{mode,(1,6)}^\theta = 2.5$ Gauss, so the torque is:

$$T_{(1,6)} = C_{(1,6)} (2.31)(2.5 \text{ Gauss})(2.58 \times 10^{-3})(80 \text{ Gauss}) = 1.2 C_{(1,6)} \text{ Gauss}^2, \quad (4.7)$$

where $C_{(1,6)}$ is a constant of proportionality.

For the $n = 6$ perturbation at the toroidal gap, the product will be evaluated for the discharge in Fig. 4.11 at the (1,6) mode locking event at ~ 22.6 ms [Fig. 4.11(a)]. The full mode amplitude and (1,6) perturbation amplitude data are available, so the torque is

$$T_{(1,6)} = C_{(1,6)} (12 \text{ Gauss})(0.9 \text{ Gauss}) = 7.2 C_{(1,6)} \text{ Gauss}^2. \quad (4.8)$$

As long as the current profiles are not too different, so that the values can be directly compared (equal C). Then the torque at the locking threshold, i.e. just before the phase velocity makes the rapid transition to zero, is a factor of 6 larger for an $n = 6$ perturbation than for an $m = 1$ perturbation.

Internal electromagnetic torques (§ 2.2.1.2) can probably be excluded as a mechanism to explain the difference, because for both cases the evaluation is being done away from a sawtooth crash, so the mode amplitudes are smaller. Inertial effects are probably small as well, because the acceleration is small for both cases. The most likely explanation, then, is differences in the viscous torque. The $m = 1$ perturbation at the poloidal gap directly affects *all* of the $m = 1$ modes, so no differential rotation between the modes is set up. On the other hand, the $n = 6$ perturbation at the toroidal gap *only* couples directly to the (1,6) mode; the other $m = 1$ modes are unaffected, so they will continue their rotation, and drag on the (1,6) mode. It will break free of the other modes and lock when the electromagnetic torque on it is large enough or the inter-island viscosity is sufficiently reduced, e.g. by changes in the island widths.

Of further interest is the external torque from the $m = 0$ perturbation at the poloidal gap on the rotating (0,1) mode (from § 4.1.1.4). We will make the same assumptions as for the $m = 1$ perturbation acting on the (1,6) mode, but use the (0,1) amplitude fraction for an $m = 0$ perturba-

tion at the poloidal gap,⁶ 4.6×10^{-4} . Using this, and evaluating the perturbation amplitude and mode amplitude at 19 ms (Fig. 4.5) as 30 Gauss and 20 Gauss respectively, the torque is

$$T_{(0,1)} = C_{(0,1)}(30 \text{ Gauss})(20 \text{ Gauss})(4.6 \times 10^{-4}) = 0.28 C_{(0,1)} \text{ Gauss}^2. \quad (4.9)$$

If $C_{(0,1)} \sim C_{(1,6)}$, then $T_{(0,1)} < T_{(1,6)}$. An obvious explanation is that the (0,1) mode is nearer the edge, so the perturbation amplitude at its rational surface is larger than for the (1,6) mode. In addition, the viscous torque may well be different, especially given that the edge flow is being driven in this case.

4.1.4 Estimating the viscous torque

In the previous section viscous torques were invoked to explain the difference in the electromagnetic torques required for locking between the $m = 1$ perturbation at the poloidal gap and the $n = 6$ perturbation at the toroidal gap. Since the point where the EM torque was evaluated is at the locking transition in both cases, and the velocity of the (1,6) mode is essentially static, inertial effects should be unimportant. It is therefore needed only to balance the electromagnetic and viscous torques (cf. eqn. 2.2):

$$T_{em} + T_{vis} = 0. \quad (4.10)$$

To estimate the electromagnetic torque, the important quantity is the toroidal component of the Lorentz force density on the (m,n) mode due to a (spatially) resonant perturbation:

$$\begin{aligned} f_\phi &\equiv \hat{\mathbf{e}}_\phi \cdot \left(\mathbf{j}_{(m,n)}^{pert} \times \mathbf{b}_{(-m,-n)}^{mode} + \mathbf{j}_{(m,n)}^{mode} \times \mathbf{b}_{(-m,-n)}^{pert} \right) \\ &= \left(j_{(m,n),r}^{pert} b_{(-m,-n),\theta}^{mode} - j_{(m,n),\theta}^{pert} b_{(-m,-n),r}^{mode} + j_{(m,n),r}^{mode} b_{(-m,-n),\theta}^{pert} - j_{(m,n),\theta}^{mode} b_{(-m,-n),r}^{pert} \right), \end{aligned} \quad (4.11)$$

where the phase shift δ is due to the rotation of the mode with respect to the static perturbation. The dominant part of the mode's current density should be that within the flux surface, i.e. j_θ . In addition, near the resonant surface, the dominant component of the mode's magnetic field is b_r .

Furthermore, the magnetic perturbation is mainly radial, at least for an $m = 1$ mode. Then (4.10) reduces to

$$f_\phi = -\left(j_{(m,n)}^{pert} b_{(-m,-n)}^{mode} + j_{(m,n)}^{mode} b_{(-m,-n)}^{pert}\right) \sin \delta. \quad (4.12)$$

Also,

$$j_{(m,n),\theta}^{mode} = \frac{1}{\mu_0} \hat{\mathbf{e}}_\phi \cdot \nabla \times \mathbf{b}_{(m,n)}^{mode}. \quad (4.13)$$

Since the mode and perturbation amplitudes both are mostly radial, if a cylindrical approximation is used, the poloidal current is simply

$$j_{(m,n),\theta}^{mode/pert} = \frac{1}{\mu_0 R} \frac{\partial b_{(m,n),r}^{mode/pert}}{\partial \phi}. \quad (4.14)$$

If the ϕ dependence is sinusoidal, i.e. $b_r \sim e^{-in\phi}$, then

$$j_{(m,n),\theta}^{mode/pert} = \frac{-nb_{(m,n),r}^{mode/pert}}{\mu_0 R}, \text{ where the factor of } i \text{ has been removed.} \quad (4.15)$$

Therefore, the Lorentz force density is

$$f_\phi = \frac{2n}{\mu_0 R} b_{(m,n),r}^{mode} b_{(-m,-n),r}^{pert} \sin \delta. \quad (4.16)$$

The electromagnetic torque, therefore, is

$$T_{em} = \int d^3x R f_\phi = \frac{2n}{\mu_0} \int d^3x b_{(m,n),r}^{mode} b_{(-m,-n),r}^{pert} \sin \delta. \quad (4.17)$$

The amplitudes here are those at the resonant surface.

The viscous torque, as per eqn. 2.3, is

$$T_{vis} = \int d^3x \rho v_\perp R \frac{\partial(\Delta\Omega)}{\partial r}. \quad (4.18)$$

Equating the viscous and electromagnetic torques, the perpendicular viscosity (making the assumption that it's constant) can be solved for:

$$v_{\perp} = \frac{2n \int d^3x b_{(m,n),r}^{mode} b_{(-m,-n),r}^{pert} \sin \delta}{\mu_0 \int d^3x \rho R \frac{\partial(\Delta\Omega)}{\partial r}} = \frac{2n \int r^2 b_{(m,n),r}^{mode} b_{(-m,-n),r}^{pert} \sin \delta dr}{\mu_0 R \int r^2 \rho \frac{\partial(\Delta\Omega)}{\partial r} dr}, \quad (4.19)$$

where periodic cylindrical symmetry has been assumed to dispense with the angular integration.

For the case of an applied $m = 1$ perturbation at the poloidal gap, all of the $m = 1$ modes respond together, so a simplification will be to use averaged mode and perturbation amplitudes and n in the numerator, and the limits of integration should be from 0 to the reversal ($q = 0$) radius. Similarly, in the denominator, the same limits of integration should apply. Therefore eqn. 4.19 becomes

$$v_{\perp} = \left| \frac{2\bar{n} \int_0^{r_{q=0}} r^2 \bar{b}_{m=1,r}^{mode} \bar{b}_{m=1,r}^{pert} \sin \delta dr}{\mu_0 R \int_0^{r_{q=0}} r^2 \rho \frac{\partial(\Delta\Omega)}{\partial r} dr} \right|. \quad (4.20)$$

For numbers, $R = 1.5$ m, $\bar{n} = 7$ ($n = 5 - 9$), $\sin \delta = 1$, $\rho = \text{constant} = 1.6 \times 10^{-8}$ kg/m³ (a reasonable simplification for a flat density profile), $\bar{b}_{m=1}^{mode} = 5 \times 10^{-4}$ T, and $\bar{b}_{m=1}^{pert} = 2 \times 10^{-5}$ T. For simplicity assume $\Delta\Omega = \Delta\Omega|_{r=0}[1 - (r/a)^4]$, where $a = 0.52$ m. Then $\partial(\Delta\Omega)/\partial r = -4(\Delta\Omega|_{r=0})r^3/a^4$. Let $\Delta\Omega|_{r=0} = 16000$ /s from the typical measured difference between the measured flow velocity and core mode rotation. Therefore

$$\left\langle \frac{\partial(\Delta\Omega)}{\partial r} \right\rangle \equiv -\frac{4(\Delta\Omega)|_{r_{q=0}}}{a^4 r_{q=0}} \int_0^{r_{q=0}} r^3 dr = -\Delta\Omega|_{r_{q=0}} \frac{r_{q=0}^3}{a^4} = -(16000/\text{s}) \frac{(0.42 \text{ m})^3}{(0.52 \text{ m})^4} = -16200 \text{m}^{-1} \text{s}^{-1}. \quad (4.21)$$

Furthermore, if a weak r dependence is assumed for the mode amplitudes so that they can be factored out of the integral, the integral in the numerator amounts to multiplication by $(r_{q=0})^3/3 = (0.42 \text{ cm})^3/3 = 0.024696 \text{ m}^3$. Then (4.20) becomes

$$v_{\perp} = \left| \frac{\bar{n} a^4}{\mu_0 \rho r_{q=0}^3} \frac{\bar{b}_{m=1,r}^{mode} \bar{b}_{m=1,r}^{pert} \sin \delta}{-\Delta\Omega|_{r=0}} \right| = \frac{7(0.52 \text{ m})^4 (5 \times 10^{-4} \text{ T})(2 \times 10^{-5} \text{ T})(1)}{(4\pi \times 10^7 \text{ H/m})(1.6 \times 10^{-8} \text{ kg/m}^3)(1.5 \text{ m})(0.42 \text{ m})^3 (16000/\text{s})}$$

$$\approx 140 \text{ m}^2/\text{s}. \quad (4.22)$$

This is about triple the previous measurement of the global viscosity in the core of MST.⁴ The agreement is good, given the crudeness of the calculation. Moreover, it should not necessarily be expected for them to be the same, because the viscosity as measured in Ref. 4 deals with momentum *transport*, i.e. diffusion, whereas the process under investigation here is momentum *transfer*, i.e. a faster process.

A similar analysis can be performed for the $n = 6$ perturbation at the toroidal gap immediately prior to one of the events in which it locks. In this case only the (1,6) mode is affected, so the integration is just over its island. We will use the viscosity calculated in eqn. 4.22 and calculate the average angular velocity shear. The mode amplitude, $b_{(1,6)}^{mode}$, is $1.2 \times 10^{-3} \text{ T}$, and the perturbation amplitude, $b_{(1,6)}^{mode}$, is $9 \times 10^{-5} \text{ T}$. If the mode is centered about $r = 0.16 \text{ m}$, which is

reasonable, and a 10 cm island width is assumed, as well as the same parameters from the above calculation, then the result is

$$\begin{aligned}
 \left| \left\langle \frac{\partial(\Delta\Omega)}{\partial r} \right\rangle \right| &= \left| \frac{2n \int_{r_{(1,6)}-W/2}^{r_{(1,6)}+W/2} r^2 b_{(1,6),r}^{mode} b_{(1,6),r}^{pert} \sin \delta dr}{\mu_0 R \rho v_{\perp} \int_{r_{(1,6)}-W/2}^{r_{(1,6)}+W/2} r^2 dr} \right| \\
 &= \left| \frac{2n b_{(1,6),r}^{mode} b_{(1,6),r}^{pert} \sin \delta}{\mu_0 \rho R v_{\perp}} \right| \\
 &= \frac{2(6)(1.2 \times 10^{-3} \text{ T})(9 \times 10^{-5} \text{ T})(1)}{(4\pi \times 10^{-7} \text{ H/m})(1.6 \times 10^{-8} \text{ kg/m}^3)(1.5 \text{ m})(140 \text{ m}^2\text{s}^{-1})} \approx 3.07 \times 10^5 \text{ m}^{-1}\text{s}^{-1}. \quad (4.23)
 \end{aligned}$$

This is about a factor of 20 larger than what was calculated for the $m = 1$ perturbation at the poloidal gap (eqn. 4.21). This larger differential rotation seems to bear out the argument in § 4.1.3 that the viscous torque is larger for perturbations at the toroidal gap (single mode) versus those at the poloidal gap (multiple modes).

4.2 Rotating Magnetic Perturbation

The RMP system was able to deliver 1250 A peak current. If the (1,6) magnetic perturbation from the applied current transformation from § 3.2.2.2 is used, this translates into a peak radial magnetic field of $(1250 \text{ A}) \times (8.7 \times 10^{-5} \text{ G/A}) = 0.11 \text{ G}$, which is about 20% of the ($m = 1$, $n = 6$) magnetic perturbation amplitude at the toroidal gap required to produce locking (§ 4.1.2). Figure 4.12(a) shows the toroidal phase velocity of the (1,6) mode averaged over 50 discharges. The velocity does stay near the RMP velocity. However, this is true before and after the RMP circuit was fired as well as when the circuit is on. Figure 4.12(b), the standard deviation of the (1,6) mode phase velocity, shows no decrease during the time in which the RMP was in use, in-

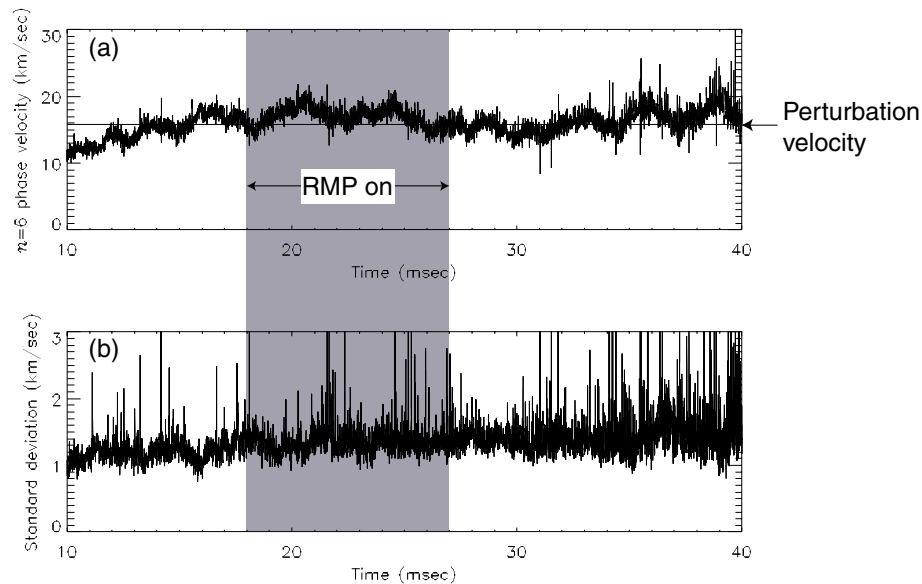


Figure 4.10. Discharges with applied RMP (gray area). (a) Ensemble averaged (1,6) mode toroidal phase velocity, and (b) standard deviation of the phase velocity.

dicating there doesn't seem to be any locking-in of the phase velocity to that of the RMP, so its effect is presumably negligible.

Since the frequency of the perturbation matches the mode rotation frequency well [cf. Fig. 4.12(a)], the lack of a result is surprising, given that the torque should be large when the frequency difference between the perturbation and the mode is small. There must be large torques between the (1,6) and adjacent rotating modes. As discussed for the static perturbation at the toroidal gap in §§ 4.1.2-4, these torques could be produced by viscous coupling between the (1,6) mode and the adjacent ones, and the implication from § 4.1.4 is that these torques are large.

Experiments have been done on the RFX RFP to induce rotation of the (0,1) mode by modulating the toroidal field in order to generate a (0,1) perturbation.⁸ By rotating this mode, the $m = 1$ modes are made to rotate as well, and the frequency relationships between the various

modes are consistent with nonlinear coupling. It is thus entirely possible that a more powerful RMP system could produce results on MST. Some time will be devoted to this in Chapter 6.

4.3 External torques during sawtooth activity

Substantial external torques on the modes may be generated during sawtooth events, because of the enhancement of the mode amplitudes and the presence of field errors. It will be instructive to perform calculations similar to those in § 4.1.3, and compare with those results.

The ensemble-averaged amplitude of the $m = 1$ component of the field error at the poloidal gap is plotted in Fig. 4.13(a). The amplitude of the (1,6) mode is plotted in Fig. 4.13(b), and the product of the two multiplied by the (1,6) fraction (eqn 4.6) is plotted in Fig. 4.13(c). The peak value is 2.3 Gauss^2 , i.e. the torque is $2.3 C'_{(1,6)} \text{ Gauss}^2$, where the ' refers to evaluation at a sawtooth crash, not a derivative.

This result should be compared with the calculations from §4.1.3. The $m = 1$ perturbation

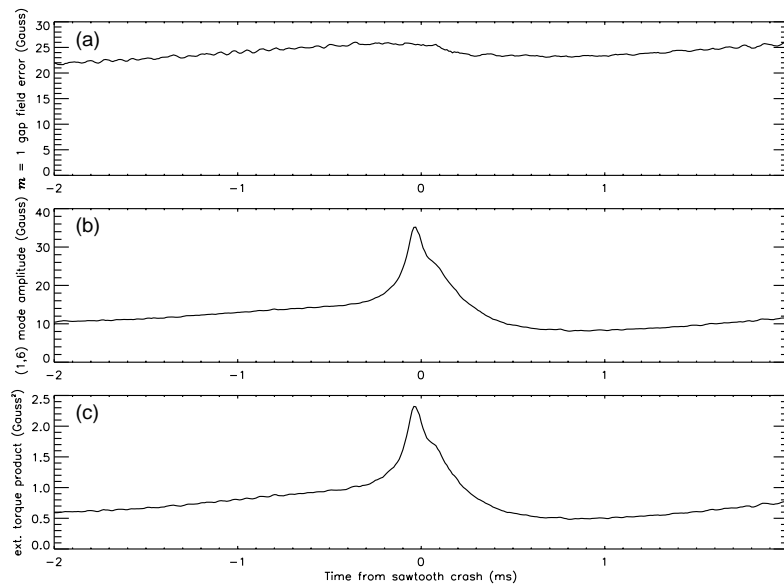


Figure 4.13. Ensemble averaged (a) $m = 1$ gap field error and (b) (1,6) mode amplitude. (c) Product of (a) and (b) multiplied by the $n = 6$ fraction for an $m = 1$ perturbation at the poloidal gap.

for locking led to an external torque of $1.2 C_{(1,6)} \text{ Gauss}^2$ (eqn. 4.7), and the $n = 6$ perturbation gave a torque of $7.2 C_{(1,6)} \text{ Gauss}^2$ (eqn. 4.8), so if $C'_{(1,6)} \sim C_{(1,6)}$ the external torque on the (1,6) mode during a sawtooth crash is in the range of what is needed for an external perturbation to cause locking. A caveat is that circumstances are not exactly the same between the sawtooth crash and the static perturbation: the current profile is different during the sawtooth crash than away from the crash, and inertia is important because of the large deceleration of the mode. However, as will be discussed in the next chapter, the observed deceleration of the (1,6) mode cannot be solely due to the external torque on it in any case.

Finally, it will also be of interest to compute a similar product for the $m = 0$ field error and the (0,1) mode. The ensemble-averaged amplitude of the $m = 0$ component of the field error at the poloidal gap is plotted in Fig. 4.14(a). The amplitude of the (0,1) mode is plotted in Fig.

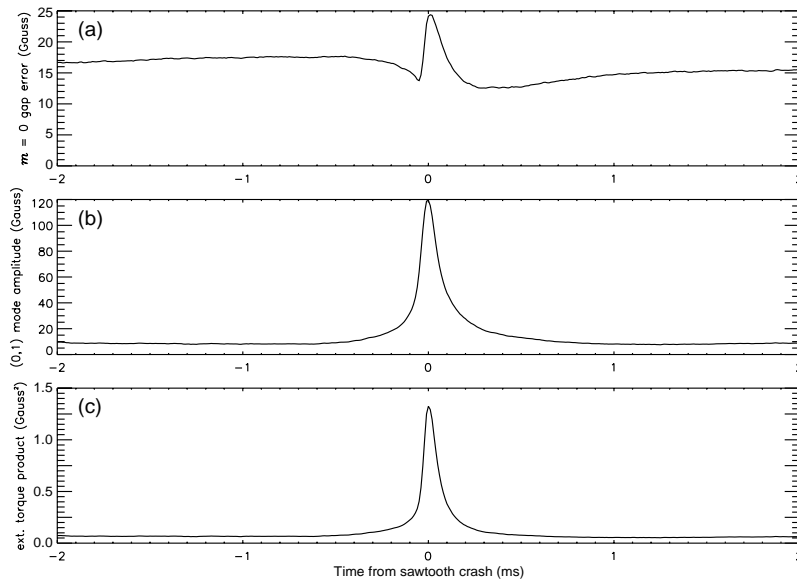


Figure 4.14. Ensemble averaged (a) $m = 0$ gap field error and (b) (0,1) mode amplitude. (c) Product of (a) and (b) multiplied by the $n = 1$ fraction for an $m = 0$ perturbation at the poloidal gap.

4.14(b), and the product of the two multiplied by the (0,1) fraction (§ 4.1.3) is plotted in Fig. 4.14(c). The peak value is 1.3 Gauss^2 , i.e. a torque of $1.3 C'_{(0,1)} \text{ Gauss}^2$. This is much larger than what was found for the $m = 0$ static perturbation if $C_{(0,1)} \sim C'_{(0,1)}$. Once again, the situations may not strictly be comparable.

4.4 Summary

Many of the results of the static perturbation experiments are consistent with the action of an external electromagnetic torque: the $m = 1$ modes were locked by a large enough $m = 1$ perturbation, but not by $m = 0$ or $m = 2$ perturbations; the (0,1) mode is locked by an $m = 0$ perturbation, and the (1,6) mode is locked by an $n = 6$ perturbation. However, the torque from the $n = 6$ perturbation is found to be several times larger than that from the $m = 1$ perturbation, presumably due to viscosity between the islands in the former case. Rough calculations of the viscosity and differential rotation support this contention. The external torques exerted on the $m = 0$ and $m = 1$ modes during a sawtooth crash appear to be of similar magnitude to those exerted by static perturbations that induce locking. The result that the (1,7) and (1,8) modes are locked by the $n = 6$ perturbation is not explained by the action of an external torque. This will be discussed in the next chapter.

References:

- ¹ A.K Hansen, A.F. Almagri, D. J. Den Hartog, S.C. Prager, and J. S. Sarff, Phys. Plasmas **5**, 2942 (1998).
- ² D. Craig, A. F. Almagri, J. K. Anderson, J. T. Chapman, C.-S. Chiang, N. A. Crocker, D. J. Den Hartog, G. Fiksel, S. C. Prager, J. S. Sarff, and M. R. Stoneking, Phys. Rev. Lett. **79**, 1865 (1997).
- ³ D. Craig, Ph. D. thesis, University of Wisconsin—Madison (1998).
- ⁴ A. F. Almagri, J. T. Chapman, C.-S. Chiang, D. Craig, D. J. Den Hartog, C. C. Hegna, and S. C. Prager, Phys. Plasmas **5** 3982 (1998).
- ⁵ A.F. Almagri, S. Assadi, S.C. Prager, J.S. Sarff, D.W Kerst, Phys. Fluids B **4**, 4080 (1992).
- ⁶ R.N. Dexter, D.W. Kerst, T.W. Lovell, S.C. Prager, and J.C. Sprott, PLP 965, Plasma Studies, University of Wis-

consin (1985).

⁷ M. Yokoyama, J.D. Callen, and C.C. Hegna, Nucl. Fusion **36**, 1307, (1996).

⁸ R. Bartioromo, T. Bolzonella, A. Buffa, G. Chitarin, S. Martini, A. Masiello, S. Ortolani, R. Piovan, P. Sonato, and G. Zollino, Phys. Rev. Lett. **83**, 1779 (1999).

5 Experiments involving nonlinear electromagnetic torques

In this chapter experimental results will be discussed that focus on internal torques, specifically the nonlinear torque (§ 2.2.1.2.2). As discussed in § 3.2.1.2, it is difficult to do the harmonic separation needed to find the amplitudes of the ($m = 0, n \geq 5$) modes, i.e. those needed for torques on the $m = 1$ modes from toroidal coupling (§ 2.2.1.2.1), so this process will not be investigated. However, many of the results could be interpretable in terms of this process as well as the nonlinear torque.

As a carryover from the previous chapter, § 5.1 is a discussion of the results from the $n = 6$ perturbation experiment in terms of the nonlinear torque. The rest of this chapter (§§ 5.2 and 5.3) will focus on the kinematics of the modes during the sawtooth cycle (cf. §2.4). The first topic, in § 5.2.1, will be the coupling of the mode and flow kinematics, which means that changes in the mode rotation are linked to plasma momentum transport. Next, in § 5.2.2 is a discussion of the dynamics of the modes during the sawtooth cycle, and how the mode kinematics are consistent with the action of the nonlinear torque. Standard RFP discharges are described in § 5.2.2.1. Section 5.2.2.2 is a description of how modifying the flow/mode rotation profile through an applied edge electric field produced the first results that indicated that rapid changes in the core mode rotation are not due to the action of external torques from field errors. Following, in § 5.2.2.3 is a discussion concerning discharges in which the $q = 0$ resonance was removed by changing the equilibrium, which resulted in the dramatic reduction of changes in the velocity of the $m = 1$ modes. This is also consistent with the nonlinear torque being a dominant process. Having made the case for the importance of the nonlinear torque in the sawtooth crash, measurements of the correlated triple products of mode amplitudes that characterize the nonlinear torque (cf. eqn. 2.11) will be discussed in § 5.2.3. The experiments in § 5.2.2.2, § 5.2.2.3,

and § 5.2.3 constitute the major pieces of evidence for the presence of nonlinear torques in MST. Finally, in § 5.3, ensembles over sawtooth crashes where the $m = 1$ modes undergo permanent locking will be compared and contrasted with ensembles taken from the same discharges in which the modes reaccelerate.

5.1 Nonlinear torques in active experiments

Recall from § 4.1.2 that application of a sufficiently large $n = 6$ magnetic perturbation resulted in the locking of the (1,7) and (1,8) modes as well as the (1,6). This was shown in Figs. 4.10 and 4.11. If electromagnetic torques are the sole agents responsible, then the nonlinear torque must be involved, because the (1,7) and (1,8) modes don't satisfy the resonance condition for the external torque, and the torque from toroidal coupling only works for modes with different m and the same n . Moreover, the locking most frequently occurs on a sawtooth crash, where the nonlinear torque should be large (cf. § 5.2). However, other mechanisms, such as viscous torques between mode structures, may also explain the results.

5.2 Nonlinear torques in sawtooth activity

5.2.1 Modes and flow

It has been reported previously that the toroidal velocity of the modes and the toroidal plasma flow in MST track each other closely.¹ Ensemble averages of the (1,6) toroidal phase velocity and C^{4+} (a.k.a. Carbon V) ion flow, as measured by the ion dynamics spectrometer, are shown in Fig. 5.1(a). The dynamics of this species reflect that of the core majority ions. Note that the scales are different. Also, it is more typical for the flow velocity between sawtooth crashes to be about 5-10 km/sec higher than the mode velocity rather than for them to be almost the same as in Fig. 5.1(a). The difference is probably in the radial width of the C^{4+} emission profile. In any case, what is seen is that the $m = 1$ modes and core ions both decelerate at essentially

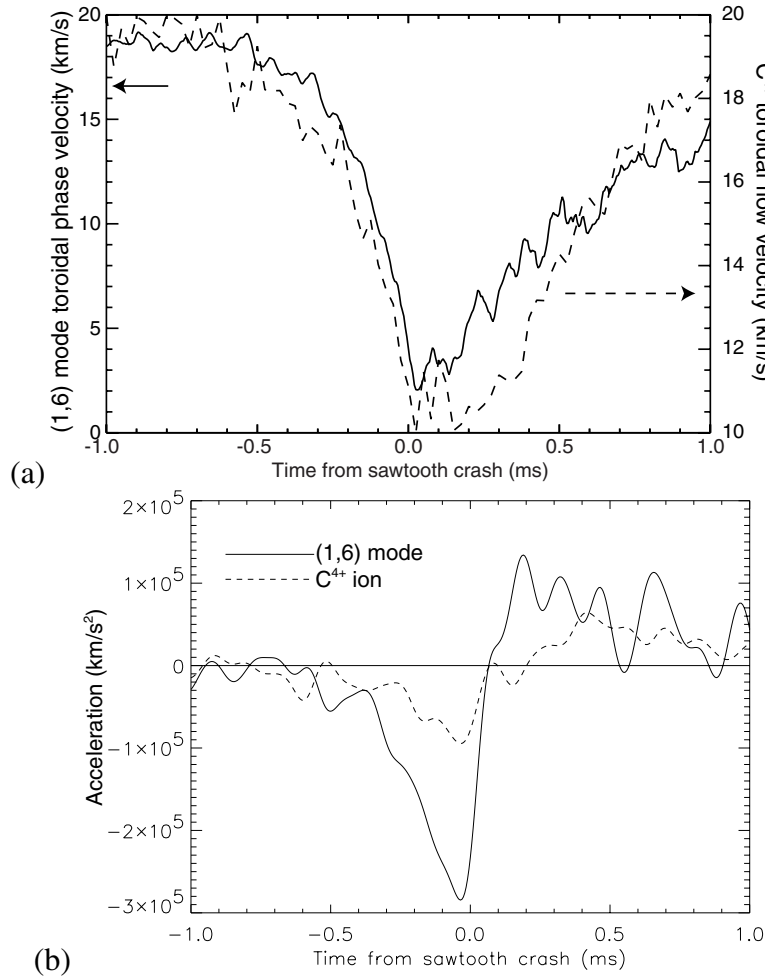


Figure 5.1. (a) Toroidal phase velocity of (1,6) mode (solid) and toroidal velocity of C⁴⁺ ions (dashed) averaged over an ensemble of 30 sawtooth crashes. Note the difference in scales. (b) Toroidal acceleration of (1,6) mode (solid) and C⁴⁺ ions (dashed) for the same ensemble.

the same time before the sawtooth crash, and the flow reaccelerates after the modes start to spin back up following the crash. Because the flow changes along with the mode rotation, it can be argued that there is momentum transport associated with the mode kinematics. In addition, the $\sim 100 \mu\text{s}$ timescale for the flow deceleration is faster than a classical slowing down time, $\sim 250 \text{ ms}$,² so the momentum transport is anomalous. Anomalous transport of momentum was reported previously for MST in Ref. 2, in a different context.

5.2.2 Mode dynamics in the MST sawtooth cycle.

5.2.2.1 Standard case

The amplitudes of all of the modes increase at the sawtooth crash, as shown in Fig. 5.2. The $m = 0$ modes [Fig. 5.2(a)] spike up at the crash, while the $m = 1$ modes tend to rise more slowly [Fig 5.2(b)].

The kinematics of the ($m = 1, n = 6-8$) modes are similar to each other during the sawtooth cycle (Fig. 5.3), with those of the (1,5) being slightly different from the others. All show rapid deceleration around the time of the sawtooth crash, followed by a slower reacceleration. As is apparent from Fig. 5.3(a), the velocity tends to decrease with increasing n , corresponding to increasing radii (cf. Fig. 2.1). In addition, the (1,6) mode decelerates first, with the higher- n modes following suit later. The (1,5) mode decelerates last.

The $m = 0$ modes, as exemplified by the (0,1) mode, tend to rotate in the opposite direction to the $m = 1$ modes, at a smaller speed (Fig. 5.4). At the sawtooth crash, the rotation profile

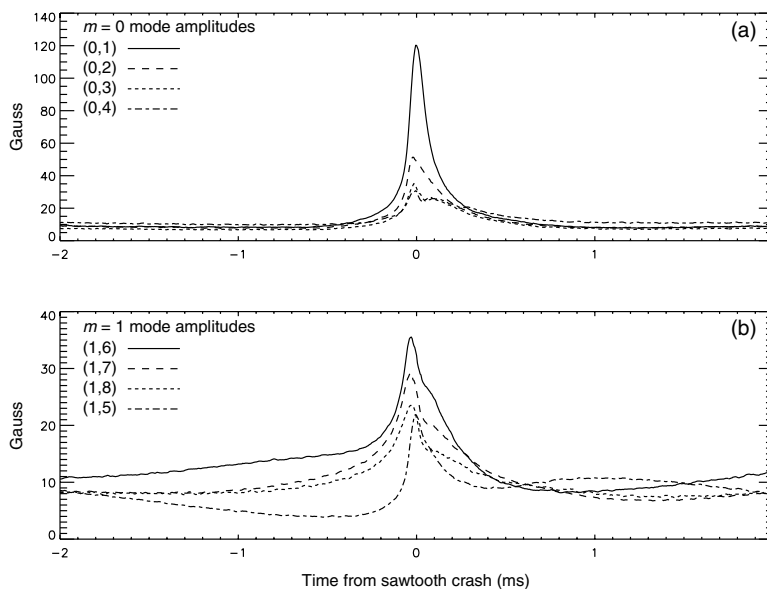


Figure 5.2. (a) $m = 0$ mode amplitudes and (b) $m = 1$ mode amplitudes, ensemble averaged over ~ 700 sawtooth events.

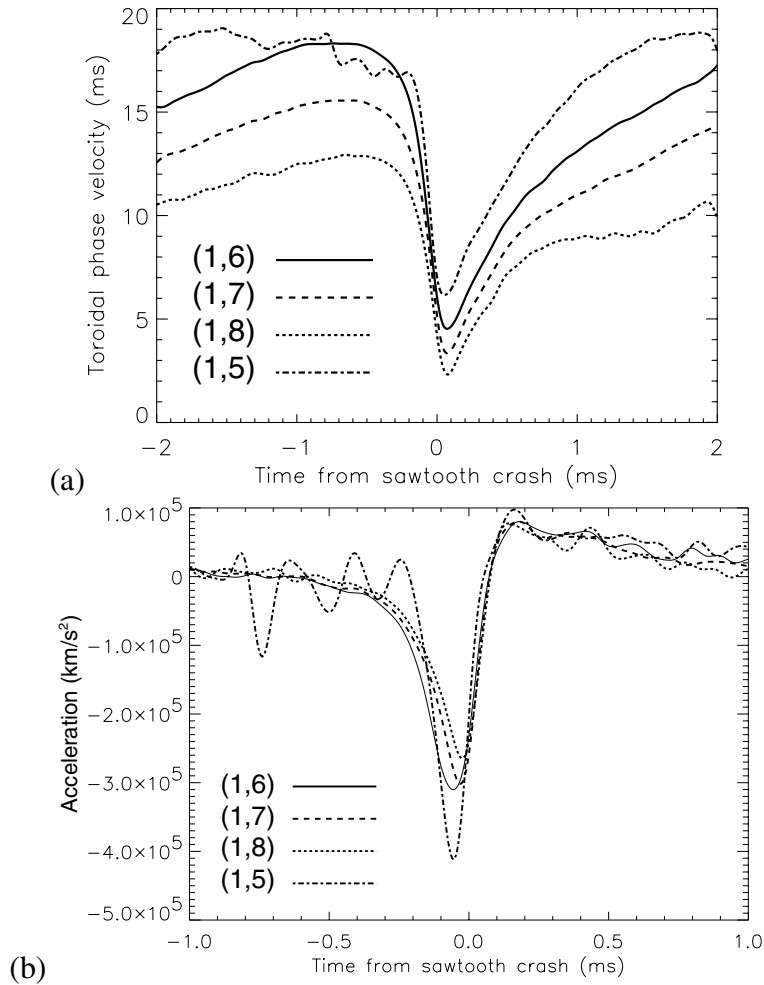


Figure 5.3. (a) Toroidal phase velocity of (1,5), (1,6), (1,7), and (1,8) modes, ensemble averaged over ~ 700 sawtooth events. (b) Toroidal acceleration of the same modes, for the same ensemble.

flattens, as indicated in Fig. 5.4. This is an important result, because it is consistent with what would be expected for the action of the nonlinear torque.

5.2.2.2 Applied radial electric field

Although Fig. 5.4 shows flattening of the mode rotation, the same result could be produced by the $m = 0$ and $m = 1$ components of the field error at the poloidal gap acting on the respective resonant modes. Experiments that involved applying a radial electric field within the plasma edge showed that field errors were not the primary players in the flattening.

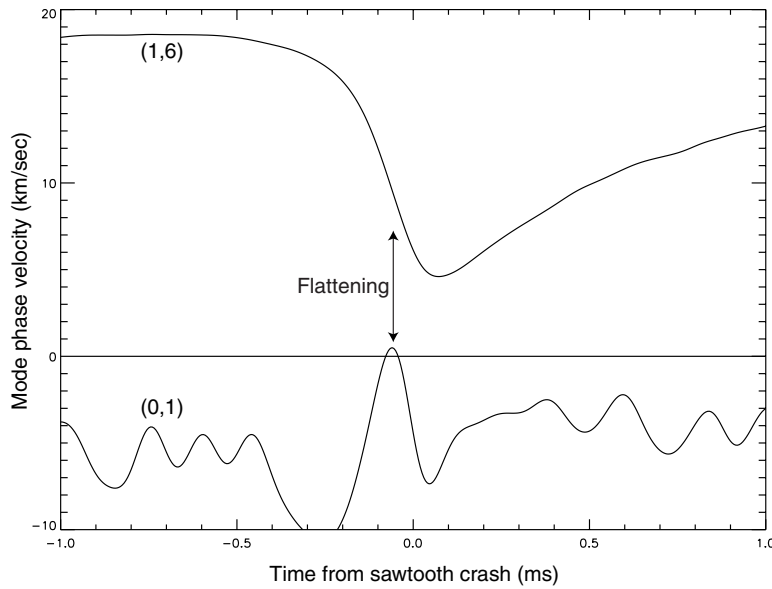


Figure 5.4. (1,6) and (0,1) mode toroidal phase velocities, ensemble averaged over ~ 700 sawtooth crashes.

The radial electric field was applied in two different ways. One was to insert a metal probe into the plasma ($\sim 10\text{-}15$ cm) that was biased with respect to MST's wall (cf. § 4.1.1.3).² The other was to use multiple “plasma guns”,^{3,4,5} small plasma sources that are inserted a short distance (~ 5 cm) into the plasma and biased with respect to the wall in order to generate electrons. The results to be presented in this section are from discharges with several plasma guns inserted, but similar results are obtained when the metal probe is used.

The radial electric field promptly changes the toroidal flow in the edge plasma (near the guns) [Fig. 5.5(a), reprinted from Ref. 5] through the $E_r B_\theta$ term of the $\mathbf{E} \times \mathbf{B}$ drift. The core flow responds to this change, on a slower timescale [Fig. 5.5(b)]. The change in the flow profile in turn affects the mode rotation. Figure 5.6 depicts the C^{4+} ion (core) toroidal flow velocity and (1,6) mode toroidal phase velocity. When the additional electric field is active, indicated by the region labeled “Bias on” in the plot, both the ion flow and the mode rotation reverse their direction. In addition, as labeled on the figure, the modes and flow *speed up* rather than slow down

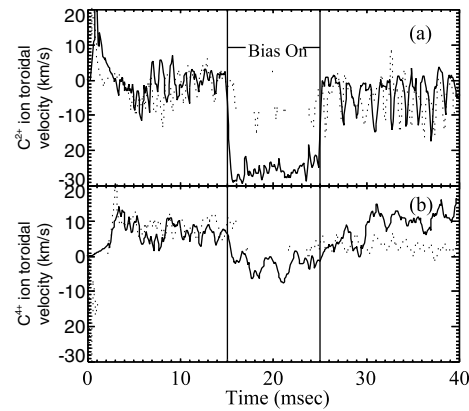


Figure 5.5. (a) C^{4+} and (b) C^{2+} toroidal flow velocity for a discharge with applied electric field.

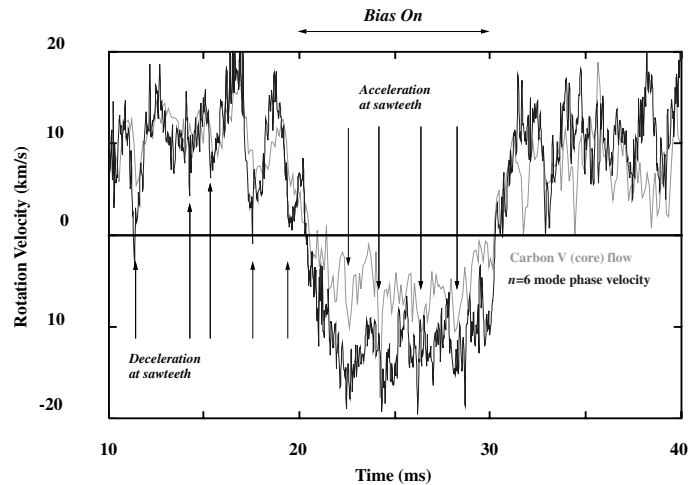


Figure 5.6. (1,6) mode phase velocity and C^{4+} flow for a discharge with applied electric field.

on sawtooth crashes, though the direction of acceleration is the same as in standard discharges. This is inconsistent with the action of the external torque imposed by a static field error.

In Fig. 5.7 are plotted the phase velocities of the (0,1) and (1,6) modes, averaged over ~ 30 discharges. The averaging procedure washes away much of the sawtooth activity. The (0,1) mode starts out with essentially zero velocity, and promptly accelerates in response to the applied electric field, ultimately reaching a speed of ~ 17 km/sec. The (1,6) mode rotates at about 10 km/sec before the radial electric field is turned on, then over a period of 1-2 ms it decelerates

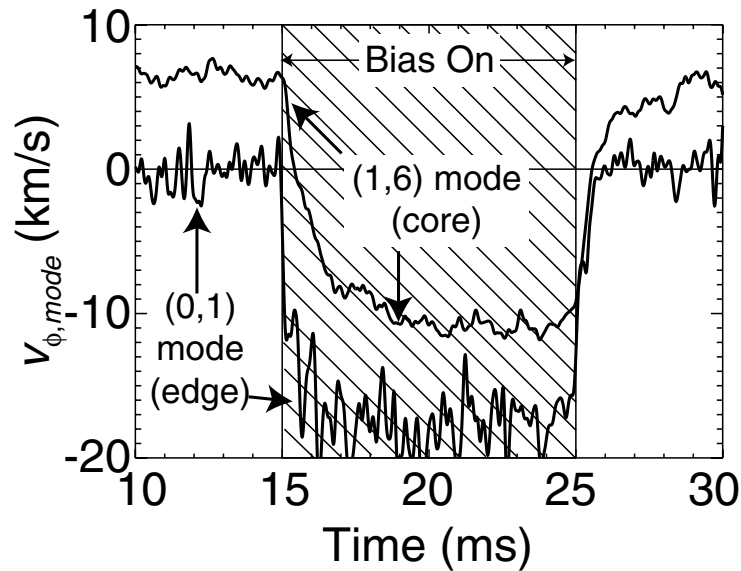


Figure 5.7. (0,1) and (1,6) modes ensemble averaged over ~30 discharges with applied radial electric field.

through zero velocity, finally settling down at ~ 10 km/sec, in the opposite direction to its original direction of rotation. The effect of the applied electric field, therefore, is to offset the entire rotation profile by a constant amount. These results should be compared to those in Fig. 5.5; clearly the (0,1) mode and the C^{2+} flow velocity have similar behavior, just as do the (1,6) mode and the C^{4+} ion flow.

The kinematics of these modes over a sawtooth crash are shown in Fig. 5.8. Figure 5.8(a) shows the mode velocities, averaged over ~ 70 events where the guns were in the plasma but the electric field was not on, i.e. before 15 ms and after 25 ms. The results are similar to those shown in Fig. 5.4. In Fig. 5.8(b) the mode velocities are averaged over ~ 280 sawtooth events during the period of applied electric field. The plot looks similar to Fig. 5.8(a), except for the offset. Note that in both cases, the two rotation velocities tend to approach each other, i.e. the rotation profile flattens, just before the sawtooth crash. This is consistent with what should be expected from the nonlinear torque: an overall flattening of the momentum profile.

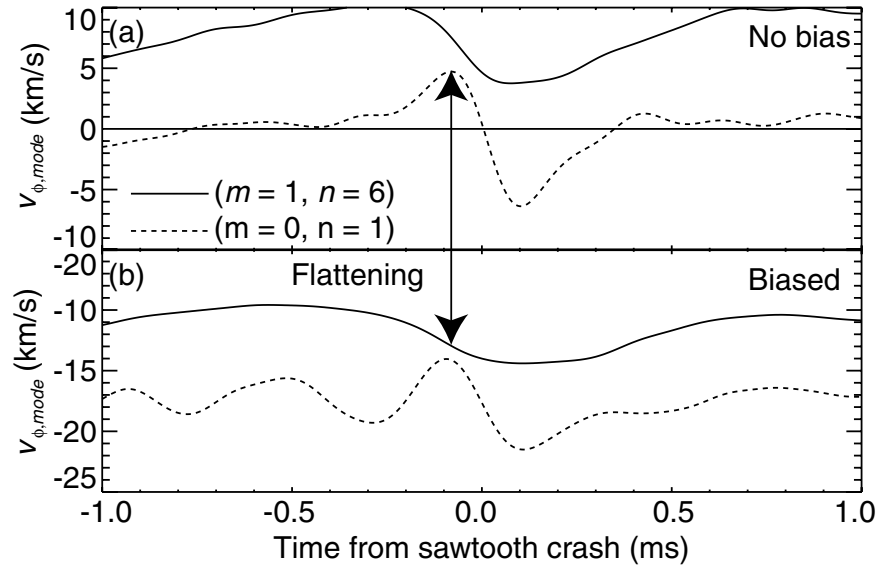


Figure 5.8. (0,1) and (1,6) modes ensemble averaged over (a) ~70 sawteeth with no applied radial electric field, and (b) ~280 sawteeth with applied radial electric field..

5.2.2.3 Non-reversed discharge

An experiment was done in MST in which discharges were run with a non-reversed toroidal field. The toroidal field on the edge was still quite small, so the q profile of the configuration should not have been vastly different from an RFP, except for being positive everywhere within the plasma. By doing this, the $m=0$ resonance was removed from the plasma, so the expectation was that the nonlinear (or other internal) torque would vanish.

In fact, that is just what was seen. Figure 5.9(a) is the toroidal phase velocity of the (1,6) mode. The large deceleration events are absent. Figure 5.9(b) is the (1,6) mode amplitude. There are still sawtooth-like bursts in its amplitude, and because of the presence of a nonzero $m=1$ field error, there are still external torques on this mode, which may be responsible for the small changes in the velocity on the bursts [Fig. 5.9(a)]. Figure 5.9(c) is the (0,1) mode amplitude. No bursts are seen, and it is essentially at the noise level for detection. The absence of the large changes in the (1,6) mode velocity that are seen in other discharges provides another piece

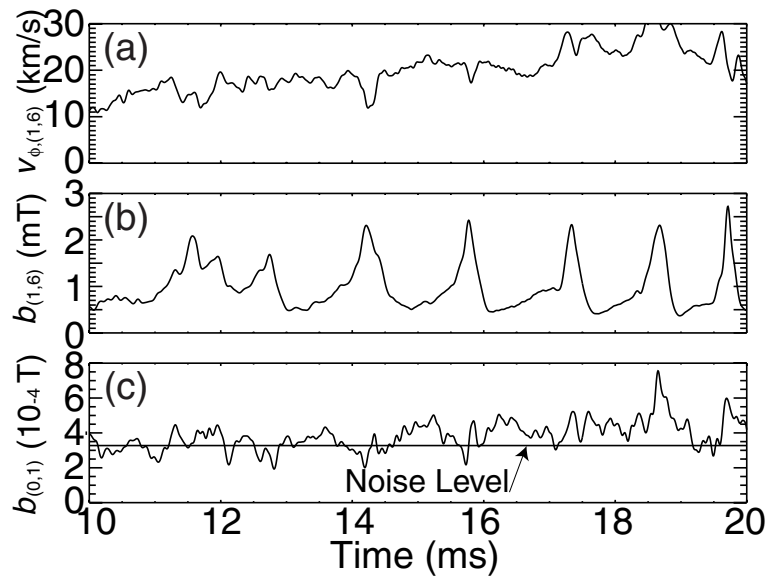


Figure 5.9. (a) Toroidal phase velocity of (1,6) mode, (b) amplitude of (1,6) mode, and (c) amplitude of (0,1) mode for a non-reversed discharge.

of evidence that nonlinear torques are responsible for the kinematics of the modes during a sawtooth crash.

In summary, the nonlinear torque is a major agent in the kinematics of the modes during a sawtooth crash. External torques on the modes from resonant field errors presumably do occur, but are not responsible for the large ($3 \times 10^8 \text{ m/s}^2$) deceleration seen in the $m = 1$ modes.

5.2.3 Triple product measurement

Having presented the argument that the nonlinear torque is a dominant player in the kinematics of the modes during the sawtooth crash, it is natural to attempt a measurement. This was done using the toroidal arrays of magnetic pickup coils to find the mode amplitudes and phases between the modes that are characteristic of the nonlinear torque (cf. eqn. 2.11).

For simplicity, the three largest terms that go into the torque on the (1,6) mode will be examined, rather than trying to approximate the total torque by calculating all of the triple products, especially because the nonlinear coupling coefficients in eqn. 2.11 involve detailed knowl-

edge of the current profile,⁶ which is not available on MST. The three products are the two that involve the (1,6) and (0,1) mode:

$$\langle b_{(1,7)}b_{(1,6)}b_{(0,1)}\sin(\delta_{(1,7)}-\delta_{(1,6)}-\delta_{(0,1)}) \rangle \text{ and } \langle b_{(1,6)}b_{(1,5)}b_{(0,1)}\sin(\delta_{(1,6)}-\delta_{(1,5)}-\delta_{(0,1)}) \rangle,$$

and the only term involving the (0,2) mode: $\langle b_{(1,8)}b_{(1,6)}b_{(0,2)}\sin(\delta_{(1,7)}-\delta_{(1,6)}-\delta_{(0,1)}) \rangle$.

The ensemble used consists of ~ 700 similar sawtooth events. The analysis technique was straightforward: average the mode amplitudes and the sine of the differences in their phases (cf. eqn. 2.11), and then multiply them. The results are shown in Fig. 5.10.

Figure 5.10(a) is the toroidal velocity of the (1,6) mode, for reference purposes. In Fig. 5.10(b) are plotted the triple products. The products involving the (1,7) and (0,1) modes and the (1,5) and (0,1) modes are of comparable amplitude, while the maximum of that involving the (1,8) and (0,2) modes is smaller. The relative amplitudes are what would be expected from the mode amplitudes, Fig. 5.10(c-d), in that the (1,7), (1,5) and (1,8) modes are not too far apart in amplitude, but the (0,2) mode is about a factor of 3 smaller than the (0,1). The changes in sign of the signals in 5.10(b) are obviously due to those in the sine of the phase difference, Fig. 5.10(e). Note that the term involving the (1,5) and (0,1) modes and that involving the (1,8) and (0,2) modes change sign at the same time, and that all of these quantities are nearly zero, i.e. uncorrelated, except for the region from 0.2 ms before the crash to 1 ms after the crash. A value of zero in this case represents a random phase averaged over many discharges, i.e. incoherence.

All of the triple products develop noticeable amplitudes at ~ 0.2 ms before the sawtooth crash. This is consistent with the time where a large change is seen in the acceleration of the (1,6) mode in Figs 5.3 and 5.4. In addition, the (0,1) mode accelerates at about the same time, as

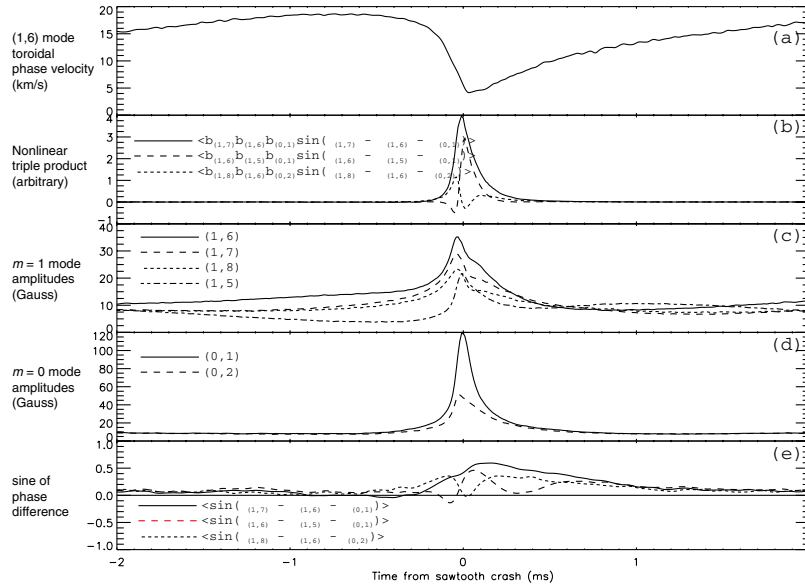


Figure 5.10. (a) Toroidal phase velocity of (1,6) mode, (b) nonlinear triple products, (c) $m = 1$ mode amplitudes, (d) $m = 0$ mode amplitudes, and (e) nonlinear phase factors, ensemble averaged over ~ 700 sawteeth.

seen in Figs. 5.4 and 5.5. The slower deceleration phase in the (1,6) kinematics that is seen between 0.5 and 0.2 ms is almost certainly not due to the nonlinear torque.

5.3 Permanent locking vs. reacceleration during sawtooth events.

As mentioned in § 2.4, in some instances the $m = 1$ modes will decelerate on a sawtooth crash, but not reaccelerate. Instead they will remain locked. An example of this phenomenon is shown in Fig. 5.11. In this discharge, several sawtooth events occur in which the (1,6) mode resumes rotation, then one in which the mode locks.

Kinematic differences in the modes between the two types of events can be seen in Fig 5.12. Besides the obvious difference of rotation vs. locking following the sawtooth crash, the (1,6) mode, representing all of the $m = 1$ modes, begins decelerating earlier for locking crashes [Figs. 5.12(a) and (b)]. In addition, the velocity of the (1,6) mode is slightly smaller on average

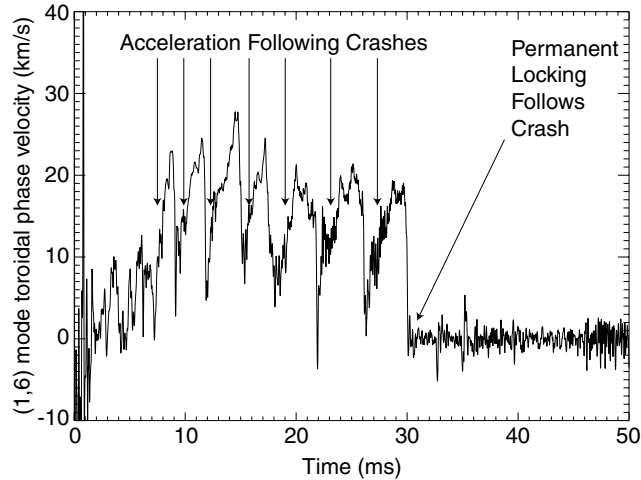


Figure 5.11. (1,6) mode phase velocity for typical discharge with several sawteeth without permanent locking of the $m = 1$ modes and one where locking occurs.

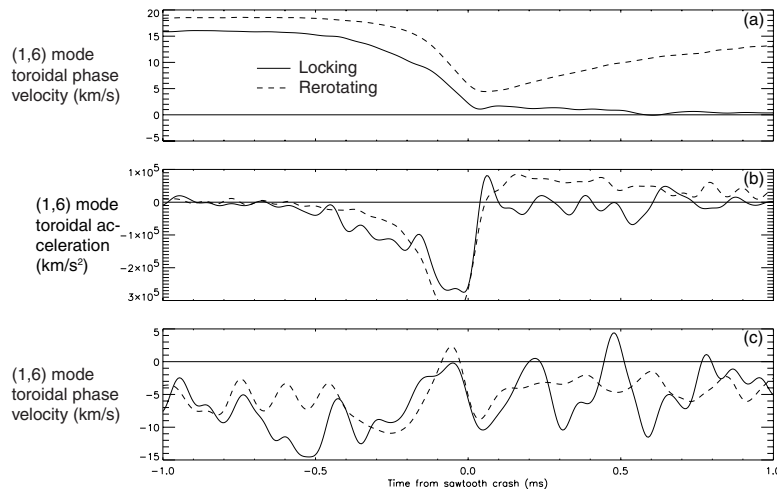


Figure 5.12. Ensemble averaged (a) Toroidal phase velocity of (1,6) mode, (b) toroidal acceleration of (1,6) mode, and (c) Toroidal phase velocity of (0,1) mode, for sawtooth events where permanent locking of the $m = 1$ modes occurred (solid, ~ 100 events) and events where the $m = 1$ modes continued to rotate (dashed, ~ 700 events)

before sawteeth where permanent locking occurs, although this is not true in every discharge.

There are also slight differences in the rotation of the (0,1) mode, too.

The obvious explanation that one would invoke to explain this phenomenon is differences between the sawtooth events in the external torque on the (1,6) mode. However, this is not borne out in the data. In Fig. 5.13(a) the product of the ensemble-averaged (1,6) mode amplitude and

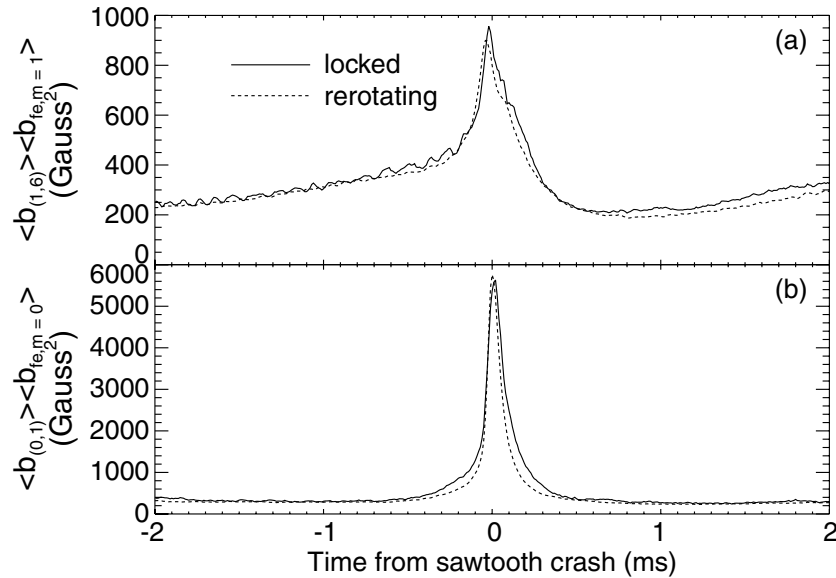


Figure 5.13. Products of (a) (1,6) mode amplitude and $m = 1$ field error at the poloidal gap, and (b) (0,1) mode amplitude and $m = 0$ field error at the poloidal gap, for ensembles of sawtooth crashes where permanent locking of the $m = 1$ modes occurred (solid)

$m = 1$ component of the field error at the poloidal gap are plotted for sawtooth events where permanent locking occurred (solid) and where the mode continued to rotate (dotted). This product is characteristic of the external torque. There is not a substantial difference between the two plots until after the sawtooth event. Figure 5.13(b) is a similar plot of the ensemble-averaged (0,1) mode amplitude and $m = 0$ component of the field error. This also does not differ much between the two classes of sawtooth events. At $400 \mu\text{s}$ before the crash, which is when the large difference in the acceleration of the $m = 1$ modes between locking and rotating events [Fig. 5.13(b)], there is a difference in Fig. 5.13(b), but it is not very large, and could be an effect of the change in the mode kinematics rather than causal.

Since changes in the external torques do not appear to be relevant to explain locking on sawtooth crashes in typical discharges, another explanation is needed. For an electromagnetic process, a logical candidate to investigate is an internal torque, specifically the nonlinear torque.

In Fig. 5.14 are plotted quantities relevant for the nonlinear torque, in the same format as Fig. 5.10, but for an ensemble of sawteeth where permanent locking of the $m = 1$ modes occurred. The signals look similar to those in Fig. 5.10, with no obvious feature at $400 \mu\text{s}$ before the sawtooth crash. The amplitudes of the nonlinear products are smaller for this case, mainly because the mode amplitudes are smaller. In Fig. 5.15, the (1,6) phase velocity (a), the triple product $\langle b_{(1,7)}b_{(1,6)}b_{(0,1)}\sin(\delta_{(1,7)}-\delta_{(1,6)}-\delta_{(0,1)}) \rangle$ (b), the (1,6) mode amplitude (c), the (0,1) mode amplitude (d), and the phase factor $\langle \sin(\delta_{(1,7)}-\delta_{(1,6)}-\delta_{(0,1)}) \rangle$ (e) are plotted for ensembles of sawtooth crashes with (solid) and without (dashed) permanent locking of the $m = 1$ modes. There are some slight differences [other than the (1,6) velocity] between the ensembles a few hundred microseconds before the crash, particularly the (1,6) and (0,1) mode amplitudes. However, it is difficult to attribute any significance to the differences. The most likely conclusion is

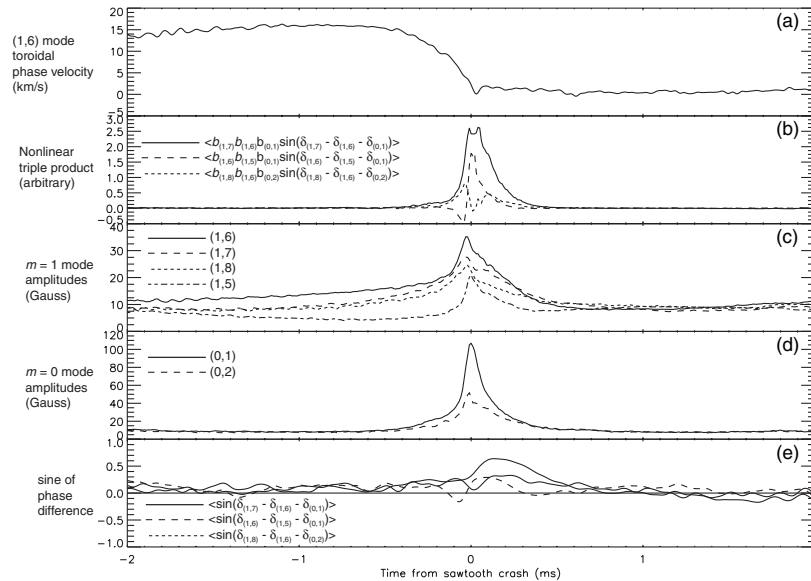


Figure 5.14. (a) Toroidal phase velocity of (1,6) mode, (b) nonlinear triple products, (c) $m = 1$ mode amplitudes, (d) $m = 0$ mode amplitudes, and (e) nonlinear phase factors for ensemble of sawteeth with permanent locking of the $m = 1$ modes.

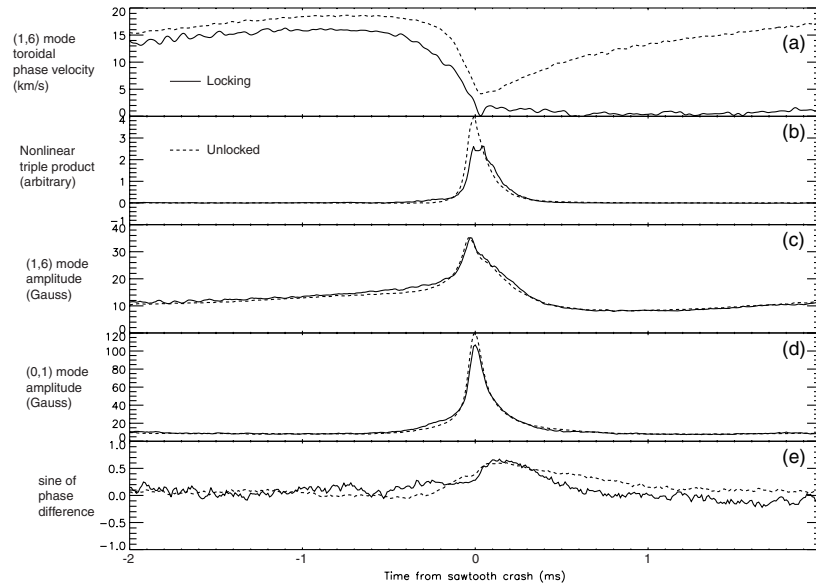


Figure 5.15. (a) Toroidal phase velocity of (1,6) mode, (b) nonlinear triple product, (c) (1,6) mode amplitude, (d) (0,1) mode amplitude, and (e) nonlinear phase factor for ensembles of sawteeth with permanent locking of the $m = 1$ modes (solid) and without permanent locking (dashed).

that, just as for the external torque, any differences in the internal torque do not produce permanent locking.

Another possibility, because of the strong coupling between the flow and the modes (§ 5.2.1), is that changes in the flow could produce changes in the mode rotation. However, as is shown in Fig. 5.15, for an ensemble of sawtooth events where permanent locking occurs, the large flow deceleration occurs ~ 300 ms after the mode deceleration becomes large. It seems unlikely, therefore, that the flow is doing anything that leads to locking of the $m = 1$ modes.

Other possibilities exist, but have not yet been investigated. One possibility is that the drive for the plasma/mode rotation, which is assumed to be a transport-generated radial electric field,¹ is reduced, e.g. by enhanced ion loss., thereby changing the viscous torque and reducing the electromagnetic torque necessary to produce locking. Figure 5.16 shows supporting evidence for this contention—following the sawtooth crash, the core (C^{4+}) and edge (C^{2+}) flow velocities

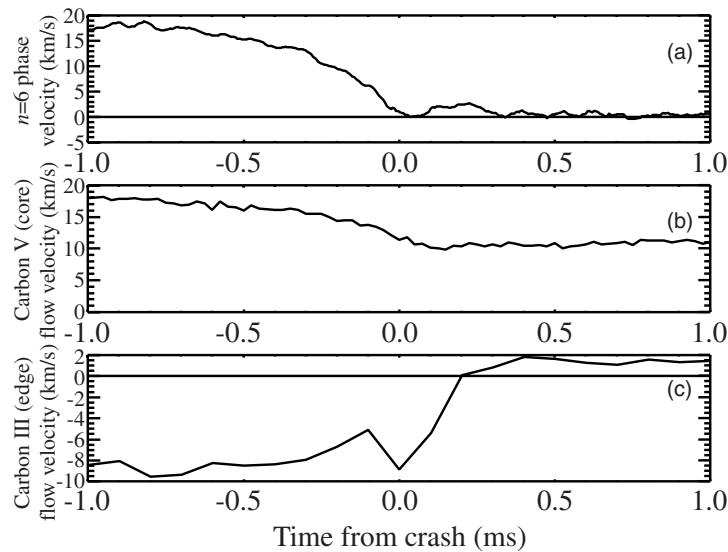


Figure 5.16. Ensemble averaged (a) Toroidal phase velocity of (1,6) mode, (b) C4+ ion toroidal velocity, and (c) C2+ ion toroidal velocity. Note that (c) is from a different set of discharges than (a) and (b).

are much closer together, but because locking has occurred, the profile stays flattened rather than peaking, as in prior to the sawtooth crash. In principle, the role of electric fields can be resolved through diagnostic enhancements on MST, such as CHERS and HIBP, both of which offer better spatial resolution for core measurements than does passive spectroscopy. Another possibility is that because the mode structure in MST is so complex, the locking process may be chaotic, depending sensitively and essentially unpredictably on the plasma conditions prior to a sawtooth crash.

5.4 Summary

Evidence for nonlinear torques is seen in several different situations on MST. When an $n = 6$ magnetic perturbation is applied at the toroidal gap, the other $m = 1$ modes lock too. The mode velocity profile appears to flatten during a sawtooth crash; when the direction of the core mode rotation is reversed by an applied electric field, the flattening effect leads to the $m = 1$

modes speeding up rather than slowing down during the crash. When the $q = 0$ resonance is removed from the plasma, the large changes in the mode velocity are also removed. Finally, when correlated triple products that are characteristic of the nonlinear torque were measured using the edge coil array, they showed the expected behavior—no torque far away from the sawtooth crash because of a lack of phase coherence, and a torque when the mode amplitudes are large and the phases are appropriate.

The process of locking of the $m = 1$ modes on a sawtooth crash has been investigated. The differences between the electromagnetic torques, both external and internal, do not appear to be significant between sawteeth where locking occurs and those where the $m = 1$ modes continue rotating. Nor are there significant differences in the measured ion flow. The cause of sawtooth mode locking, therefore, remains unknown.

References:

- ¹ D.J. Den Hartog, A.F. Almagri, J.T. Chapman, H Ji, S.C. Prager, and J.S. Sarff, *Phys. Plasmas* **2**, 2281 (1995).
- ² A.F. Almagri, J.T. Chapman, C.-S. Chiang, D. Craig, D.J. Den Hartog, C.C. Hegna, and S.C. Prager, *Phys. Plasmas* **5** 3982 (1998).
- ³ G. Fiksel, A.F. Almagri, D. Craig, M. Iida, S.C. Prager, J.S. Sarff, *Plasma Sources, Science and Technology* **5**, 78 (1996).
- ⁴ D. Craig, A. F. Almagri, J. K. Anderson, J. T. Chapman, C.-S. Chiang, N. A. Crocker, D. J. Den Hartog, G. Fiksel, S. C. Prager, J. S. Sarff, and M. R. Stoneking, *Phys. Rev. Lett.* **79**, 1865 (1997).
- ⁵ D. Craig, Ph. D. thesis, University of Wisconsin—Madison (1998).
- ⁶ C.C. Hegna, University of Wisconsin, private communication (2000).

6 Summary and Future Work

6.1 Summary of physics results

Static magnetic perturbations at the poloidal gap gave results that were consistent with theory and prior results from tokamaks: perturbations locked only the modes with which they were resonant, and not the other modes. On the other hand, an $n = 6$ perturbation at the toroidal gap produced locking of the other $m = 1$ modes as well, which is possibly due to the nonlinear torque. In addition, an $m = 1$ perturbation at the poloidal gap induces locking with less torque than an $n = 6$ perturbation at the toroidal gap. This difference was attributed to the large differential rotation in the latter case—a rudimentary calculation was performed that gave this result. This effect probably was responsible for the failure of the rotating magnetic perturbation experiment—a larger perturbation amplitude is needed. Finally, the electromagnetic torque generated at the poloidal gap during a sawtooth crash was found to be comparable to what was input in the static perturbation experiments.

In addition to the results of the $n = 6$ perturbation experiment, three other pieces of evidence for nonlinear torques in MST were found, all involving the sawtooth cycle. The direction of acceleration of the modes was unchanged when the mode rotation was offset by an applied radial electric field such that the $m = 1$ modes reversed their direction. The $m = 1$ modes no longer exhibited large changes in velocity when the plasma was run in a non-reversed state, such that there was no $m = 0$ resonance. Finally, correlated triple products characteristic of the nonlinear torque were measured, and found to have a phase appropriate to give a torque only near the sawtooth crash. In a related topic, it was found that the products characteristic of the external torque and those characteristic of the nonlinear torque were not substantially different

for sawteeth where the $m = 1$ modes permanently locked than for those where the $m = 1$ modes continued rotating. There was also no noticeable difference in the flow that could account for the behavior.

6.2 Future Work

Major physics issues that remain unaddressed are: (1) lack of quantification of the viscous torques between the islands in the absence of nonlinear coupling, (2) no direct measurement of the coupling coefficients for the nonlinear torque, and (3) the causation of locking at a sawtooth crash still remains unclear.

An experiment that should be done as soon as it is feasible is to apply a static $n = 6$ perturbation to a non-reversed discharge, to determine whether the observed locking of all of the $m = 1$ modes is due to the nonlinear torque or some other interaction such as viscous drag between the $m = 1$ magnetic islands. If the effect is due to the nonlinear torque, then only the (1,6) mode should be affected. If the locking of the other modes was due to inter-island viscosity, then we can get a measure of this, addressing (1) above. This experiment has not been performed yet because the $n = 6$ coils were damaged during the experiments in § 4.1.2.

In order to address issue (2), multiple-helicity rotating magnetic perturbations may provide an answer by breaking phase locking between the modes. Work is currently underway to put a set of $m = 1$ coils in place at the poloidal gap and apply a rotating $m = 1$, broadband n perturbation there. This has several advantages over the toroidal gap. The current requirements for such a system, as inferred from the static perturbation experiments in § 4.1, are not as daunting as for the toroidal gap (5 vs. 20 kA). In addition, the poloidal gap has magnetic pickup coils so that the perturbation can be detected in a straightforward manner. Finally, the $m = 1$

perturbation is resonant with multiple modes. This accounts for the lower magnetic perturbation levels needed, and also introduces the possibility for some interesting physics, in that the perturbation will attempt to drive the various $m = 1$ modes at the same frequency, which is not the usual situation.

In addition, design work is underway for a new set of coils at the toroidal gap that can generate magnetic fields that are sufficient to affect the modes. In addition to the $n = 6$ coil, there may be utility, because of the nonlinear torque, in putting in an $n = 1$ coil as well. In any case, the system will attempt to affect multiple modes simultaneously.

Along more speculative lines, D. Craig suggests that one option to deal with the large current requirements for the system would be to produce virtual wires within the plasma with plasma guns and return electrodes [to avoid applying the radial electric field (cf. § 5.2.2.2)] to generate a radial magnetic field. A simple experiment to do would be to set up a simple set of 4 guns and 4 return electrodes to generate a static $n = 1$ perturbation, and try to lock the (0,1) mode to the perturbation.

Diagnostic improvements on MST may help to resolve issue (3), permanent mode locking at a sawtooth crash. For example, the Heavy Ion Beam Probe will eventually provide time and spatially resolved information about the core radial electric field. The neutral-beam based CHERS diagnostic will provide better spatial resolution of the flow. These parameters reflect the drive for the mode rotation, which if changed could lead to locking.

Finally, there is ongoing work on MST to develop active correction for the field error at the poloidal gap. Its importance from the perspective of this work is to minimize the field errors

at the poloidal gap, and thereby reduce the external torques on the modes, so if issue (3) is not resolved, it may be possible to extend the locking-free parameter space.